Spring 2019

Dual modality optical coherence tomography : Technology development and biomedical applications

Farzana Rahmat Zaki
New Jersey Institute of Technology

ABSTRACT

DUAL MODALITY OPTICAL COHERENCE TOMOGRAPHY: TECHNOLOGY DEVELOPMENT AND BIOMEDICAL APPLICATIONS

by
Farzana Rahmat Zaki

Optical coherence tomography (OCT) is a cross-sectional imaging modality that is widely used in clinical ophthalmology and interventional cardiology. It is highly promising for *in situ* characterization of tumor tissues. OCT has high spatial resolution and high imaging speed to assist clinical decision making in real-time.

OCT can be used in both structural imaging and mechanical characterization. Malignant tumor tissue alters morphology. Additionally, structural OCT imaging has limited tissue differentiation capability because of the complex and noisy nature of the OCT signal. Moreover, the contrast of structural OCT signal derived from tissue's light scattering properties has little chemical specificity. Hence, interrogating additional tissue properties using OCT would improve the outcome of OCT's clinical applications. In addition to morphological difference, pathological tissue such as cancer breast tissue usually possesses higher stiffness compared to the normal healthy tissue, which indicates a compelling reason for the specific combination of structural OCT imaging with stiffness assessment in the development of dual-modality OCT system for the characterization of the breast cancer diagnosis.

This dissertation seeks to integrate the structural OCT imaging and the optical coherence elastography (OCE) for breast cancer tissue characterization. OCE is a functional extension of OCT. OCE measures the mechanical response (deformation, resonant frequency, elastic wave propagation) of biological tissues under external or

internal mechanical stimulation and extracts the mechanical properties of tissue related to its pathological and physiological processes. Conventional OCE techniques (i.e., compression, surface acoustic wave, magnetomotive OCE) measure the strain field and the results of OCE measurement are different under different loading conditions. Inconsistency is observed between OCE characterization results from different measurement sessions. Therefore, a robust mechanical characterization is required for force/stress quantification. A quantitative optical coherence elastography (qOCE) that tracks both force and displacement is proposed and developed at NJIT. qOCE instrument is based on a fiber optic probe integrated with a Fabry-Perot force sensor and the miniature probe can be delivered to arbitrary locations within animal or human body.

In this dissertation, the principle of qOCE technology is described. Experimental results are acquired to demonstrate the capability of qOCE in characterizing the elasticity of biological tissue. Moreover, a handheld optical instrument is developed to allow *in vivo* real-time OCE characterization based on an adaptive Doppler analysis algorithm to accurately track the motion of sample under compression.

For the development of the dual modality OCT system, the structural OCT images exhibit additive and multiplicative noises that degrade the image quality. To suppress noise in OCT imaging, a noise adaptive wavelet thresholding (NAWT) algorithm is developed to remove the speckle noise in OCT images. NAWT algorithm characterizes the speckle noise in the wavelet domain adaptively and removes the speckle noise while preserving the sample structure. Furthermore, a novel denoising algorithm is also developed that adaptively eliminates the additive noise from the complex OCT using Doppler variation analysis.

DUAL MODALITY OPTICAL COHERENCE TOMOGRAPHY: TECHNOLOGY DEVELOPMENT AND BIOMEDICAL APPLICATIONS

by
Farzana Rahmat Zaki

A Dissertation
Submitted to the Faculty of
New Jersey Institute of Technology
in Partial Fulfillment of the Requirements for the Degree of
Doctor of Philosophy in Electrical Engineering

Helen and John C. Hartmann
Department of Electrical and Computer Engineering

May 2019

.

APPROVAL PAGE

DUAL MODALITY OPTICAL COHERENCE TOMOGRAPHY: TECHNOLOGY DEVELOPMENT AND BIOMEDICAL APPLICATIONS

Farzana Rahmat Zaki

Dr. Xuan Liu, Dissertation Advisor Assistant Professor of Electrical and Computer Engineering, NJIT	Date
Dr. Haim Grebel, Committee Member Professor of Electrical and Computer Engineering, NJIT	Date
Dr. Namas Chandra, Committee Member Distinguished Professor of Biomedical Engineering, NJIT	Date
Dr. Dong Kyun Ko, Committee Member Assistant Professor of Electrical and Computer Engineering, NJIT	Date
Dr. Sagnik Basuray, Committee Member Assistant Professor of Chemical and Materials Engineering, NJIT	Date

BIOGRAPHICAL SKETCH

Author: Farzana Rahmat Zaki

Degree: Doctor of Philosophy

Date: May 2019

Undergraduate and Graduate Education:

- Doctor of Philosophy in Electrical Engineering,
  New Jersey Institute of Technology, Newark, NJ, USA, 2019

- Master of Science in Electrical and Electronic Engineering,
  Bangladesh University of Engineering and Technology, Dhaka, Bangladesh, 2013

- Bachelor of Science in Electrical and Electronic Engineering,
  Bangladesh University of Engineering and Technology, Dhaka, Bangladesh, 2006

Major: Electrical Engineering

Presentations and Publications:

Journal Articles:

X. Liu, F. R. Zaki, and Y. Wang, "Quantitative optical coherence elastography for robust stiffness assessment," *Applied Science*, vol. 8, no. 8, pp. 1255, 2018.

X. Liu, F. R. Zaki, H. Wu, C. Wang, and Y. Wang, "Temporally and spatially adaptive Doppler analysis for robust handheld optical coherence elastography," *Biomedical Optics Express*, vol. 9, no. 7, pp. 3335-3353, 2018.

X. Liu, F. R. Zaki, and D. Renaud, "Assessment and removal of additive noise in a complex optical coherence tomography signal based on Doppler variation analysis," *Applied Optics*, vol. 57, no. 11, pp. 2873-2880, 2018.

F. R. Zaki, Y. Wang, H. Su, X. Yuan, and X. Liu, "Noise adaptive wavelet thresholding for speckle noise removal in optical coherence tomography," *Biomedical Optics Express*, vol. 8, no. 5, pp. 2720-2731, 2017.

X. Liu, F. R. Zaki, Y. Wang, Q. Huang, X. Mei and J. Wang, "Secure fingerprint identification based on structural and microangiographic optical coherence tomography," *Applied Optics*, vol. 56, no. 8, pp. 2255-2259, 2017.

F. R. Zaki, I. Hou, D. Cooper, D. Patel, Y. Yang, and X. Liu, "High-definition optical coherence tomography imaging for noninvasive examination of heritage works," *Applied Optics*, vol. 55, no. 36, pp. 10313-10317, 2016.

Y. Qiu, F. R. Zaki, N. Chandra, S. A. Chester, and X. Liu, "Nonlinear characterization of elasticity using quantitative optical coherence elastography," *Biomedical Optics Express*, vol. 7, no. 11, pp. 4702-4710, 2016.

Conference Papers:

F. R. Zaki, Y. Wang, C. Wang, and X. Liu, "Adaptive Doppler analysis for robust handheld optical coherence elastography," In Proc. SPIE 10880, Optical Elastography and Tissue Biomechanics VI, 108801I, 21 February 2019.

X. Liu, F. R. Zaki, H. Garg, and J. Rodriguez, "OCE quantification of Poisson's ratio through 2D speckle tracking," In Proc. SPIE 10880, Optical Elastography and Tissue Biomechanics VI, 108801J, 21 February 2019.

F. R. Zaki, Y. Wang, X. Yuan, and X. Liu, "Adaptive wavelet thresholding for optical coherence tomography image denoising," in Imaging and Applied Optics 2017 (3D, AIO, COSI, IS, MATH, pcAOP), OSA Technical Digest (online), Optical Society of America, 2017, paper CTh4B.4.

X. Liu, F. R. Zaki, and Y. Wang, "Robust stiffness quantification using quantitative optical coherence elastography," In Conference on Lasers and Electro-Optics, Optical Society of America, 2017.

F. R. Zaki, I. Hou, D. Copper, D. Patel, Q. Huang, Y. Yang, and X. Liu**,** "Optical coherence tomography for non-invasive examination and conservation of cultural heritage objects," In Proc. SPIE 10110, Photonic Instrumentation Engineering IV, 101100F, 20 February 2017.

Y. Qiu, F. R. Zaki, N. Chandra, S. A. Chester, and X. Liu, **"**Characterization of nonlinear elasticity for biological tissue using quantitative optical coherence elastography**,**" In Proc. SPIE 10053, Optical Coherence Tomography and Coherence Domain Optical Methods in Biomedicine XXI, 1005324, 17 February 2017.

Y. Wang, Y. Qiu, F. R. Zaki, Y. Xu, B. Hubbi, K. D. Belfield, and X. Liu; "Entropy analysis of OCT signal for automatic tissue characterization," In Proc. SPIE 9720, High-Speed Biomedical Imaging and Spectroscopy: Toward Big Data Instrumentation and Management, 972018, 7 March 2016.

J. Y. Qiu, F. R. Zaki, Y. Wang, Y. Xu, N. Chandra, J. Haorah, B. Hubbi, B. Pfister, and X. Liu, "Depth resolved optical coherence elastography based on fiber-optic probe with integrated Fabry-Perot force sensor," In Conference on Lasers and Electro-Optics, OSA Technical Digest (online), Optical Society of America, 2016, paper AW1O.3.

S. Islam, F. R. Zaki, and M. Faisal, "Dispersion optimization of 160-Gb/s 2000-km transmission by appropriate orientation of chirped fiber Bragg grating," In 8th International Conference on Electrical and Computer Engineering (ICECE), 2014, pp. 417-420, December 2014.

F. R. Zaki, and M. Faisal, "Impact of third-order dispersion in ultra-high speed long-haul optical fiber communication system," In 2nd International Conference on Informatics, Electronics & Vision (ICIEV), 2013, pp.1-5, 17-18 May 2013.

Poster Presentations:

F. R. Zaki, Y. Wang, C. Wang, and X. Liu, "Adaptive doppler analysis for robust handheld optical coherence elastography," presented at BiOS Poster Presentation, SPIE Photonic West 2019, San Francisco, CA, 2019.

F. R. Zaki, X. Liu, H. Garg, and J. Rodriguez, "OCE quantification of Poisson's ratio through 2D speckle tracking," presented at BiOS Poster Presentation, SPIE Photonic West 2019, San Francisco, CA, 2019.

D. Renaud, F. R. Zaki, and X. Liu, "Development of spectral domain Doppler phase microscopy," presented at 2017 Summer Research Program Poster Presentation, New Jersey Institute of Technology, Newark, NJ, 2017.

I. Hou, F. R. Zaki, Q. Huang, and X. Liu, "Optical coherence tomography for non-invasive examination and conservation of cultural heritage objects," presented at 2016 Summer Research Program Poster Presentation, New Jersey Institute of Technology, Newark, NJ, 2016.

To my parents, Muhammad Zakiul Islam and Salma Zaki,

who encouraged me a lot

ACKNOWLEDGMENT

First, I would like to express my sincere and greatest appreciation to my dissertation advisor, Dr. Xuan Liu, for all her guidance, constant support, and encouragement throughout my Ph.D. journey. She not only guided me through my research, but also helped me enormously to be independent. I have not only gained the knowledge about my research arena but also learned professional communication skills from her. Her patience and understanding coupled with her experience have contributed to the successful completion of my studies.

I want to express my gratitude to all my dissertation committee members, Dr. Haim Grebel, Dr. Namas Chandra, Dr. Dong Kyun Ko, and Dr. Sagnik Basuray for their valuable suggestions. During my Ph.D. coursework, I took optoelectronics course taught by Dr. Haim Grebel. I am grateful to him for helping me understand the concepts of optical sources and detectors that are the key components for my experimental setup. I am thankful to Dr. Yun Q. Shi who helped me in understanding the basic fundamental concepts of image enhancement and image restoration techniques during my coursework of digital image processing that I have applied later during the signal processing of my experiments. I would also like to express my sincere gratitude to Dr. Namas Chandra, Dr. Maciej Skotak and Center of Injury Biomechanics, Materials and Medicine (CIBM3) for their guidance and support to perform experiments on bio-samples and helpful discussions for this research. Additionally, I would like to thank Dr. Namas Chandra for granting me research assistance during second semester of my Ph.D. studies.

In addition, I would like to thank my Ph.D. graduate advisor Dr. Durgamadhab Misra who encouraged and advised me for the last four years. I would like to express my

gratitude to all our funding agencies (National Institute of Health (NIH), start-up funding from New Jersey Institute of Technology (NJIT) and National Science Foundation (NSF)) to conduct this research. I would also like to thank ECE department of NJIT especially Dr. Leonid Tsybeskov, Dr. Mengchu Zhou, Ms. Monteria Bass, Ms. Joan M. Mahon and Ms. Ellen Stark for all their support throughout my entire Ph.D. journey. My appreciation also goes to Ms. Clarisa González-Lenahan, Dr. Sotirios G. Ziavras and the Office of Graduate Studies (GSO) of NJIT for providing me with valuable guidelines and assistance in formatting this dissertation.

I would like to thank my friend and my lab-mate, Yahui Wang for his enormous support in this journey. I would like to thank my all other lab members Dr. Yi Qiu, Dr. Jiangjun Wang, Haokun Wu and Chizhong Wang for inspiring me all the way. I am also grateful to Dylan Renaud, Qiongdan Huang, Mandar Malve, Xin Mei, Isabella Hou, Denver Cooper, Divya Patel, Dr. Yi Yang, Harshita Garg, Jonathan Rodriguez, Benjamin Litvin, Nishat Sadia and Jamia Gilles for their help and encouragement. I am also thankful to my friends and colleagues specially Farhan Azad Chowdhury, Mehnaz Mursalat, Manar Reza Chowdhury, Rakibul Hafiz, Mahbubur Rahman, Ishrat Ahmed Maureen, Humayra Tasnim Priyanka, Mahmuda Akter Munni, Masudul Hassan Quraishi, Imran Bin Azad, Abdul Quader, Fahmida Rahman and Tashfia Hoque for their encouragement throughout this journey.

Last, but not the least, I am thankful to my parents, Muhammad Zakiul Islam and Salma Zaki for their continuous inspiration, encouragement, support and guidance. Their beliefs have given me the courage to achieve my dreams. I would like to express my heartfelt gratitude to my sister Farhana Rahmat Zaki and my brother-in-law Saifur

Rahman Talukder for their support and encouragement throughout my endeavor. I am always grateful to my two lovable nieces, Eshal Saif and Parin Saif for making my life colorful.

TABLE OF CONTENTS

TABLE OF CONTENTS
(Continued)

Chapter **Page**

TABLE OF CONTENTS
(Continued)

Chapter **Page**

TABLE OF CONTENTS
(Continued)

Chapter **Page**

LIST OF TABLES

LIST OF FIGURES

TABLE OF FIGURES
(Continued)

Figure **Page**

TABLE OF FIGURES
(Continued)

Figure **Page**

TABLE OF FIGURES
(Continued)

Figure **Page**

TABLE OF FIGURES
(Continued)

Figure **Page**

TABLE OF FIGURES
(Continued)

Figure **Page**

NOMENCLATURES

Bandwidth	A range of frequencies within a given band for transmitting a signal.
Broadband light source	A light source with a broad optical bandwidth (typically 100nm or more).
Collimator	A device for producing a beam of parallel rays of light.
Common-path OCT	An OCT topology where the sample and the reference arms share the same path, therefore, no additional synchronization is required for the reference arm and the system is relatively insensitive to vibration as well as fiber induced polarization and dispersion mismatch.
Fabry Perot (FP) Cavity	A simplest form of plane-parallel optical cavity consisting of two reflecting mirror surfaces.
Fast Fourier Transform (FFT)	A mathematical method to transform the time domain to frequency domain. It is a discrete Fourier transform algorithm that reduces the number of computations required for N from $2N^2$ to 2N log (N).
Fiber-optic Coupler	A device used in optical fiber system with one or inputs and one or more output terminals.
Graphic Processing Unit (GPU)	A specialized electronic circuit designed to rapidly operate and modify memory to accelerate the formation of images in a frame buffer projected for output to a display device.
GRIN Lens	Graded index lens which is frequently used as a fiber coupling element. The lens has a gradient profile where the refractive index varies in the direction perpendicular to the optical axis.
Interference	In physics, interference is a phenomenon where two waves superimpose to generate a resultant wave of greater, lower, or the same amplitude.
Space Division Multiplexing OCT	The main purpose of this technology is to generate multiple imaging beams to illuminate the sample simultaneously, while maintaining optical delays in between each beam.

Spectral domain	Also known as frequency domain. It represents how much a signal lies within each assigned frequency over a range of frequencies.
Spectrometer	An optical instrument used for measuring wavelengths.

CHAPTER 1

INTRODUCTION

1.1 Motivation

There is a strong need for technologies that measures the mechanical properties of biological tissue. Microscopic mapping of tissue mechanical properties is critical for the diagnosis and treatment of a wide range of diseases including traumatic brain injury (TBI) and breast cancer. TBI, also known as intracranial injury that occurs due to injury to the central nervous system from physical trauma and damage to the central nervous system, is one of leading cause of death and disability around the world. TBI contributes to 30% of all injury deaths in USA [1]. However, data on mechanical properties of biological tissues are quite limited [147- 149]. In addition, values reported in literature are highly inconsistent [83]. Particularly, the Young's moduli of brain tissue reported in literature vary for several orders of magnitude (from kPa to GPa) [150]. The scarcity of data on tissue mechanical properties is due to technical limitations in current measurement methodologies. Breast cancer is the most common cancer among women (excluding nonmelanoma skin cancers) and is the second leading cause of cancer-related deaths for women in the United States. According to the surveillance research report of American Cancer Society, an estimated 60,290 new cases of breast cancer and 40, 290 deaths from breast cancer were expected in the United States in 2015 [2]. Although the death rates have declined significantly over the past two decades due to the improvement of public awareness and early detection of the disease, the diagnosis and treatment are far from perfection.

Conventionally, medical practitioners apply manual palpitation method on tissues as part of the screening and diagnosis of breast cancer (such as stiffness) [3]. However, manual palpitation provides the qualitative measurement of tissue mechanics properties. In recent years, a new branch of imaging techniques, known as elastography, has been developed for better characterization of the tissue pathologies quantitatively. Elastography is a medical imaging modality that tracks the tissue deformation upon an applied mechanical load and relates the tissue deformation, typically elasticity, which is then mapped into an image, known as elastogram. For example, tumor and cancer tissues are often stiffer than the healthy ones. Currently, elastography is commercially applied in ultrasound elastography (URE) and magnetic resonance imaging (MRI) as a diagnostic tool for the assessment of breast lesions [4] and liver fibrosis [5]. Meanwhile, the spatial resolution of these techniques is limited from few hundred micrometers (μm) to several millimeter (mm) ranges allowing the visualization of macroscale level visualization of tissue features.

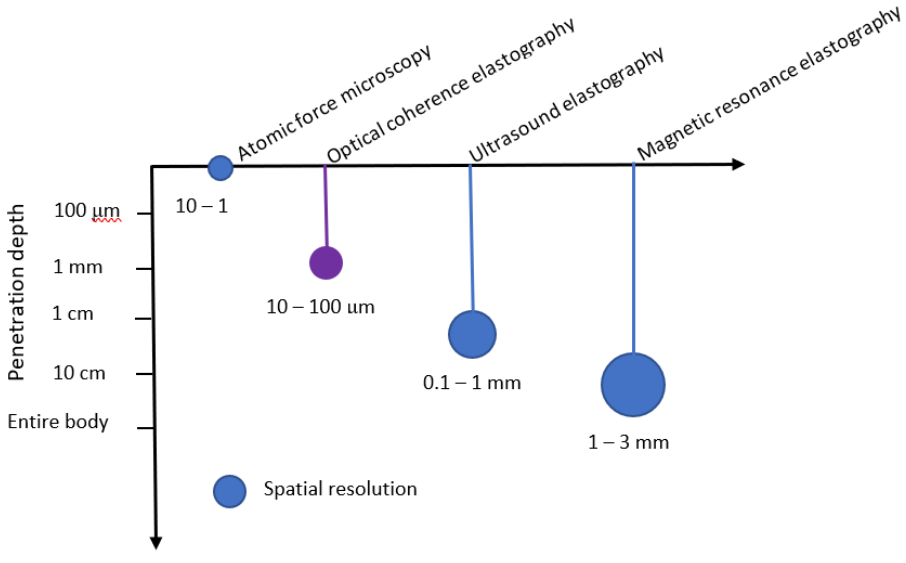

Figure 1.1 Scales of different elastography techniques.
Source: [6]

Meanwhile, elastography by atomic force microscopy (AFM), can explore the cellular scale (nanometers to micrometers). Yet, this technique lacks the capability to measure tissue mechanical properties in the range of micrometers to millimeters—a vital scale between that of cells and whole organs in order to reveal the microscopic progression of cancer tissue detection at early stage. Therefore, a technology for *in situ*, microscopic characterization of breast tissue is urgently needed for improved diagnosis and treatment of breast cancer. Optical coherence elastography (OCE) can bridge the gap. Scales of different elastography methods based on penetration depth and imaging spatial resolution are presented in Figure 1.1.

Optical Coherence Elastography (OCE) is a functional extension of Optical Coherence Tomography (OCT), which is a cross-sectional imaging modality based on low coherence light interferometry. Compared to conventional macroscopic medical imaging modalities, OCT has high spatial resolution (1μm - 10μm) to reveal fine structural details of biological tissue. In addition, OCT also provides extremely high imaging speed (typically faster than 100, 000 A-scans per second, or 100 B-scan frames per second) to assist clinical decision making in real-time. In breast cancer management, OCT can be used in both structural imaging and mechanical characterization. However, *in situ* structural OCT imaging alone has limited efficacy in distinguishing normal breast tissue from diseased breast tissue because OCT signal is obscured by photons with multiple scattering events and speckle noise. Hence, there is a need to integrate additional imaging/sensing capabilities with structural OCT imaging for its translation to clinical applications. In addition to morphological difference, cancerous breast tissue usually has higher stiffness compared to normal breast tissue, which is a compelling reason for the specific

combination of structural OCT imaging with stiffness assessment in the proposed dual-modality OCT characterization of breast tissue.

The most frequently used parameter that describes the elasticity of a material is the Young's modulus measured at small strains. The Young's modulus can be directly measured using the stress-strain relationship through a compression process. Researchers also investigated indirect methods to quantify the Young's modulus of tissue. One of the indirect measurement technologies is dynamic elastography that generates dynamic excitation and propagating mechanical wave in tissue [11, 12]. In dynamic OCE, OCT imaging system is used to measure the propagation parameters of shear wave or surface wave for the estimation of Young's modulus. The mechanical excitation in dynamic OCT can be introduced by focused ultrasound or by photothermal effects, providing great opportunity for loading at depth. Nevertheless, indirect measurement of tissue Young's modulus has limited spatial resolution and limited access to deep tissue. Conventional compression OCE that measures spatially resolved tissue displacement under compression has the potential to achieve high spatial resolution and can be implemented as an instrument with a small form factor. However, conventional compression OCE lacks the mechanism for force or stress quantification. This can limit its application in tissue characterization, because most of the biological tissues have different elastic behavior under large loads as compared to small loads. Strain stiffening is frequently observed in biological tissue at large loads, and the linear stress-strain relationship is limited to few tissues such as bone tissue in a very limited deformation regime. In other words, the displacement of tissue measured by OCE not only depends on the mechanical characteristics of the tissue, but also depends on the magnitude of loading [13]. Therefore, it is critical for OCE measurement

to consider both the linear and nonlinear elasticity of tissue quantitatively to achieve effective tissue differentiation, which has not been investigated extensively before [14].

For the development of the dual modality OCT system, the structural OCT images suffer from additive and multiplicative noises that degrade the image quality. To suppress noise in OCT imaging, a noise adaptive wavelet thresholding (NAWT) algorithm has been developed to remove the speckle noise in OCT images. NAWT algorithm characterizes the speckle noise in the wavelet domain adaptively and removes the speckle noise while preserving the sample structure. Furthermore, a novel denoising algorithm is also developed that adaptively eliminates the additive noise from the complex OCT using Doppler variation analysis.

In summary, pathological tissue has altered microarchitecture which can be characterized by the structural OCT imaging. Moreover, pathological tissue has altered mechanical properties which can be assessed by OCE technique. Therefore, the dual modality (structural and mechanical) measurement of OCT integrates the structural OCT imaging with stiffness assessment of OCE and allows more accurate characterization of biological tissues.

1.2 Background Information

1.2.1 Light-tissue Interactions/Tissue Optics

Light is an electromagnetic wave. Typically, OCT imaging in nontransparent tissue is performed in the near-infrared region. Elastic light scattering is considered as the most important light-tissue interaction that generates OCT signal. Light scattering is generated from the spatial heterogeneity distribution of the optical refractive index. Optical refractive index depends on the spatial distribution of local mass density and constituent of a tissue

(i.e., lipid membrane, collagen fibers, the size of nuclei, hydration status in the tissue, etc).

A simple relationship between the optical refractive index and the local molecular density of the tissue is given as:

$$n = n_0 + \alpha\rho \tag{1.1}$$

where n_0 indicates the refractive index of the liquid medium (i.e., water), ρ is the fractional volume of the tissue solids such as proteins, DNA, RNA, lipids, etc. and can vary from 0 to 1 and α is the proportionality constant. All these quantities are dependent to wavelength of light [151].

The process of light scattering can be defined with the help of an electromagnetic wave. Let's consider an electromagnetic wave of a unit magnitude propagating in the z_0 direction through the sample where the refractive index varies. The scattering particle will generate a spherical wave $E_z(\mathbf{r})$ located at **r** position in the direction of z = **r**/r, where r =|**r**|. The generated spherical wave is:

$$E_z(\boldsymbol{r}) = \boldsymbol{g}(\boldsymbol{z}, \boldsymbol{z_0}) \frac{e^{jkr}}{r} \tag{1.2}$$

where $\boldsymbol{g}(\boldsymbol{z}, \boldsymbol{z_0})$ represents the scattering amplitude and is also a complex vector component.

The most commonly used term to describe the characteristics of scattering property is the scattering cross-section. Scattering cross-section is the geometrical cross-section of a particle that produces the equal quantity of scattering and scattered power observed in a solid angle of Ω from all sides of the particles and can be expressed as:

$$\sigma_s = \int_0^{4\pi} |\boldsymbol{g}(\boldsymbol{z}, \boldsymbol{z_0})|^2 \, d\Omega \tag{1.3}$$

A relative quantity, the total cross-section (σ_t) is defined as:

$$\sigma_t = \sigma_s + \sigma_a \tag{1.4}$$

where σ_a is the absorption cross-section.

In tissue optics, the absorption and scattering coefficients represent the overall attenuation experienced by the sample due to the light propagation. Absorption of light provides information about the chemical composition of a tissue and can provide information such as tissue oxygenation, oxygen consumption, blood hemodynamic, etc. [15]. Generally, when an electron interacts with the light, a photon energy at specific frequency is absorbed and is moved to a higher energy state. The attenuation causes an exponential decay of the incident light intensity with the penetration depth. Penetration depth measures the depth that light can penetrate through a sample tissue and it depends on the absorption and scattering properties of the biological specimens.

For biological applications, OCT system typically use the near-infrared wavelengths and hereby, the optical response of the tissue is generally governed by the scattering phenomena rather than the absorption. OCT, therefore, provides good penetration depth and uses the coherence gating detection scheme to reject the undesired multiple scattered lights. Additionally, OCT provides micron-scale resolution with imaging contrast based on intrinsic sample properties, i.e., the scattering potential. This makes the extensive use of OCT imaging system for the retinal imaging [153- 155].

1.2.2 Introduction to Optical Coherence Tomography (OCT)

Tomographic technique generates slices of images from the three-dimensional objects and has a great impact on medical field imaging due to its capability for producing non-invasive diagnostic images from the sample tissues. In early 90´s, Huang *et al*. [16] applied the low coherence interferometry principle to generate the high resolution, cross-sectional tomographic images of biological tissues by measuring the echo time delay and magnitude

of backscattered light. The technique is known as Optical Coherence Tomography (OCT). Imaging was performed *ex vivo* in the human retina and in atherosclerotic plaque as examples of imaging in transparent, weakly scattering media and in highly scattering media. Figure 1.2 shows the early OCT images. Imaging experiment was performed with an infrared light of 800nm wavelength. These early OCT images had an axial image resolution of ~15μm, which introduces almost one order of magnitude better for clinical imaging opportunity than standard ultrasound imaging technique.

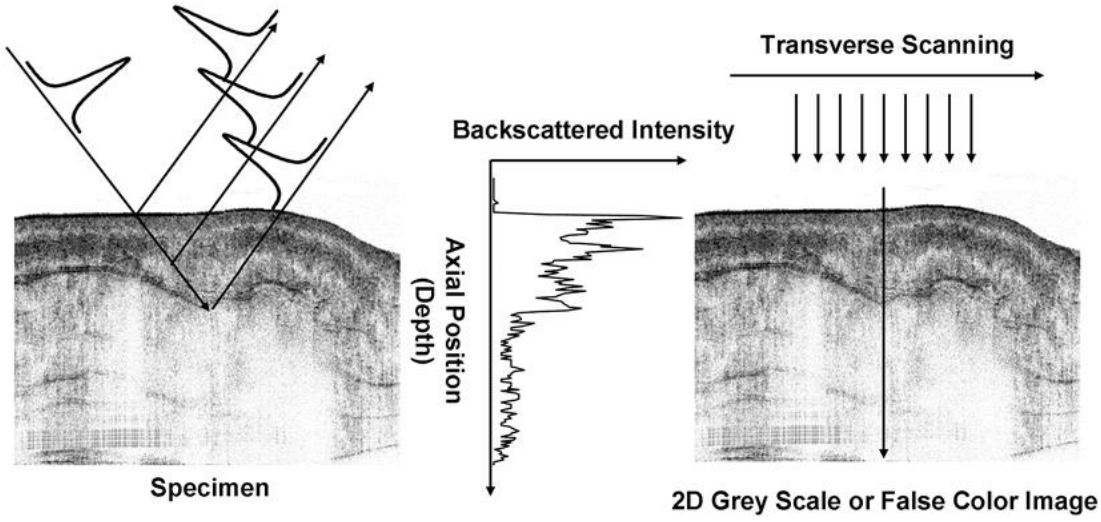

Figure 1.2 Generation of cross-sectional images by OCT through the measurement of the magnitude and echo time delay of backscattered light from the different transverse positions. A two-dimensional data set is displayed as a grayscale or false color image.
Source: [16]

Now-a-days, OCT has become an optical imaging modality for biomedical research and clinical applications in several areas, e.g., ophthalmology, dermatology, oncology, etc. Compared to conventional macroscopic medical imaging modalities, OCT has high spatial resolution (1μm - 10μm) to reveal fine structural details of biological tissue. In addition, OCT also provides extremely high imaging speed (typically faster than 100, 000 A-scans per second, or 100 B-scan frames per second) to assist clinical decision making in real-

time.

1.2.2.1 Coherence and interference. Coherence is important in understanding OCT. In physics, two wave sources are said to be coherent if they have a constant phase difference with the same frequency and the same waveform. Coherence is an ideal property of waves that enables stationary (i.e. temporally and spatially constant) interference.

Interferometry measures the echo time delay of the backscattered light with high sensitivity and high dynamic range. OCT uses the interference to measure the backscattered signal intensity indirectly through the use of an interferometer. Therefore, a reference arm is required as the back-reflection intensity cannot be measured directly due to the high speed associated with the propagation of light. A Michelson interferometer will be discussed to present the interferometry and coherence concept.

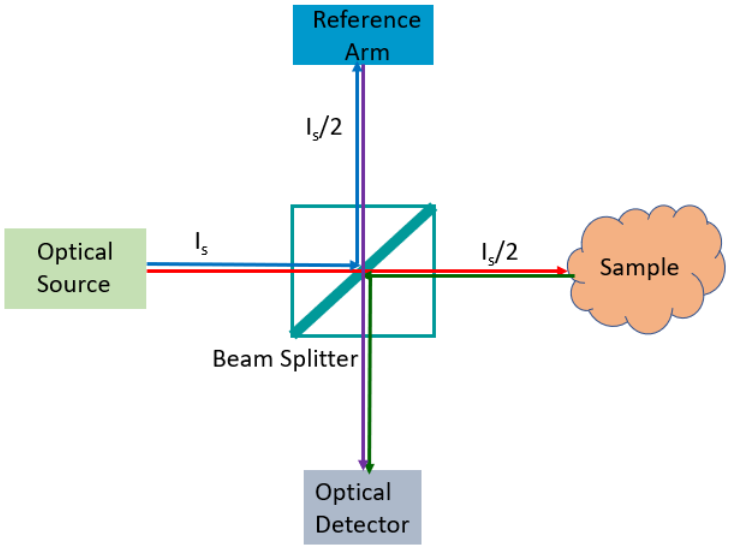

Figure 1.3 Schematic representation of a Michelson interferometer.

A schematic of the interferometer is shown in Figure 1.3. The system comprises of three main parts: optical source, scanning system and optical detector. The light emitted

from the optical source with low coherence length is divided from the beam-splitter to the sample and reference arm. Next, the backscattered lights from the sample and the reference arms are recombined at the beam-splitter and the generated interference patterns are detected by the optical detector. According to the broadband properties of the optical source, the interference fringes will appear only when the optical path difference between the two arms are nearly identical and are matched to within the coherence length as shown in Figure 1.4(a). The coherence length (l_c) is a measure of the coherence and is inversely proportional to the frequency bandwidth. In OCT imaging, the coherence length determines the axial or depth resolution.

For path length mismatches greater than the coherence length as shown in Figure 1.4 (b), the electromagnetic fields from the two beams are uncorrelated and no interference would be occurred. The magnitude and echo time delay of the reflected light can be measured by scanning the reference mirror delay and demodulating the interference signal from the interferometer. Because the interference signal is measured as a function of time and echoes are measured sequentially, this detection technique is also known as time domain detection.

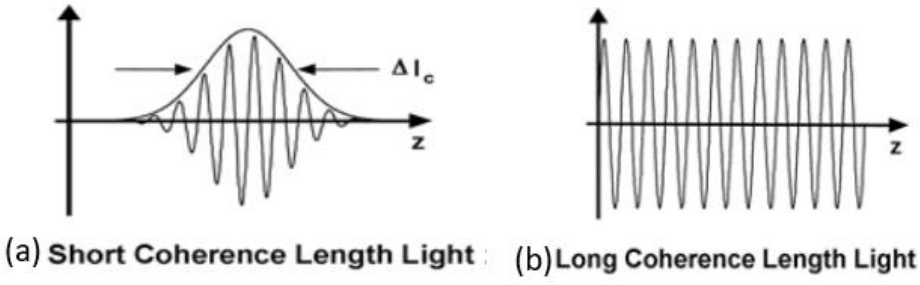

Figure 1.4 Two types of coherence length
Source: [16]

1.2.2.2 Interferometric techniques for OCT imaging system Optical

coherence tomography uses interferometry to perform high-resolution measurements of light echoes. Two different types of interferometric detection techniques are used in OCT instruments: time domain OCT (TD-OCT), Fourier domain OCT (FD-OCT).

In TD-OCT system, a broadband light source is used. Due to the low coherence of the light source, the interference signal is obtained only when the optical path length of the sample and reference arm is matched to within the narrow coherence length. The reference arm is then scanned to match the optical path length of the reflections from within the sample. The recorded interference signal at different depths or relative time delays between reference and sample is then demodulated to generate a reflectivity depth profile or A-scan as shown in Figure. 1.5(a).

In FD-OCT systems, the interference signal is distributed and integrated over many spectral slices, and is inverse Fourier transformed to obtain the depth-dependent reflectivity profile of the sample. The main advantage of FD-OCT is that, once that a CCD based spectrometer is used, there is no need of any mechanical scanning for depth resolved imaging. All the depth information and the scattering profile are encoded in the spectral interference pattern, which is further processed easily by a personal computer. Therefore, the position of the reference arm is fixed. Hence, FD-OCT system provides a higher scan speed compared to TD-OCT. However, in FD-OCT, the detector cost is high and complex and the FD signal needs additional signal processing with powerful computers.

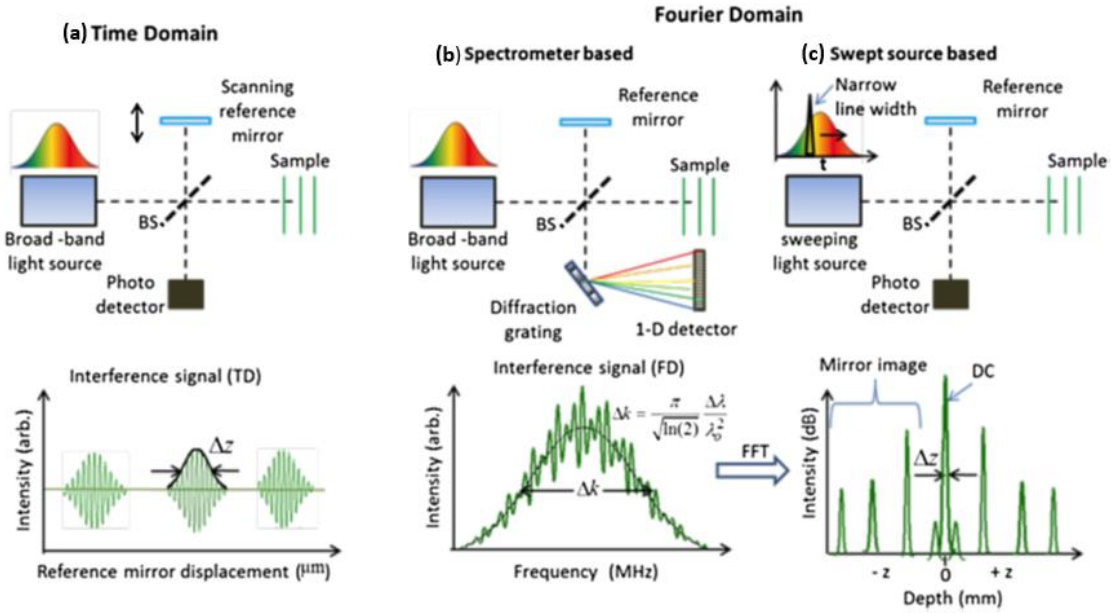

Figure 1.5 Schematic of different OCT modalities: (a) Time domain OCT (TD-OCT), two different Fourier domain OCT (FD-OCT); (b) Spectral domain OCT (SD-OCT); (c) Swept source OCT (SS-OCT).
Source: [17]

There are two types of Fourier domain detection schemes: spectral domain OCT (SD-OCT) and swept source OCT (SS-OCT). Both instruments use Fourier domain detection techniques. The SD-OCT instrument uses a broadband near-infrared superluminescent diode (SLD) as a light source and a spectrometer as the detector. The interference signal is split into different optical frequencies using a diffraction grating and is then detected through a one-dimensional (1-D) CCD array as shown in Figure. 1.5(b). Resampling of the data obtained from the CCD array is performed in order to correct the nonlinear spatial mapping of wavenumbers. After resampling and subtraction of the DC background, the depth-resolved structural profile information can be obtained by performing the inverse Fourier transform.

In SS-OCT, the system uses an interferometer with a narrow instantaneous bandwidth, frequency-swept light source. The light source sweeps through a range of wavelengths and measures the interference output as a function of time by a single

photodiode as the detector. The collected signal obtained from the detector is equivalent to the SD-OCT technique. Then Fourier transform is performed to the detected intensity spectrum to generate the depth-resolved reflectivity profile (A-scan) of the sample as shown in Figure 1.5(c). In SS-OCT, the setup does not require any moving mirrors, no gratings and CCDs. SS-OCT systems are advantageous for their tremendously fast scanning speeds, in the range of 50kHz to several MHz axial scans per second.

1.2.2.3 Mathematical derivation of the interference signal at the detector for OCT

In SD-OCT system, an electrical field amplitude of the optical source (E_i), defined by Equation (1.5), is applied to the beam-splitter which splits the radiation to the sample (E_s) and reference arm (E_r).

$$E_i = S(k,\omega)e^{(kz-\omega t)} \tag{1.5}$$

where z = Sample depth

k = Wave number = $\frac{2\pi}{\lambda} = \frac{\omega}{c}$

ω = Angular frequency

As the sample consists of multiple layers, for the discrete reflection, we have:

$$r_s(z_s) = \sum_{n=1}^{N} r_{sn}\,\delta(z_s - z_{sn})$$

E_s and E_r can be expressed as Equations (1.6) and (1.7), respectively.

$$E_s = \frac{E_i}{\sqrt{2}}\left[r_s(z_s) \otimes e^{i2kz_s}\right] = \frac{E_i}{\sqrt{2}}\sum_{n=1}^{N} r_{sn}e^{i2kz_{sn}} \tag{1.6}$$

$$E_r = \frac{E_i}{\sqrt{2}}\, r_r e^{i2kz_r} \tag{1.7}$$

The intensity on detector (I_d) is proportional to square modulus of the sum of the electric fields of sample and reference arm:

$$I_d(k,\omega) = \frac{\rho}{2} |E_r + E_s|^2$$

$$= \frac{\rho}{2} \left| \frac{S(k,\omega)}{\sqrt{2}} r_r e^{i(2kz_r - \omega t)} + \frac{S(k,\omega)}{\sqrt{2}} \sum_{n=1}^{N} r_{sn} e^{i(2kz_{sn} - \omega t)} \right|^2 \quad (1.8)$$

By elimination the ω terms, Equation (1.8) will become:

$$I_d = \frac{\rho}{4} [S(k)(R_R + R_{s1} + R_{s2} + R_{s3} + \cdots)] + \frac{\rho}{4} \left[S(k) \sum_{n=1}^{N} \sqrt{R_{sn} R_R} \left(e^{i2k(z_r - z_{sn})} + e^{-i2k(z_r - z_{sn})} \right) \right] + \frac{\rho}{4} \left[S(k) \sum_{n \neq m=1}^{N} \sqrt{R_{sn} R_{sm}} \left(e^{i2k(z_{sn} - z_{sm})} + e^{-i2k(z_{sn} - z_{sm})} \right) \right] \quad (1.9)$$

Equation (1.9) contains three terms that contribute to the total OCT signal intensity: DC term, cross-correlation term and the auto-correlation term, respectively. The DC term is generated from the sample and reference reflectivities. The cross-correlation term is formed from the interference of the sample and reference arms and the auto-correlation term is obtained due to the sample path difference.

From Equation (1.9), it is found that as I_d depends on k, Fourier transform can be applied to obtain the signal depth. For an arbitrary cosine function:

$$\cos(kz_0) \overset{Fourier\ transform}{\Longleftrightarrow} \frac{1}{2} [\delta(z + z_0) + \delta(z - z_0)] \quad (1.10)$$

After applying the Fourier transform on I_d, Equation (1.9) can be reduced to

$$I_d = \frac{\rho}{8} [\gamma(k)(R_R + R_{s1} + R_{s2} + R_{s3} + \cdots)] + \frac{\rho}{4} \left[\sum_{n=1}^{N} \sqrt{R_{sn} R_R} \left[\gamma\left(2(z_r - z_{sn})\right) \right] + \gamma(-2(z_r - z_{sn})) \right]$$

$$+ \frac{\rho}{4} \left[\sum_{n \neq m=1}^{N} \sqrt{R_{sn} R_{sm}} \left[\gamma\left(2(z_r - z_{sn})\right) \right] + \gamma(-2(z_r - z_{sn})) \right] \quad (1.11)$$

1.2.2.4 Performance analysis of OCT system

(a) Image resolution of OCT:

OCT system has two kinds of resolution: axial resolution and lateral (transverse) resolution.

The axial image resolution in OCT is determined by the coherence length of the light source. The coherence length is proportional to the width of the field autocorrelation measured by the interferometer, and the envelope of the field autocorrelation is related to the Fourier transform of the power spectrum. For a Gaussian-shaped spectrum, the axial resolution (Δz) can be defined as:

$$\Delta z = \frac{2\ln(2)}{\pi} \frac{\lambda_0^2}{\Delta\lambda} \tag{1.12}$$

Here, Δz is the full-widths-at-half-maximum (FWHM) of the autocorrelation function, λ_0 is the center wavelength of the light source and $\Delta\lambda$ is the bandwidth of the light source, respectively. Choice of light source (λ_0 and $\Delta\lambda$) affects Δz and also the penetration depth of the sample tissue. As axial resolution is inversely proportional to the bandwidth of the light source, broad bandwidth optical sources are required to achieve high axial resolution.

The transverse or lateral resolution in OCT imaging is determined by the diffraction-limited spot size of the focused optical beam. The diffraction-limited minimum spot size is inversely proportional to the numerical aperture (NA) or the focusing angle of the beam. The transverse resolution (Δx) is given as:

$$\Delta x = \frac{4\lambda}{\pi} \left(\frac{f}{d}\right) \tag{1.13}$$

where d is the spot size on the objective lens, f is its focal length of the lens and NA = d/f. A better performance of lateral resolution can be achieved by using a larger NA that focuses the beam to a small spot size. Typically, OCT imaging is performed with low NA focusing to have a large depth of field.

(b) Sensitivity of OCT:

Interference amplifies weak signals and hence increases sensitivity of the system. An important feature of an OCT system is the weakest sample reflectivity ($R_{s,min}$) that provides

a signal power equal to the noise of the system. Therefore, Sensitivity (S) can be defined as the ratio of the signal power generated by a perfectly reflecting mirror ($R = 1$) and that generated by $R_{s,min}$. Since these signal powers are proportional to the corresponding reflectivities we have:

$$S = \frac{1}{R_{s,min}}\Big|_{SNR=1} \tag{1.14}$$

Standard OCT devices use ac detection. As most amplifiers display flicker noise ($1/f$ noise; with typically 3dB per octave slope) in the low frequency range, frequencies more than 10kHz are used. The dominating noise sources are shot noise, excess intensity noise and receiver noise. In the interim region, shot noise governs and the sensitivity can be expressed as:

$$S = \frac{\alpha}{4}\frac{P_s}{q_e B} \tag{1.15}$$

Here, $\alpha = \frac{q_e \eta}{h\nu}$, q_e is the electron charge, η is the quantum efficiency, $h\nu$ is the photon energy, P_s is the source power and B is the bandwidth of the light source. So, sensitivity is proportional to the source power and is inversely proportional to the electronics bandwidth. In OCT system, at lower power, receiver noise limits the sensitivity of the system and at higher power no additional sensitivity are added due to the presence of excess noise.

1.2.2.5 Image generation and display of OCT system OCT data can be collected and displayed in a number of different formats. The most common three types of formats are A-scan, B-scan and C-scan images in OCT. Each form represents a unique way to visualize the test sample.

(a) A-scan OCT image:

A-scan OCT image generates the reflectivity or depth-resolved profile of the sample being scanned. It generates the intensity of the reflected light at various depths for a single sample location. It contains information about the spatial dimensions and location of the sample structures within the region of interest. Figure 1.6(a) shows the A-scan image of a sample object. It represents the intensity of the backscattered signal from the sample as the varying depth in the axial direction.

(b) B-scan OCT image:

B-scan OCT image provides a two-dimensional graphical presentation. It generates a cross-sectional image of the sample by axially scanning and combining the series of A-scan images sequentially. Figure 1.6(b) shows the B-scan or cross-sectional image of a fingertip of a healthy volunteer.

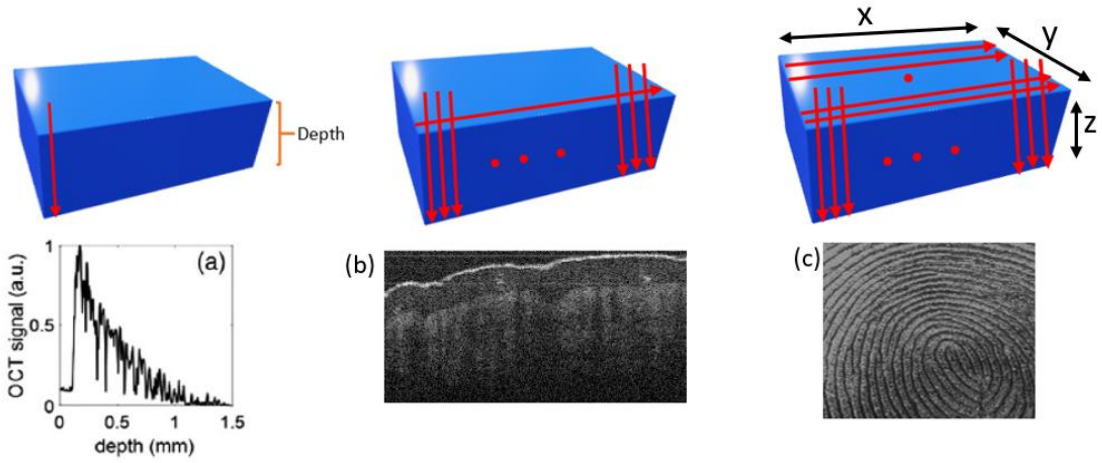

Figure 1.6 Different image display in OCT: (a) A-scan, (b) B-scan or cross-sectional image, (c) C-scan image. Here, human fingertip is used as sample to acquire the images. *Source: [18-19]*

(c) C-scan OCT image:

C-scan image generates 3D image of the sample by performing the lateral scanning and the

combining the B-scan images sequentially. Using the 3D data cube, an *enface* image is formed. Figure 1.6(c) shows an *enface* image of a fingertip of a healthy volunteer. From the figure, the ridges and valleys of the fingerprint are visible clearly.

1.2.3 Speckle Analysis in OCT

Speckle is an intrinsic feature of images appearing in all types of coherent imaging systems, such as ultrasound, synthetic aperture radar, optical holography and OCT. Speckle is often considered as a granular-textured noise. Speckle noise imposes the fundamental limitation on image quality for OCT. It obstructs the structural features and makes it challenging to extract information (such as structural property of a sample) from an OCT image. Therefore, a lot of research work is going on to suppress this speckle effects by reducing the speckle contrast ratio of the image. However, the main limitation is due to the fact that "speckle" and "structure" cannot be easily separated.

In OCT, speckle is produced by the addition of multiple optical wavefields, backscattered from the sample arm of an interferometer. A speckle pattern in a B-scan FD-OCT image is presented in Figure 1.7 [20].

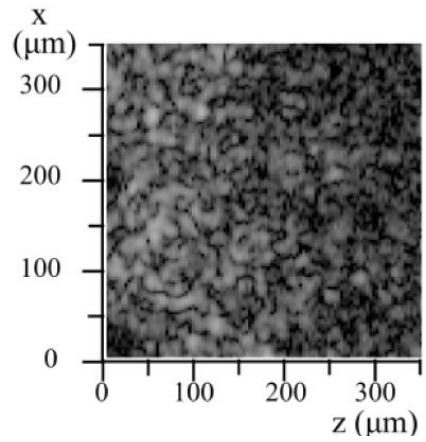

Figure 1.7 A speckle pattern in a B-scan FD-OCT image.
Source: [20]

In OCT, speckle is distinct from noises (such as intensity, shot and phase noises determined by the imaging system, that depend on the source and detection scheme properties). In fact, speckle formation is sample dependent and time invariant. For instance, if the sample is motionless with respect to the probing beam, then speckle plays a vital role for the formation of OCT images. Hence, in this situation, complete removal of speckle would cause with no OCT image at all [21]. Speckle in a single backscattering scenario can be modeled as the difference between the coherent and incoherent images of a highly random microstructure modulated by a slowly varying "mean" function. [22]

1.2.3.1 Mathematical Analysis of Speckle In this section, only the signal arising due to single scattering, by first order Born-approximation scattering is considered [23] in which the sample is denoted as superposition of non-interacting phase gratings. Thereby, for monochromatic light, the scattered wave depends linearly on the sample's scattering potential for any incident wave is:

$$S_S(\boldsymbol{r}, k_\lambda) = \frac{k_\lambda^2(n^2(\boldsymbol{r})-1)}{4\pi} \tag{1.16}$$

Where n(**r**) represents the refractive-index, **r** is a three-dimensional spatial location vector, k_λ represents wavenumber at a particular λ

For simplicity, assuming the refractive index is wavenumber-independent (neglecting dispersion effect of the sample), sample susceptibility can be considered to discard the wavenumber dependency from the calculation, as [24]

$$\chi(\boldsymbol{r}) = (n^2(\boldsymbol{r}) - 1) = \frac{S_S(\boldsymbol{r})4\pi)}{k_\lambda^2} \tag{1.17}$$

In particular, the scattering potential represents as

$$\chi(\boldsymbol{r}) = P(\boldsymbol{r})N(\boldsymbol{r}) \tag{1.18}$$

where P is a slowly varying non-negative deterministic function denoted as the macroscopic variations in the sample and N is a rapidly varying complex ergodic random process function represented as the microscopic scatterer distribution within the macroscopically locally homogeneous regions and can be approximated as Dirac delta function, δ(**r**). The terms "Slowly" and "rapidly" varying in this section is considered with respect to the spatial scale of the OCT PSF envelope.

The detected OCT signal, as a function of scan position, is given by the superposition integral:

$$A\,(\boldsymbol{r}) = \iiint_{-\infty}^{\infty} \chi(\boldsymbol{r}')B(\boldsymbol{r}-\boldsymbol{r}';\,\boldsymbol{r})d^3\boldsymbol{r}' \tag{1.19}$$

where B(a, **r**) is the local system PSF.

However, if the imaging system is spatially invariant for one-dimensional, then Equation (1.19) is a convolution integral, A (**r**) = χ(**r**) ⊗ B(**r**), so that B(a; **r**) ≡ B(a). It means that the OCT PSF can be assumed to be spatially invariant when performing enface imaging.

Consider, N is a Delta-dirac function. The integral of N over its entire domain is 1. The mean value $\overline{A(\boldsymbol{r})}$ = 0, due to the random phase of N. This simple statistic provides a clarification for the speckle phenomenon. So, the total OCT signal is due to fluctuations about this zero-mean point.

The mean-squared value of A(r) by the sifting property of the delta function is:

$$\overline{|A(r)|^2} = \iiint_{-\infty}^{\infty}\iiint_{-\infty}^{\infty}\overline{\chi(r')\chi^*(p')}\;B(r-r';\,r)B^*(r-\,p';r)d^3r'd^3p'$$

$$\cong\; |P(r)|^2 \iiint_{-\infty}^{\infty}|B(\boldsymbol{r}';\boldsymbol{r})|^2 d^3\boldsymbol{r}' \tag{1.20}$$

The factor |P(**r**)|^2 is taken outside the integral due to the assumption that it is slowly

varying (in comparison with the size of $|B(\mathbf{r_0; r})|^2$).Now for an incoherent imaging system (hypothetical equivalent) which is linear with respect to optical intensity, the detected signal by the convolution integral is:

$$F(\boldsymbol{r}) = \iiint_{-\infty}^{\infty} |\chi(\boldsymbol{r}')|^2 |B(\boldsymbol{r} - \boldsymbol{r}';\ \boldsymbol{r})|^2 d^3\boldsymbol{r}' \tag{1.21}$$

The variance of F is zero under the delta-function limit. So, F (r) can be expressed as:

$$F(\boldsymbol{r}) = \overline{F(\boldsymbol{r})} = |P(\boldsymbol{r}')|^2 \iiint_{-\infty}^{\infty} |B(\boldsymbol{r}';\ \boldsymbol{r})|^2 d^3\boldsymbol{r}' \tag{1.22}$$

Equations (1.20) and (1.22) reveal the origin of speckle in coherent imaging. The incoherent image $F(\mathbf{r})$ represents the exact reconstruction of $|P(\mathbf{r})|^2$, equal to its mean (deterministic) value, and is independent of the small-scale fluctuations caused by N(r). Furthermore, both the squared modulus of the coherent complex amplitude distribution ($\overline{|A(\boldsymbol{r})|^2}$) and the incoherent intensity distribution ($F(\boldsymbol{r})$ show same mean value.

Based on the prior analysis, speckle can be defined as the difference between a coherent image $|A(\mathbf{r})|^2$ and the corresponding incoherent image F ($\mathbf{r}$) considering that the imaging process can be modeled by a superposition integral [22].

In OCT, if we represent the sample as a collection of point scatterers, then the OCT signal can be expressed as [22]:

$$A = |A|e^{j\theta_A} = \sum_{i=1}^{M} A_i = \sum_{i=1}^{M} a_i e^{j\phi_i} \tag{1.23}$$

Where A_i indicates the phasor influence of i-th scatterer of total M components to the signal. The term |A| is known as speckle envelope. Assuming, the scatteres are identical, the distribution of a_i depends only on the shape of the local point-spread function (PSF). PSF of an imaging system indicates the response of a point source. Moreover, all the values of a_i and ϕ_i are independent [156].

Therefore, the speckle envelope is Rayleigh-distributed and the speckle size remains almost constant over the entire A-scan image [22]. Additionally, the OCT PSF has pulse broadening effect in the axial direction of the sample with the increase of sample depth in the presence of dispersion. However, in SD-OCT system, low NA is considered for selecting the lens of the sample arm. As a result, OCT signals are not affected by the dispersion and the speckle size will remain the same [157]. Moreover, as the phase contribution of different scatterers to OCT signal varies over the A-scan, this variation maintains the dispersion-free speckle correlation function, even if the axial resolution of the image degrades [22].

1.2.3.2 Speckle Reduction Methods Speckle suppression methods can be classified into two categories: 1) based on the modification of the experimental setup and 2) post-processing of the recorded OCT images.

In experimental methods, multiple images are captured under different detection schemes or illumination techniques. The main purpose of these methods is to obtain the uncorrelated speckle patterns from the local region that corresponds to the same region of interest (ROI). For example, Angle compounding approach uses speckle averaging in OCT using summation of A-scan envelope signals from an array of detectors [21]. An illumination direction diversity method [25] can be applied for speckle-reduction technique for enface OCT images. Some other experimental methods include the illumination center wavelength [26]; the detection angle [27-30], the beam focal position [31-32] and strain induced in the sample [33-34].

Post-processing techniques are flexible for OCT speckle suppression. Speckle reduction algorithms are applied to extract useful sample information from speckle-

corrupted images and suppress image-distorting effects. The first image postprocessing technique for speckle suppression in OCT has used a wavelet filter [35]. Many methods have been proposed, for instance, averaging filters [21], wavelet transforms [36] and anisotropic diffusion [37]. However, the averaging filter technique degrades the spatial resolution [22]. In wavelet transform filtering methods, the signals are decomposed into wavelet coefficients. Based on the magnitudes of coefficients, a spatially adaptive threshold estimator classifies the signal either as information or speckle noise. Wavelet transform can reduce the speckle while preserving the spatial resolution of the image.

1.2.4 Introduction to Optical Coherence Elastography (OCE)

Optical coherence elastography (OCE) was first introduced by Schmitt in 1998 [38]. OCE shows great potential for micron and submicron imaging applications because it benefits from the high resolution of OCT, while additionally providing the elastic properties of the sample. OCT provides structural images that are similar to histology, where the microstructures of biological tissues can be quantified based on the optical backscattering properties within the imaging region of interest. This high-resolution, noninvasive imaging modality allows OCE to evaluate the mechanics of intact tissue on microscopic scale. OCE has a number of advantages over ultrasound elastography and magnetic resonance elastography, such as: spatial resolution, sub-nanometer displacement sensitivity and fast image acquisition speed. Table 1.1 shows the comparison of various elastography techniques based on performance evaluation. OCE has the ability to generate high-resolution and high-contrast elastograms. Therefore, current research interests are focusing on the key advances to enable clinical OCE, feasible imaging probes integrated with loading instruments, and better contrast realization in pathological tissue.

Table 1.1 Performance Evaluation of Elastography Techniques

Techniques	Resolution	Imaging depth	SNR (dB)	Imaging Speed
Magnetic Resonance Elastography	1.3mm	Whole body	5 - 14	2 – 20min
Ultrasound Elastography	0.1 – 0.5mm	4-5cm	8 - 12	4 - 30μs
OCE	15 - 100μm	0.5 – 3mm	10 -25	20 - 100μs
Brillouin Microscopy	0.5 - 5μm	0.1 – 3mm	10 - 30	2 – 5min
Atomic Force Microscopy	1-100nm	Surface only	10 -33	30s – 30mins

Source: [39]

There are three main steps to perform the OCE, which is given as follows:

(1) Identification of the structural characteristics of the sample tissue (i.e., isotropic or anisotropic) and establishment of an appropriate theoretical relationship with appropriate boundaries to connect the applied forces to strains or deformations.

(2) Design of appropriate experimental methods to perform the experiment and also the detection scheme to identify the tissue deformation for the theoretical framework.

(3) Obtain the stress-strain relationship and hence, calculate the elastic modulus.

1.2.4.1 Mechanical Properties of Tissue Elastography maps local mechanical properties, such as stiffness or elasticity, from a set of measured displacements. The relationship between the measured displacement and the elasticity is not apparent due to complex varying composition of tissue. Most of the biological tissues exhibit viscoelastic, anisotropic and nonlinear behavior in response to applied force [40-41]. Most of the time,

tissue is approximated as a linear elastic solid with isotropic mechanical properties [7], [42-43]. The assumption of linearity is commonly applied typically for strain <10%) in elastography [8].

For a linearly elastic material, the stress and strain distribution throughout a volume can be defined by second-order tensors to determine the tissue mechanical properties. The isotropic linear elastic constitutive Equation [44] is given by

$$\sigma_{xy} = \lambda \varepsilon_{zz} \delta_{xy} + 2\mu \varepsilon_{xy} \tag{1.24}$$

where x, y and z are the Cartesian coordinates and λ and μ are elastic constants, known as Lamé constants and δ_{xy} represents Kronecker delta (For x = y, the value is 1, otherwise it is 0 otherwise). Equation (1.24) is defined at each spatial (*xyz*) location in the tissue.

The loading can be static, quasi-static and dynamic. For a uniaxial static or quasi-static loading, compressive axial stress, σ and axial strain, ε are linearly related through the Young's modulus, *E*, given as,

$$E = \frac{\sigma}{\varepsilon} \tag{1.25}$$

For the dynamic load, elasticity is measured by the wave propagation in the bulk material [45] or on the surface [46] of a sample. For an isotropic linear elastic model of tissue behavior, the propagation of a shear wave in a bulk material is given by the Helmholtz Equation [44]:

$$G\nabla^2 u - \rho \frac{\partial^2 u}{\partial t^2} = 0 \tag{1.26}$$

Where G is the shear modulus, u is displacement, ρ is density and ∇ is the Laplacian operator. The relationship between shear modulus and Young's modulus (E) is:

$$G = \frac{E}{2\,(1+\upsilon)} \tag{1.27}$$

where υ is Poisson's ratio.

For soft tissues, Poisson's ratio is around 0.5, so, Equation (1.27) simplifies to $G = E/3$. The phase velocity of the shear wave, c_s is related to the shear modulus by the expression [45]

$$c_s = \sqrt{\frac{G}{\rho}} \tag{1.28}$$

where ρ for soft tissue is typically assumed to be ~1000 kg/m^3[45].

When a dynamic load is applied at the surface of the sample, the generated surface wave behaves as Rayleigh waves. Rayleigh waves have surface longitudinal and vertical shear components that propagate only few meters per second to penetrate through an elastic medium. For OCE, the surface acoustic phase velocity, c_p, in an elastic, homogeneous half-space is related to the Young's modulus by [46]

$$c_p = \frac{0.87+1.12\nu}{1+\nu}\sqrt{\frac{E}{2\rho(1+\nu)}} \tag{1.29}$$

1.2.4.2 OCE Techniques OCE techniques use a wide variety of loading mechanisms, namely, static/quasi-static or dynamic onto the tissue either internally or externally [12]. Each OCE technique measures the displacement and estimates the tissue mechanical properties through a mechanical deformation model. In this section, compression OCE using quasi-static, external loading; Surface acoustic wave (SAW-OCE) with dynamic loading; and Magnetomotive OCE (MM-OCE) by internal loading will be presented briefly. Key elements of these techniques are shown in Figure 1.8.

Table 1.2 summarizes some performance parameters of OCE techniques.

Table 1.2 Comparison of OCE Techniques

Techniques	Measured parameter	Dynamic range	Axial resolution	Lateral resolution	Loading frequency
Compression	Local strain	~ 660	40 – 120μm [47]	Same as OCT	0 – 800Hz [48]
SAW	Phase velocity	~450	Not known	500- 1000μm	1 – 300Hz [49]
MM	Natural frequency	~16	Same as OCT	Not known	10 – 400Hz [50]

Source: [44]

(i) Compression OCE

In compression OCE, an external compressive load is applied to the sample. Typically, a step change in this load is applied between acquisitions (of either OCT A-scans or B-scans). The local axial strain (i.e., the strain measured over a small depth range), ε_l , is estimated, as illustrated in Figure 1.8(a), by measuring the change in displacement, Δuz , over an axial depth range, Δz [51]:

$$\varepsilon_l = \frac{\Delta u_z}{\Delta z} \tag{1.30}$$

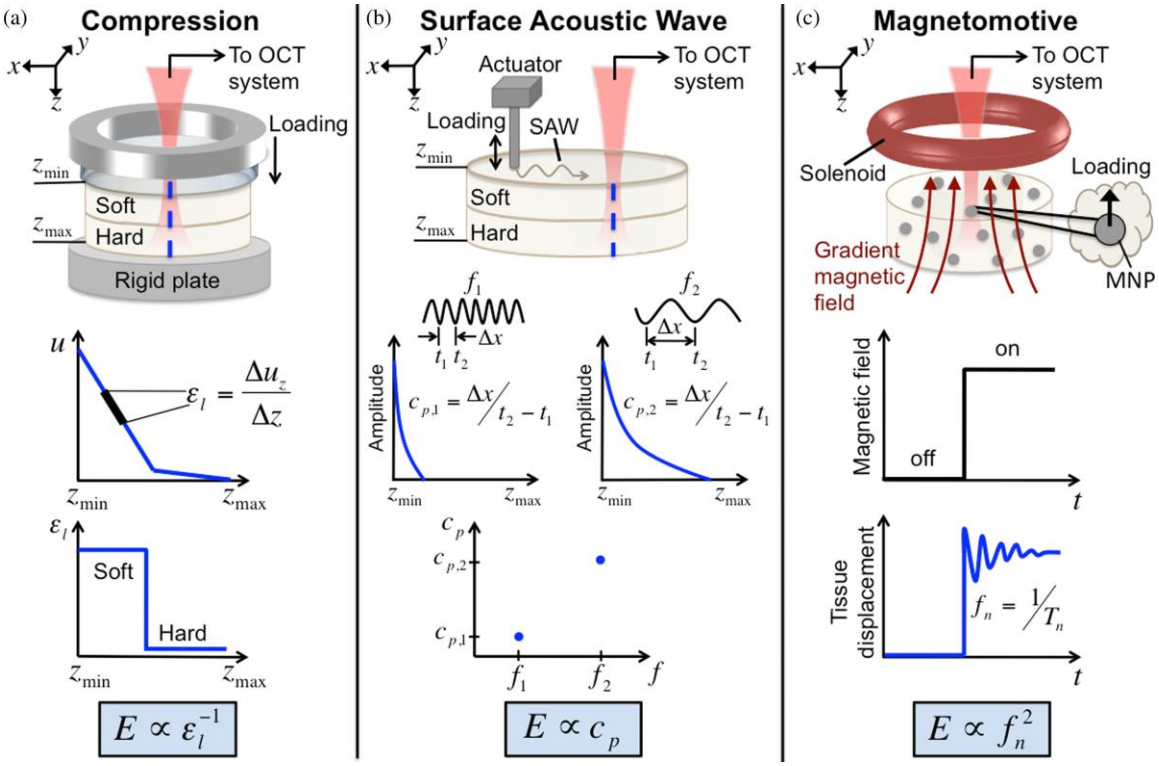

Figure 1.8 Illustrations of loading schemes and elasticity estimation for three OCE techniques: (a) Compression: (top to bottom) loading and detection in a bi-layer sample; displacement versus depth; the corresponding local strain, ε_l ; (b) SAW: (top to bottom) periodic loading and off-axis detection; amplitude decay with depth for high and low SAW frequencies, f_1 and f_2 , respectively; phase velocity, c_p , is frequency-dependent in a layered sample); (c) MM: (top to bottom) MNPs embedded in a homogeneous sample in response to a step application of the magnetic field; applied magnetic field; corresponding sample response versus time, where f_n is the natural frequency of oscillation and T_n the period. *Source: [44].*

The elastogram maps this local strain, which provides a relative measurement of mechanical properties. Compression OCE is one of the effective ways to measure the elasticity ([4], [41-42]). Young's modulus can be calculated from the local strain with known local stress value.

Quasi-static compression loading can be quantified through speckle tracking which has limited motion sensitivity [51 - 54]. On the other hand, phase-sensitive OCT detection methods [55 - 57] has higher motion sensitivity Compression OCE has also used dynamic

loading [48, 58-60]. In dynamic loading, a sinusoidal external load's vibration amplitude is measured and then the dynamic strain is calculated over the variations of vibration amplitude with respect to the axial depth.

(ii) Surface Acoustic Wave OCE (SAW-OCE)

In SAW-OCE, as illustrated in Figure 1.8(b), surface waves are generated by a transient (pulsed) or periodic load and then are detected by OCT after propagating at small velocity (typically at a few m/s) over a lateral distance of typically ~0.5–20mm [61-62]. The relationship between phase velocity of the SAW and the Young's modulus is given in (1.31).

$$c_p = \frac{0.87+1.12\nu}{1+\nu}\sqrt{\frac{E}{2\rho(1+\nu)}} \tag{1.31}$$

Various loading methods have been used to generate SAWs. Contact methods include a metal rod or piezoelectric transducer in direct contact with the sample [63 - 66], as shown in Figure 1.8(b).

The SAW decays exponentially in depth, with an effective penetration depth, z_{SAW}, approximately equal to the wavelength, λ_{SAW}:

$$z_{SAW} \approx \lambda_{SAW} = \frac{c_p}{f_{SAW}} \tag{1.32}$$

where f_{SAW} is the SAW frequency.

The SAW-OCE has the capability to measure tissue mechanical properties at depths beyond the OCT imaging limit. Also; it is suitable for non-contact (air-pressure or photothermal) loading on sophisticated tissues such as the cornea [61-62].

SAW-OCE has lower lateral resolution (~500μm) compared to OCT's lateral resolution (~10μm). This limitation is due to the relatively long wavelength (>10mm) set by the system in order to detect the time delay and dispersion of the surface acoustic waves.

(iii) Magnetomotive OCE (MM-OCE)

MM-OCE uses magnetic nanoparticles (MNPs) scattered in the tissue and stimulated by an external magnetic field to produce local nanometer-range tissue displacements [67 - 71]. MM-OCE uses the time-dependence of the motion to determine the Young's modulus.

Local magnetic gradient force, *F*, per unit volume, *V*, in tissue containing MNPs resulting from the gradient magnetic field, *B*, is given by [44]:

$$\frac{F}{V} = [(M_{MNP} + M_T).\nabla]B \tag{1.33}$$

Where M_{MNP} and M_T are the volume magnetizations due to the MNPs and tissue, respectively.

Net magnetic force is either positive or negative due to the opposite magnetization directions (positive or negative) for the tissue. However, $M_{\mathrm{MNP}} > M_T$ [68]. The magnetic susceptibility of MNPs is $>10^5$ times larger than that of tissue. Therefore, a threshold MNP fractional volume of 10^{-5} [68] is a significant factor for the application of MM-OCE.

A schematic illustration of MM-OCE is shown in Figure 1.8(c). The under-damped oscillation of magnetite MNPs was measured [50] and used to characterize the Young's modulus of silicone phantoms. The natural frequency of the samples is linearly dependent on the square root of E [50]. An MM-OCE has the ability to perform measurements in small samples. Moreover, MM-OCE requires low force to operate and hence, makes it a suitable candidate to measure very soft tissues over other OCE techniques.

1.3 Research Objective

The aim of this doctoral study is to develop of a dual modality OCT system for structural imaging and quantitative optical coherence elastography (qOCE) sensing. This includes:

(i) Development of dual modality qOCE system that tracks both interaction force and local displacement for quantitative mechanical characterization of biological tissue.

(ii) Development of an adaptive Doppler analysis algorithm to accurately track the deformation of tissue under OCE measurement.

(iii) Validation of qOCE technique for linear and non-linear characterization on mechanical substance (phantom) as well as various bio-applications such as *ex vivo* (brain tissue), *in vivo* (skin tissue) sample.

(iv) Validation of depth-resolved displacement for qOCE characterization of stiffness on samples with different thicknesses.

(v) Implementation of a noise adaptive wavelet threshold (NAWT) algorithm to reduce the speckle noises from OCT images.

(vi) Assessment and removal of additive noise in a complex OCT signal based on Doppler analysis.

1.4 Dissertation Organization

Chapter 1 covers the motivation, background information related to our research and the objectives of the present thesis. We have briefly discussed the optical interference theories and light-tissue interaction. A brief introduction of OCT methodology, time-domain OCT (TD-OCT) and Fourier-domain OCT (FD-OCT) are also presented from the view of principle and performance in Chapter 1. Next, the chapter also represents a brief introduction on OCE theories. We will consider the physical principles that govern the tissue deformation. We will use the conventional quantities to relate tissue displacement, deformation, load and elasticity. Also, recent developments of OCE techniques will be covered in this chapter.

Chapter 2 describes the development and validation of qOCE technology based on FD-OCT. Here, we will describe the implementation of our miniature qOCE probe that tracks both the interaction force and depth resolved local displacement within the sample.

The signal processing technique of the qOCE probe will be also presented in the chapter. The chapter focuses on the application of qOCE probe on phantoms and biological tissues (*in vivo* skin tissue and *ex vivo* brain tissue)

Chapter 3 demonstrates the capability of quantitative optical coherence elastography (qOCE) for robust assessment of material stiffness under different boundary conditions using the reaction force and displacement field established in the sample.

Chapter 4 presents the development of a handheld optical instrument that allows *in vivo* real-time OCE characterization based on an adaptive Doppler analysis algorithm to accurately track the motion that varies as time and spatial location. Afterwards, the imaging system and data acquisition will be described for the adaptive Doppler algorithm. We will then show results obtained from phantom experiments and *in vivo* tissue characterization, to demonstrate the effectiveness of the adaptive Doppler analysis for motion tracking in a dynamic manual loading process.

Chapter 5 shows the noise adaptive wavelet thresholding (NAWT) algorithm that removes the speckle noise in OCT and OCE images. Our NAWT algorithm utilizes the characteristics of speckle noise in wavelet domain to adaptively remove speckle noise, while preserves structure features in OCT image. Moreover, NAWT has improved visual appearance of OCT image compared to conventional wavelet domain thresholding and Gaussian filtering.

Chapter 6 represents the development of an innovative algorithm to adaptively eliminate the additive noise from the complex OCT using Doppler variation analysis. The method first generates a map of additive noise for the OCT image through Doppler variation analysis. Then, the additive noise is removed from the real and imaginary parts

of the complex OCT signal through pixelwise Wiener filtering. Results show that this method has the capability to improve the sensitivity of OCT imaging while preserving the spatial resolution without any modification of the imaging apparatus and data acquisition protocol.

Chapter 7 is the concluding chapter. It contains the summary of the work. The chapter also highlights scopes for the future work. All references are placed at the end of this thesis.

CHAPTER 2

DESIGN AND IMPLEMENTATION OF A qOCE FIBER-OPTIC PROBE

2.1 Introduction

This chapter describes the development of a quantitative optical coherence elastography (qOCE) technology. Design and fabrication of a miniature qOCE probe are discussed. qOCE probe has an integrated force sensor and acquires structural OCT data to quantitatively characterize the mechanical properties of tissue. The qOCE system can be used to establish the relationship between mechanical stimulus and tissue response to characterize the stiffness of biological tissue. qOCE data is processed in real-time using graphic processing unit (GPU). The calibration and validation of qOCE in linear and nonlinear mechanical characterization is discussed in this chapter.

2.2 Principle of qOCE Technology

2.2.1 System Configuration and Fabrication of qOCE Probe

Figure 2.1(a) shows the schematic diagram of qOCE system. The qOCE system utilizes a spectral domain OCT (SD-OCT) engine operated at 1.3μm. A superluminescent diode (SLD1325 Thorlabs, 100nm bandwidth) is used as a light source. The system operates at a 91 kHz A-scan rate and has an axial resolution of ~7.5μm. The phase noise of the SD-OCT system is 0.01radians that implies a displacement tracking sensitivity of 1nm. The output of broadband SLD light source illuminates the reference and sample arm of a fiber-optic Michelson interferometer through a fiber-optic coupler (FC). In this system, a fiber optic qOCE probe is used as the sample arm of the Michelson interferometer. The interference

signal from the sample and reference arms is detected by a CMOS InGaAs camera (SUI1024LDH2, Goodrich) after a spectrometer. A frame grabber (PCIe-1433, National Instrument) receives the interferometric signal from the camera and streams the signal to the host computer for further processing. All the device controls and signal processing are performed by a host computer (Dell Precision T7600) with software developed in C + + (Microsoft Visual Studio, 2012) in real-time using graphic processing units (GPU).

A miniature fiber optic probe (qOCE probe) is used to apply compression in the sample. If the sample is mechanically homogeneous, the loading produces a uniaxial compression. Otherwise, the state of stress is determined by the heterogeneity that can also be measured. A common-path OCT signal tracks the probe deformation in response to the applied force. The common-path OCT signal is detected from the interference of the optical fields (E_{fp1}) reflected from the tip of single mode fiber (SMF) and from the first surface of the GRIN (gradient index) lens (E_{fp2}). Another OCT signal is sensed from the interference between the sample light (E_s) and the reference light (E_r) through Michelson interferometry to trace the sample deformation in front of the probe tip.

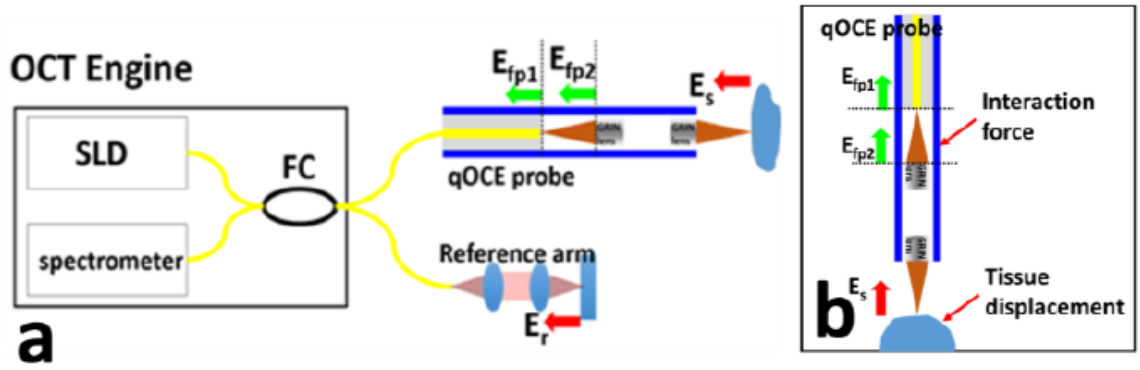

Figure 2.1 (a) Illustration of qOCE system (FC: fiber-optic coupler, SLD: superluminescent diode, E_{fp1}: optical reflection from single mode fiber-tip, E_{fp2}: optical reflection from the proximal end of the first GRIN lens, E_s: sample light, E_r: reference light; (b) qOCE probe for tissue characterization.

Figure 2.2 shows the qOCE probe. The size of the probe is compared with a US quarter. To fabricate the probe, a SMF is inserted into a stainless-steel tube (25-gauge). The fiber and the tube are attached together with the optical epoxy to achieve the preferred firmness for the elasticity measurement. With additional cascaded tubing, the fiber is then combined to a polyimide tube (Microlumen) with inner diameter of 1.8mm. An adhesive optical epoxy is applied to the proximal end of the polyimide tube for fixation. A pair of GRIN lenses (Newport, LGI1300-1A, 0.23 pitch, 0.26mm working distance) is attached to the distal end of the polyimide tube. The distance between the first GRIN lens and the fiber tip is adjusted to obtain the collimated light beam. The second GRIN lens focuses the light beam in such a way that the waist of the output beam is located at 0.26mm depth away from the GRIN lens surface. Particularly, the mechanically active portion in this probe for the OCT sensing is the segmentation between the assembly points of the SMF and the first GRIN lens.

Figure 2.2 qOCE probe compared to a US quarter.

As shown in Figure 2.1(b), a lead-in SMF is connected to the proximal end of the qOCE probe shaft and a pair of rod GRIN lenses are attached to the distal end of the probe shaft. The cleaved SMF tip and the proximal surface of the first GRIN lens work as two end surfaces to form a low fineness Fabry Perot (FP) cavity. Incident light from the SLD

is reflected by two end surfaces (E_{fp1} and E_{fp2}) of the FP cavity due to a discontinuity in refractive index (from glass to air and from air to glass).

The common path interference between E_{fp1} and E_{fp2} generates an OCT signal (A-scan, $\mathbf{I}_{FP}$) with a peak located at the depth L_{fp} that equals the FP cavity length as shown in Figure 2.3(a). The phase of complex valued OCT signal at L_{fp} varies proportionally with the variation length of the FP cavity (as shown in Figure 2.3(b) and (c)) and hence, the force is exerted from the tip of the probe. In other words, the force exerted through the qOCE probe causes deformation of the probe which in turn generates a detectable Doppler phase shift in the complex valued OCT signal. Meanwhile, the GRIN lens pair also serves as an objective lens and focuses the output light beam from SMF for illuminating the sample.

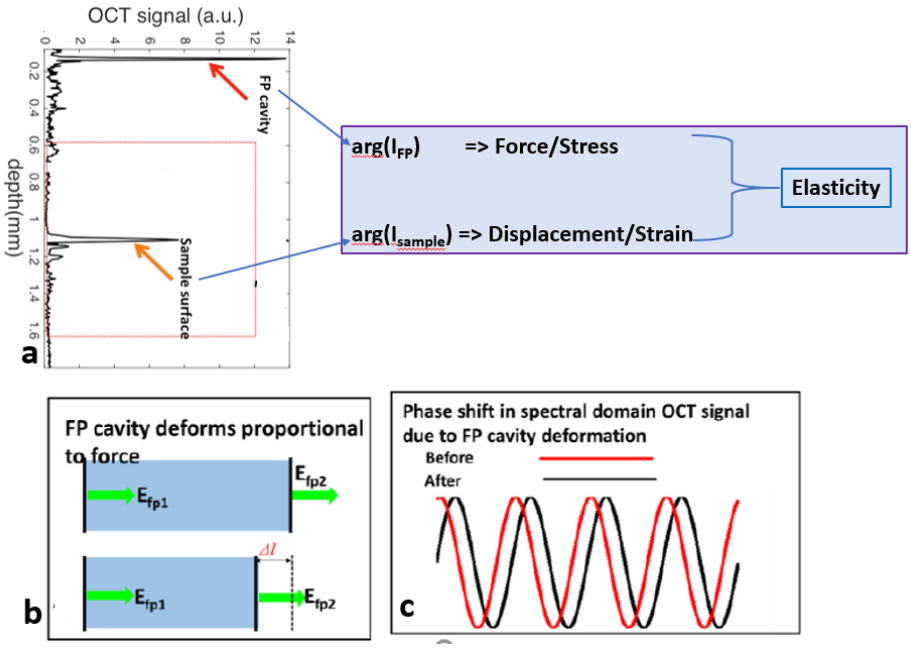

Figure 2.3 (a) Elasticity measurement by qOCE probe; (b) deformation of FP cavity in proportional to the applied force; (c) FP cavity deformation results in phase shift in OCT signal.

The spectrometer detects the backscattered light from the sample (E_s) through the fiber optic probe for OCT imaging. E_s interferes with the reference light (E_r) and generates a depth-resolved profile for the sample ($\boldsymbol{I}_{sample}$). In summary, $\boldsymbol{I}_{\text{sample}}$ is derived from the Michelson interferometer consisting of the reference arm and the sample arm, and $\boldsymbol{I}_{FP}$ is derived from the common path interferometer (the FP cavity). The optical path length (OPL) of reference arm is adjusted in such a way that eventually, OCT signal from the sample ($\boldsymbol{I}_{sample}$) can start beyond L_{fp}. OPL is matched by a SMF patch cord in the reference arm and through the coarse and fine adjustment of the collimator position in the reference arm. This configuration is known as the spatial division multiplexing of the OCT signal. This method is used for simultaneous tracking the probe deformation (ΔL_{probe}) and the sample tissue deformation (ΔL_{sample}).

Particularly, the GRIN lenses pair helps the light beam to focus tightly into the sample and selects a smaller value of L_{fp}. A shorter FP cavity length is necessary to refrain from the insignificant signal roll-off in the system. It is maintained by locating the $\mathbf{I}_{\text{sample}}$ closer to the equal optical path plane.

Now, If L_{GRIN} represents OPL of the light reflected by the distal surface of the second GRIN lens, then the appropriate OPL of the reference arm can be chosen as:

$$L_{ref} < L_{GRIN} + L_{fp} \tag{2.1}$$

The sample is located beyond L_{fp} to avoid the overlapping of signals from the FP cavity. Moreover, the probe deformation for the quantification of the force has low impact on the measurement of tissue deformation as the stiffness of the probe has higher order of magnitude compared to the that of the soft tissue (GPa versus kPa). Therefore, the mechanical property of the tissue can be obtained by measuring the force and the depth-

resolved displacement simultaneously from the space-division-multiplexed OCT signal in the qOCE system.

If the material of the specimen (phantom or tissue) is linearly elastic, a static force generates a uniform displacement. If the material is viscoelastic, a dynamic sinusoidal force can be applied to measure the response. As the mechanical property of the sample is unknown, a simplified linear elastic model with a Young's modulus E is considered in this study.

Using OCT signals obtained, we can quantify the deformation of the probe ΔL_{probe} and the force exerted is given as:

$$F = \alpha \times \Delta L_{probe} \tag{2.2}$$

where α is a constant that correlates the probe tip force (*F*) with the deformation of the probe and can be determined by the calibration experiments. The stress applied to sample can be derived as:

$$\sigma = \frac{F}{A} \tag{2.3}$$

where A is the area of the GRIN lens.

In addition, the strain of the tissue can be calculated as:

$$\epsilon = \frac{\Delta L_{sample}}{L_0} \tag{2.4}$$

Here, L_0 is the initial specimen thickness before compression and ΔL_{sample} represents the sample deformation.

Finally, the sample's Young's modulus (E) which is the linear slope of strain-stress curve can be obtained using Equation (2.5)

$$E = \frac{\sigma}{\epsilon} = \frac{\alpha L_0}{A}\left(\frac{\Delta L_{probe}}{\Delta L_{sample}}\right) \tag{2.5}$$

where tissue elasticity can be quantified by comparing the deformation of probe and the sample.

However, Equation (2.5) is valid based on the following assumptions:

(i) The load is applied slowly. Therefore, force applied to the tissue is equivalent to force measured by the integrated Fabry Perot force sensor.

(ii) The tissue specimen is elastic and viscoelasticity is not considered.

(iii) The materials are incompressible and hence, Poisson's ratio of 0.5 has been considered for the sample.

In this study, the elastic tissue specimen is inserted in between the two rigid compressors one of which is the qOCE probe tip. This configuration provides the most simplified boundary condition and is frequently used indentation method to characterize the biomechanical properties of the soft tissue. For example, indentation measurement on Young's moduli of breast tissues are performed through simultaneous quantification of mechanical loading and tissue deformation [9, 72].

2.2.2 Signal Processing

We analyzed OCT data to track the probe deformation and sample deformation to characterize the mechanical properties quantitatively.

2.2.2.1 Signal Processing to Track the Probe Deformation Figure 2.4(a) shows the block diagram to track the probe deformation. At first, DC subtraction and interpolation on spectral domain OCT data acquired by the CMOS camera is performed to obtain k-(wavenumber) space interferogram. Afterwards, Doppler analysis and peak identification algorithms are applied to track the probe deformation.

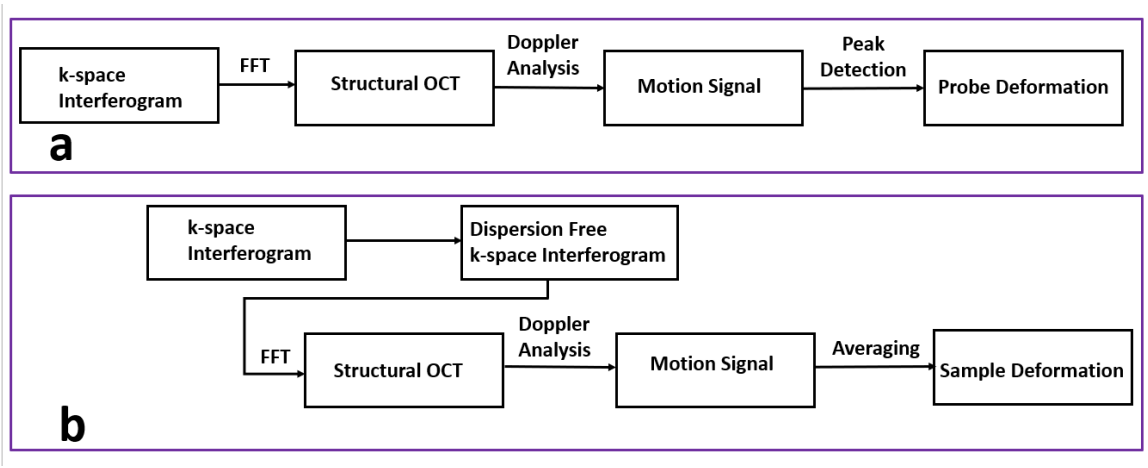

Figure 2.4 Signal processing block diagram for (a) tracking of probe deformation for the quantification of force/stress; (b) tracking of tissue deformation for the quantification of deformation/strain.

To track probe deformation as shown in Figure 2.4(a), the fast Fourier transform (FFT) on k-space interferogram is applied to obtain a complex valued 1D OCT signal, $I_{FP}(z,t)$. Here, z indicates the axial coordinate and t indicates the time of measurement. Next, the signal peak generated by the interference between optical waves from two end surfaces of the FP cavity, ($I_{FP}(L_{probe}, t)$) is identified. Afterwards, Doppler phase shift, ($\delta\phi_{probe}(t)$) between A-scans captured at different time interval, δt_{FP} (here, δt_{FP} = 5ms) is calculated by using Equation (2.6) [73]:

$$\delta\phi_{probe}(t) = a\tan[\, I_{FP}\,(L_{probe}, t + \delta t_{FP}) I^{*}_{FP}\,(L_{probe}, t)] \qquad (2.6)$$

Meanwhile, $\delta\phi_{probe}(t)$ is proportional to the probe deformation and thus the force applied to the sample can be determined.

2.2.2.2 Signal Processing for the Sample Deformation The tracking of sample deformation is obtained from OCT signal of the sample ($I_{sample}(z,t)$) and also through Doppler analysis as shown in Figure 2.4(b). The following steps are applied to determine the sample deformation:

Step-1: Numeric Dispersion Compensation

OCT signal collected from the sample suffers from signal degradation due to the effect of the chromatic dispersion. Therefore, the amount of dispersion mismatch needs to be measured in order to obtain a high resolution and a high SNR OCT signal ($I_{sample}(z,t)$) from the sample. To quantify the mismatched dispersion, the non-linear phase of the interferometric spectrum is extracted through Hilbert transformation on the interferometric spectrum. Afterwards, the non-linear phase component of the signal is approximated by applying the third order polynomial fitting: $\Phi(k) = p_3k^3 + p_2k^2 + p_1k + p_0$ where p_o to p_3 are the coefficients. Finally, the non-linear phase is then subtracted in the GPU based software before preforming FFT for real-time dispersion compensation.

Step-2: Doppler analysis

Biological tissue is less rigid compared to the plastic probe shaft and deforms more. Therefore, two A-scans acquired with smaller time interval (δt_s = 0.2ms) is applied for Doppler phase calculation (Equation (2.7)). Otherwise, deformation obtained through Doppler analysis may suffer from the phase wrapping artifact.

$$\boldsymbol{\delta}\phi_{sample}(z,t) = \operatorname{atan}\left[I_{sample}(z,t) + \delta t_{sample}\right) I^{*}_{sample}(z,t)] \tag{2.7}$$

Step-3: Averaging

Both structural OCT signal from highly scattering sample and Doppler OCT signal exhibit speckle noise. As a result, to track sample deformation with higher accuracy, spatial average is performed to obtain the filtered phase shift ($\delta\phi_{sample,filtered}(t)$) for better result (Equation (2.8)). $\delta\phi_{sample,filtered}(t)$ is proportional to spatially resolved displacement of the sample that can be converted to the local deformation and strain.

$$\delta\phi_{sample,filtered}(t) = \int_{L_0-\frac{\delta L}{2}}^{L_0+\frac{\delta L}{2}} \boldsymbol{\delta}\phi_{sample}(z,t)\, dz \tag{2.8}$$

with $\delta\phi_{probe}(t)$ or $\delta\phi_{sample,filtered}(t)$ obtained, probe deformation (δL_{probe}) and sample deformation (δL_{sample}) can be determined using Equation (2.9). For probe deformation tracking, the central wavelength of SLD output in air ($\lambda_0 = 1.3\mu m$) is selected in Equation (2.9). For sample deformation tracking, the wavelength correction is achieved by the refractive index ($\lambda = \lambda_0/n$).

$$\delta L_{probe,sample}(t) = \frac{\delta\phi_{probe,sample}(t)}{4\pi}\lambda \tag{2.9}$$

Notably, in compression OCE, mechanical loading is applied to tissue in a quasi-static process and it is essential to quantify the deformation over the entire compression process. Therefore, both the probe deformation and the sample deformation are integrated over the same time interval, as shown in Equation (2.10). The time integration also improves SNR for the elasticity measurement.

$$\Delta L_{probe,sample}(t) = \int_{t_{start}}^{t} \delta L_{probe,sample}(\tau)\, d\tau \tag{2.10}$$

with probe and sample deformation acquired using Equation (2.9) and (2.10), tissue elasticity can be measured using Equation (2.5). In the real-time software, a variable is continuously updated to calculate the accumulated displacement as shown in Equation (2.11):

$$\Delta L_{probe,sample} = \Delta L_{probe,sample} + dL_{probe,sample} \tag{2.11}$$

where $dL_{probe,sample}$ represents the incremental displacement.

2.3 Validation and Performance of qOCE Probe

2.3.1 A-scan Signals from qOCE Probe

Typical A-scan signals are acquired from the qOCE probe as shown in Figure 2.5. Figure 2.5(a) shows OCT signals attained from the probe without (black) and with (blue) numeric

dispersion compensation. A silicone phantom with Titanium dioxide to provide scattering was used as sample. Both A-scans multiplex the signals from the common path interferometer and the Michelson interferometer. For the A-scan obtained without dispersion compensation (black), a sharp signal peak (red arrow) is observed. This peak corresponds to the common path OCT signal derived from the FP cavity (interference between optical fields E_{fp1} and E_{fp2} in Figure 2.1(b). As E_{fp1} and E_{fp2} share the same optical path, the interferometric signal is free from the dispersion mismatch and a sharp peak is detected without any dispersion compensation. Moreover, the detected A-scan signal broadens at a larger imaging depth, as indicated by the dashed rectangle. Signal bounded by the rectangle is generated from the interference between the reference mirror (E_r) and the distal surfaces of the second GRIN lens (E_{GRIN}), as well as sample (E_s) under imaging. As the reference light and sample light in the Michelson interferometer travel through the different media (fiber and air), the detectable signal experiences a considerable amount of signal degradation due to the dispersion mismatch.

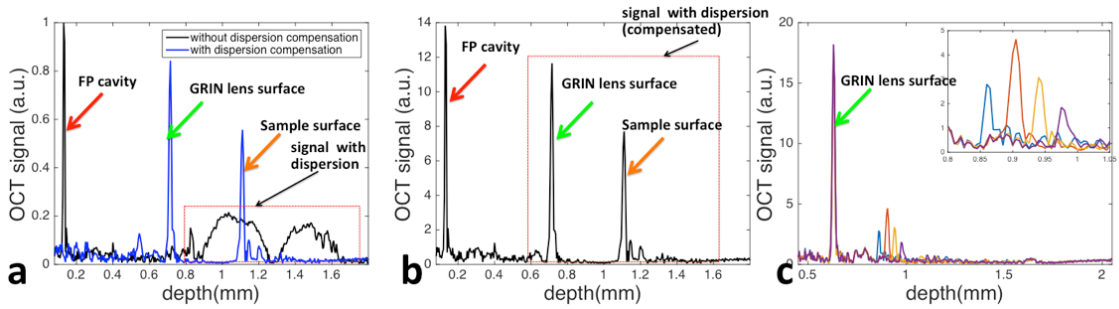

Figure 2.5 (a) Typical A-scan from qOCE probe without (black) and with (blue) dispersion compensation; (b) multiplexed signals at three different surfaces for simultaneous tracking of the probe and the tissue deformation; (c) OCT signal from Michelson interferometer after the dispersion compensation.

In comparison, the blue curve shown in Figure 2.5(a) which is obtained after the dispersion compensation shows a sharp peak corresponding to the distal surface of the

GRIN lens (indicated by the green arrow), a sharp peak corresponding to the sample surface (indicated by the orange arrow) and depth-resolved sample profile. However, OCT signal due to interference between E_{fp1} and E_{fp2} diminishes in the blue curve because of additional non-linear phase induced to the dispersion-free signal in the process of numerical dispersion compensation. Figure 2.5(a) clearly shows that OCT signal from the FP cavity for force/stress measurement is spatially demultiplexed with OCT signal from the tissue for displacement/strain measurement. Multiplexed CP OCT signal attained from the FP cavity without dispersion compensation and Michelson OCT signal acquired from tissue with dispersion compensation are also shown in Figure 2.5(b). By tracking phase shift between complex valued, spatial division multiplexed OCT signal as shown in Figure 2.5(b), the deformations of the probe and the tissue can be quantified.

Figure 2.5(c) shows segments of OCT signal obtained from the Michelson interferometer after dispersion compensation with visible low intensities weak scattering sample phantom. Curves with different color are obtained when the sample is located at various depths. Signal peak from the GRIN lens surface (indicated by the green arrow) remains identical shape for different signals. Particularly, focusing effect has been detected in Figure 2.5(c) where the focal plane is approximately 0.26mm away from the GRIN lens surface.

2.3.2 Tracking of Probe and Tissue Deformation from the qOCE Probe

Temporal variation of A-scan in Doppler phase shift is used to track the probe and the tissue deformation as shown in Figure 2.6. Figure 2.6(a) shows a frame of sequentially acquired spectral interferograms. In Figure 2.6(a), different coordinate in horizontal direction corresponds to different wavelength/wavenumber and different coordinate in

vertical corresponds to different time. Fringes due to the interference between optical fields from the two end surfaces of the FP cavity are visible in Figure 2.6(a). As the probe is used to compress tissue during the acquisition of Figure 2.6(a), slight fringe shift over time can be observed due to the probe shaft deformation. Using our real-time GPU software, we quantified the phase shift shown in Figure 2.6(a) by Equation (2.6) and converted the phase shift to probe deformation using Equations (2.8) and (2.9). Figure 2.6(b) shows signal from the tissue (screen capture of real-time display) when the qOCE probe is used to compress the phantom. Our software showed structural OCT signal (upper), as well as Doppler OCT signal (ODT, lower) obtained by calculating A-scan signal phase shift. Sequentially acquired signals are displayed in Figure 2.6(b) where different coordinate in horizontal direction corresponds to different time and different coordinate in vertical direction corresponds to different depth. Similarly, Figure 2.6(c) shows the screen capture of real-time display when releasing the compression exerted to the same phantom through the probe. Notably, in our software, colored-coded Doppler signal has been used to improve the visualization in the direction of the motion or phase shift. The negative phase shift has been coded with red color and the positive phase shift has been coded with blue color. Due to small time window (0.1s) frame for the acquisition of A-scans during quasi-static compression shown in Figure 2.6(b) and 2.6(c), a small phantom deformation is found and cannot be detected in structural OCT images (upper insets of Figure 2.6(a) and 2.6(b)). However, the phase of OCT signal provides much higher sensitivity in deformation tracking. Deformation of phantom in different direction due to the compression and removal of compression are clearly visible in the lower panels of Figure 2.6(b) and 2.6(c).

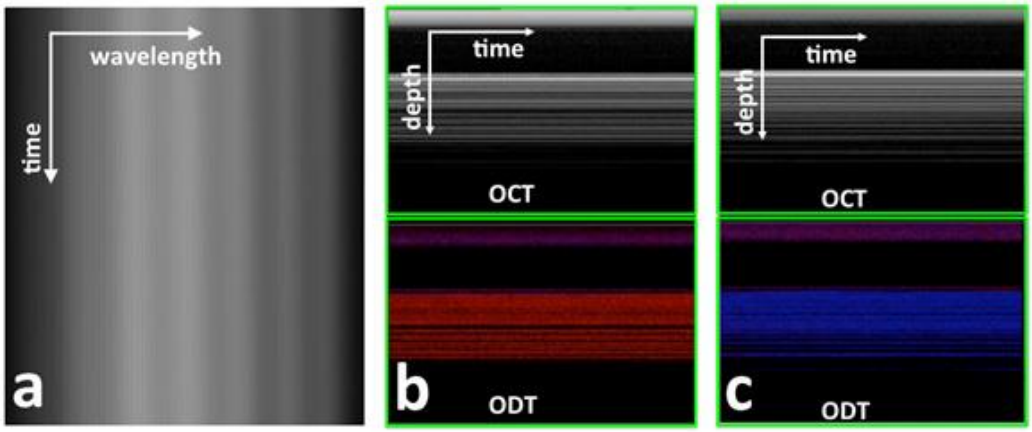

Figure 2.6 (a) A frame of interferometric spectrum when force is applied to the probe; (b) structural OCT image (upper) and Doppler OCT image (lower) during compression of sample by qOCE probe; (b) structural OCT (upper) and Doppler OCT images (lower) when the compression is released.

2.3.3 Calibration of the qOCE Probe

Accurate characterization of elastic property of tissue depends on the proper measurement of the external applied force/stress and the tissue's response in the form of deformation/strain. First, the accuracy of deformation/displacement tracking is calibrated experimentally. The qOCE probe is attached to a precise linear motor (Newport, ILS100CC DC). The probe is translated by the motor in the axial direction without touching the rigid scattering sample. Therefore, the displacement between the probe and the sample is equivalent to the distance translated by the motor. Using OCT signal, displacement between qOCE probe and sample is determined by using Equations (2.7) – (2.10), in the real-time GPU software. Comparison of displacement extracted through Doppler analysis of OCT signal with the known motor displacement is as shown in Figure 2.7. Clearly, displacement calculated using Doppler analysis shows a linear dependency on actual displacement.

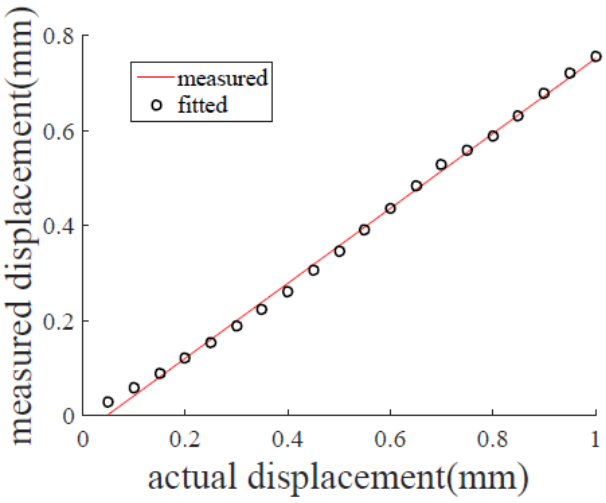

Figure 2.7 Calibration between Doppler OCT signal displacement and actual displacement.

The model is validated by linear regression given by Equation (2.12):

$$\mathbf{D}_{physical} = a\,\mathbf{D}_{Doppler} + b \tag{2.12}$$

Where the parameters are a = 1.2 and b = 0.004mm. R^2 statistic of the fitting is 0.9977, which indicates a high linear relationship between the calculated displacement and the actual displacement. The coefficient a accounts for the direction of light propagation and the refractive index of the phantom.

Moreover, another calibration experiment is conducted for the validation of the force/stress sensing capability of the qOCE system. The qOCE probe is mounted on a linear stage and the stage is translated horizontally to exert the force to the sensing tip of a digital force gauge (Shimpo, FG-3005) The digital force gauge has a high precision force measurement with 0.005N resolution. The probe deformation is tracked using Doppler OCT signal obtained from the integrated FP cavity. The results are then compared as shown in Figure 2.8.

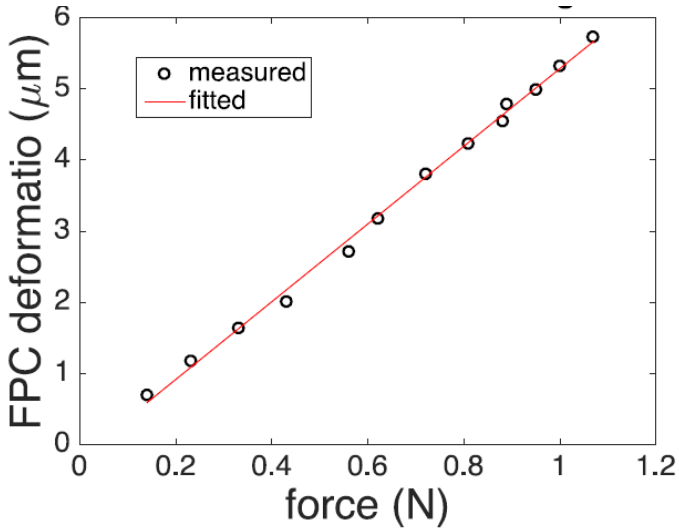

Figure 2.8 Calibration between force due to the FP cavity deformation and the force applied.

Notably, the length of FP cavity is varied linearly with the force. The linear regression model is given by Equation (2.13)

$$\mathbf{D}_{FPC} = \alpha\mathbf{F} + \beta \tag{2.13}$$

Here, the results indicated $\alpha = 0.1795$N/μm. R^2 statistic of the fitting is 0.9971, indicating a highly linear relationship between the force and the probe deformation.

Figures 2.7 and 2.8 demonstrate the quantification of the force and displacement using OCT signal. Based on results obtained from the calibration experiments, phase shift extracted from OCT signal can be converted to the tissue deformation and the force. Finally, stress can be calculated using the area of the GRIN lens (~2.54 mm^2) in contact with sample for the compression.

2.4 Elasticity Measurement and Mechanical Characterization of Samples

Conventional compression OCE lacks the mechanism for the quantification of the interaction force which limits its application for the tissue characterization. This is because, it is impossible to compare tissue stiffness in different measurement sessions when the force in unknown. In addition, most of the biological tissues show different elastic performance when large loads are being applied as compared to small loads. At larger load, strain stiffening commonly occurs in biological tissue and the linear stress-strain relationship becomes restricted to few tissues such as bone tissue in a very limited deformation region. Therefore, the tissue displacement measured by OCE not only depends on the mechanical tissue characteristics, but also depends on the magnitude of loading applied to the tissue sample [13]. Therefore, OCE measurement considering the nonlinear elasticity of tissue is important to achieve the effective tissue differentiation, which has not been investigated widely before [14].

In the previous section, the development of qOCE instrument has been presented. The qOCE instrument simultaneously measures the force exerted to tissue and the resultant tissue deformation [74]. In this section, the significance of force quantification in OCE would be explored for the characterization of linear and nonlinear elasticity. In order to measure the apparent stress and the apparent strain of the tissue using qOCE, some assumptions are used: qOCE probe is moved slowly to apply the compressive load to the tissue so that sample tissues can be assumed as isotropic, homogeneous, elastic and incompressible within the volume interrogated by qOCE. Mechanical contrast between different biological tissues can be revealed using a calibrated qOCE instrument.

A miniature fiber optic qOCE probe integrated with a Fabry-Perot (FP) interferometer is used to indent the tissue sample and to collect optical signal for elasticity assessment. In acquiring experimental data, we simultaneously measured the apparent stress and strain for the elastic characterization of biological tissue. These quantities are referred as apparent stress and strain in this section, because our measurement assumed a uniform spatial distribution of the stress and the strain within the tissue, which may not be true in biological samples with structural and mechanical heterogeneity. The qOCE probe is used to perform slow indentation on the sample and OCT signals are acquired. We quantified the probe-tissue interaction force (F) using Φ_{FP}, the accumulated phase shift at the signal peak for $\boldsymbol{I}_{FP}$, because Φ_{FP} is proportional to probe shaft deformation and thus the force. Briefly, the Doppler phase shift $\varphi_{FP}(\tau)$ are calculated between A-scans and integrated the Doppler phase shift over time:

$$\phi_{FP}(t) = \int_0^t \phi_{FP}(\tau)\, d\tau \tag{2.14}$$

To quantify the force, a calibration experiment is performed to extract the constant (α) that correlated the probe tip force (F) with the phase shift (Φ_{FP}) due to FP cavity displacement: $F = \alpha\Phi_{FP}$. The apparent stress was then obtained: $\sigma = F/A$. Here A indicates the area of the GRIN lens at the tip of the qOCE probe and A = 2.5mm^2, calculated using the radius of the GRIN lens. On the other hand, we used $\boldsymbol{I}_{tissue}$ to quantify tissue displacement and the apparent strain. We calculated tissue displacement (δl) using Doppler phase shift at depth d_0:

$$\delta l = \frac{\delta\phi_{tissue}(d_0,\tau)\lambda_0}{4\pi} \tag{2.15}$$

and integrated tissue displacement over time:

$$\Delta d = \int_0^t \delta l\,(d_0,\tau)\; d\tau \tag{2.16}$$

Assuming the uniform distribution of the displacement, the apparent strain can be calculated as: $\varepsilon = \Delta d/(\Delta d + d_0)$. In this study, d_0 is chosen as 0.63mm where the tissue deformed substantially and the SNR of OCT signal is satisfactory. Notably, the apparent stress (σ) and the corresponding apparent strain (ε) are both obtained by integrating the Doppler phase from the beginning of indentation ($\tau = 0$) to the observation time point t ($\tau = t$). The fundamental data acquisition frequency for stress and strain signal was 10kHz, determined by an external trigger source.

To perform elastic characterization, we attached the qOCE probe to a high precision linear motor (Newport, ILS100CC DC) and translated the qOCE probe at small speed (~0.1 mm/s) in axial direction for indentation. This relative slow motion is introduced to minimize any viscoelastic effects. The apparent stress-strain data are obtained during the indentation process for linear and nonlinear characterization of elastic properties of the material.

To demonstrate qOCE's capability in linear and nonlinear mechanical characterization, we performed qOCE measurement on following samples:

(a) An in-house fabricated elastic phantom

(b) *In vivo* qOCE experiment on human skin tissue

(c) *Ex vivo* qOCE experiment on rat brain tissue

2.4.1 Elasticity Measurement of Mechanical Substance

Phantoms are used to evaluate the qOCE technique. At first, we performed the qOCE experiment on an in-house fabricated elastic phantom. The phantoms mimic the optical

property and elastic modulus of biological tissues. The phantom material is silicone rubber called RTV-22 purchased from Raw Material Suppliers. PDMS phantoms are fabricated with different stiffness by combining PDMS fluid with curing agent added at different volumetric ratios. In addition, titanium dioxide is poured into the samples to provide the light scattering [75]. The mixture is then thoroughly mixed, degassed for 15 minutes, and then is cured on a 6-inch square glass plate. PDMS samples are used for the experiment and specimens are cut using circular dies with a 0.5-inch diameter.

Different loading condition is applied to observe the linear and nonlinear properties of the sample. Figure 2.9 shows the stress-strain relationship for different loading conditions. Figure 2.9.2(a) shows the linear apparent stress-strain curve for small apparent strain. The curve shows nonlinear characteristic after the apparent strain reaches high strain as shown in Figure 2.9(b). For linear regime of the apparent stress-strain curve (ε<0.1), Young's modulus (E) of the material is: $\boldsymbol{\sigma} = E_{\text{linear}}\boldsymbol{\varepsilon}$, where $\boldsymbol{\sigma}$ indicates the apparent stress, $\boldsymbol{\varepsilon}$ indicates the apparent strain and E_{linear} indicates the Young's modulus for the linear region of the sample. After performing the regression analysis, E_{linear}: E_{linear} = 84.85kPa with R^2 statistics of 0.9971.

For non-linear apparent stress-strain curve as shown in Figure 2.9(b), E of tissue can be extracted by the simplest form of Neo-Hookean model, given as:

$$\sigma = E_{nonlinear}\left(\frac{\lambda-1}{3\lambda^2}\right) \tag{2.17}$$

Here λ indicates the magnitude of stretch and λ = 1-ε.

The Neo-Hookean model reduces to the linear elasticity [76 - 77]. Afterwards, regression analysis is carried out to extract $E_{\text{nonlinear}}$, using the nonlinear model. $E_{\text{nonlinear}}$ is 85.64kPa. This value is highly consistent with E_{linear}. The R^2 statistics of the regression

analysis is 0.9787. The fitting results are shown as the black curve in Figure 2.9(b). For comparison, both the linear and nonlinear curves are plotted in Figure 2.9(b). Notably, the experimental data is significantly different from the predicted linear model for the strain value larger than 0.2.

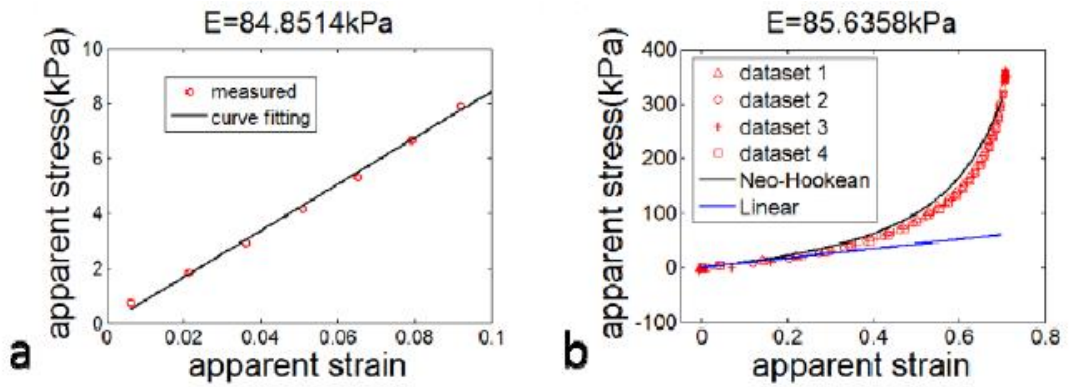

Figure 2.9 (a) Linear stress-strain curve at small strain; (b) nonlinear stress-strain curves and curve fitting based on Neo-Hookean model.
Source: [93]

2.4.2 Elasticity Measurement of *in vivo* Biological Tissue

An *in vivo* qOCE measurement is performed upon human skin tissue. This validates that the qOCE technology can estimate the nonlinear elasticity of biological tissue. The volar and the dorsal skin of the forearm of a 32 years old healthy volunteer is used as sample. The arm is rested on a flat rigid surface to minimize the motion artifacts during the measurement. Next, Quasi-static indentation is applied to the forearm regions. B-scan and *enface* images of volar and dorsal regions are shown in Figure 2.10(a)- (d), respectively. Uniform distribution of tissue strain is assumed during the experimental procedure for the analysis of dermis deformation and for the measurement of the dermis stiffness. During the experiment, it is also assumed that equilibrium has been achieved at arbitrary time during the indentation process and the apparent stress is detected by the probe tip and the force is

calculated. Figure 2.10(e) shows the apparent stress-strain curves (black dashed curve: volar forearm skin; red dashed curve: dorsal forearm skin) obtained during the experiment. Both curves are nonlinear. The slope of the skin stress-strain curve increases with the magnitude of mechanical loading. This is because, during the compression process the dermis collagen fibers rearrange their orientations and shows large stiffness [78]. As shown in Figure 2.10(e), dorsal forearm skin has larger slope compared to volar skin over the entire range of loading. These results are consistent with the experimental data of previous OCE experiment [65].

When the apparent strain is small ($\varepsilon < 0.1$), E values in the linear elasticity regime for volar region is E_{volar} = 79.7kPa and dorsal skin region is E_{dorsal} = 116.7kPa. Different tissues have different E values for the qOCE system and measurement geometry. This validated the qOCE system's tissue differentiation capability. In comparison with the structural OCT images obtained in Figure 2.10(a) –(d), it is clear that structural OCT images do not show significant difference between volar and dorsal skins of the forearm. It suggests that qOCE can potentially provide a new dimension of information for the tissue characterization.

Furthermore, linear regression analysis is performed for the apparent stress-strain data to demonstrate the nonlinear elastic behavior of the skin tissue. The resultant values of R^2 statistics of the regression are 0.7616 and 0.8898, for the volar skin and the dorsal skin, respectively which implies that a linear model cannot provide the satisfactory performance to describe the apparent stress-strain relationship of Figure 2.10(e).

Alternatively, we modeled the acquired apparent stress and apparent strain values to a nonlinear elastic model for skin tissue, known as Veronda-Westman Constitutive Law:

$$\sigma = 2\mu_0\left(\lambda^2 - \frac{1}{\lambda}\right)\frac{\exp\left[\gamma\left(\lambda^2+\frac{2}{\lambda}-3\right)\right]-1}{2\lambda} \tag{2.18}$$

where σ indicates the stress and λ indicates the stretch [79, 80].

This model is originally developed for skin tissue and is successfully used to fit experimental data. In this model, μ_0 is directly related to linear elasticity $E = 3\mu_0$ and γ determines the nonlinear rate of the apparent stress-strain from the linear behavior. The fitting results are shown as solid curves in Figure 2.10(e).

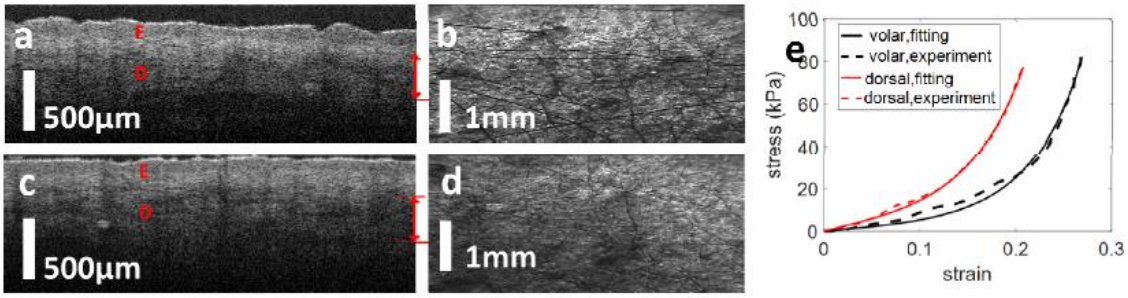

Figure 2.10 Volar forearm of human skin: (a) cross-sectional and (b) *enface* images; dorsal forearm: (c) cross-sectional and (d) *enface* images; (e) stress-strain curve for volar (black) and dorsal (red) regions. E indicates epidermis and D indicates dermis.
Source: [93]

For this experiment, μ_0 is 14kPa for volar skin and 38kPa for dorsal skin. $\gamma \approx 5.3$ for both dorsal and volar skin. $E = 3\mu_0$ is satisfied for dorsal skin. However, this equation is not validated for volar skin. This is because, we had very limited data for the linear elasticity regime to estimate E.

2.4.3 Elasticity Measurement of *ex vivo* Biological Tissue

Next, the elasticity is measured by OCE to *in vivo* rat brain tissues. 10-week-old Sprague Dawley rats (320-360g in weight) from Charles River Labs are used as samples. The brain from a rat, sacrificed for other research purposes, is harvested. A coronal brain slicer is

used to cut the brain into slices with 3mm thickness. The miniature qOCE probe performed localized mechanical characterization on hippocampus and other anatomical regions (Figure 2.11(a)). The quasi-static indentation is provided using the qOCE probe on the brain slice. Hippocampus (Figure 2.11(b)) and cortex grey matter (Figure 2.11(c)) are interrogated. In Figure 2.11(b) and 2.11(c), the scale bars indicate 1mm. Hippocampus of the brain is the center for memory, emotion and spatial navigation. Hippocampal damage in traumatic brain injury (TBI) causes disability. The mechanical contrast between hippocampus and other parts of the brain directly relates the damage of hippocampus in TBI [81, 82]. Therefore, the mechanical properties of the hippocampus are important. In this experiment, qOCE probe is moved for 0.6mm to apply pre-compression.

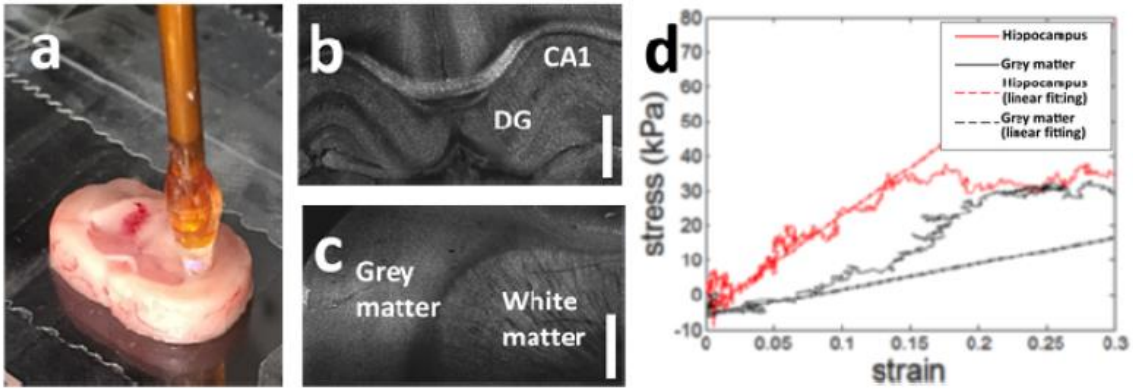

Figure 2.11 (a) qOCE probe and brain slice; (b) *enface* OCT image of hippocampus from the coronal plane (DG: dentate gyrus; CA1: Cornu Ammonis 1); (c) *enface* OCT image of cortex from the coronal plane; (d) stress-strain curve for cortex grey matter (black) and hippocampus (red) of rat brain. Solid curves represent experimental data and dashed curves are linear fitting of the stress-strain curve.
Source: [93]

The apparent stress-strain curves from the hippocampus (red) and the cortex (black) are shown in Figure 2.11(d) as solid curves. At small apparent strain (strain<0.1), the brain tissue had linear elasticity. Young's moduli for hippocampus (E_H) and cortex (E_C) are: E_H = 276kPa and E_C = 74kPa. These values are consistent with results of previous

experimental findings. The result suggests that the hippocampus tissue has larger stiffness compared to the cortex [84]. Figure 2.11(d) shows the linear curve fitting of stress-strain as dashed curves. The difference between solid and dashed curves in Figure 2.11(d) suggests the nonlinear stress-strain relationship for brain tissues.

We could not apply stress to the tissue for strain value larger than 0.2 due to the material failure. This is consistent with published results [75]. A linear regression model is applied to fit the apparent stress-strain data corresponding to strain ranging from 0 to 0.2. The R^2 statistics are 0.9472 and 0.8094 for the hippocampus, and the grey matter, respectively. The result suggests that the elastic behavior of hippocampus is almost linear whereas the grey matter diverges from linear elastic characteristic at a smaller strain.

2.5 Conclusion and Discussion

In this chapter, the principle of a fiber-optic qOCE device has been described. The qOCE device simultaneously quantifies the force exerted on the tissue and measure the resultant tissue deformation. The qOCE technique allows direct measurement of elastic properties and therefore has great potential in many applications, such as cancer diagnosis, brain injury study, tissue engineering and biomechanical modeling.

Currently, Young's modulus obtained from atomic force microscopy studies the tissue mechanics at the micro- through nanoscopic scale or be obtained from tensile stretching or indentation measurement that studies tissue mechanics at the macroscopic scale [83]. However, these techniques rely on *ex vivo* tissue specimens that have different mechanical properties from tissue in living organism. Therefore, the qOCE instrument with

small dimension allows *in situ* measurement of Young's modulus and is highly significant for the study of tissue mechanics.

Biological tissues often exhibit nonlinear elastic behavior. Therefore, understanding the nonlinear elasticity is critical for elastography imaging and mechanical characterization of biological tissue. However, conventional OCE techniques lack the mechanism for force sensing. As a result, the nonlinearity of tissue elasticity has not been fully investigated and it remains challenging to establish the consistency in tissue stiffness obtained from different OCE measurements. In this study, we demonstrated the capability of qOCE in characterizing the both the linear and nonlinear elasticity of biological tissue. We validated the effectiveness of our qOCE system by correlating its measurements with published values.

CHAPTER 3

qOCE FOR ROBUST STIFFNESS ASSESSMENT

3.1 Introduction

In this chapter, we describe the capability of quantitative optical coherence elastography (qOCE) for robust assessment of material stiffness under different boundary conditions using the reaction force and displacement field established in the sample.

Breast conserving surgery is one of the most frequently practiced surgical procedures for the treatment of breast cancer. In breast conserving surgery, a negative surgical margin reduces the risk of local recurrence and reduces the need for repeated surgery. The capability to assess surgical margin intraoperatively can benefit both patients and clinicians [85]. Cancerous breast tissue usually has higher stiffness compared to normal breast tissue [9]. Therefore, manual palpation is frequently used in clinical examination of breast cancer. Elastography techniques based on cross-sectional imaging modalities, such as ultrasound imaging and magnetic resonance imaging (MRI), are also used for breast imaging [86, 87]. Optical coherence tomography (OCT), a microscopic tomographic imaging modality based on low coherence light interferometry, has found applications in breast cancer management [16, 88 - 90]. A functional extension of OCT, optical coherence elastography (OCE) provides mechanical contrast and can be used to differentiate cancerous breast tissue and normal breast tissue [38, 44, 91]. Compared to other elastography technologies, OCE has much higher spatial resolution and allows mechanical characterization on a small volume of breast tissue.

An OCE instrument can be fabricated using fiber-optic components. The OCE instrument can be also integrated into a handheld probe that is compact and lightweight [92]. Therefore, an OCE instrument will allow convenient assessment of tissue malignancy for margin assessment during breast conserving surgery. Moreover, OCE instrument is capable of improving patient outcome by confirming the negative margin. However, conventional OCE performs the qualitative measurement and only tracks the deformation of the sample. Hence, the reaction force is unknown. Therefore, results from different OCE measurement sessions fluctuate significantly for the same sample and it also becomes challenging to establish consistent standards for the tissue classification.

In our laboratory, we have developed and validated a unique fiber-optic quantitative OCE (qOCE) technology [74, 93]. For mechanical characterization, the qOCE probe is translated to compress the sample. During the indentation period, OCT signal is captured from the qOCE probe and is analyzed for simultaneous quantification of reaction force (F) and depth resolved sample displacement (d(z)). Nevertheless, quantitative extraction of material properties remains challenging because the results of qOCE characterization (reaction force and displacement field established within the sample) depend on material properties and the geometric boundary condition [94, 95]. In this section, we describe a method for robust stiffness assessment by qOCE data (F and d(z)). We have also validated the method with the experimental data.

3.2 Experimental Set-up and Sample Preparation

Details about the qOCE technology have been described in Chapter 2. A spectral domain OCT (SD-OCT) engine at 1310nm based on a fiber-optic Michelson interferometer is used in this experiment. The experimental setup is shown in Figure 2.1 of Chapter 2. The imaging system has a 2.5mm imaging depth. The sample arm of the interferometer is interfaced with the novel qOCE probe that has a built-in Fabry–Perot (FP) force sensor and also acquires a signal from the sample underneath the probe. A common path OCT signal is generated due to the interference between optical fields reflected from two end surfaces of the FP cavity. Consider, length of FP cavity is denoted as L_{FP}. The signal peak (I_{FP}) from the FP cavity is localized at L_{FP}. When a force (F) is exerted through the probe, the FP cavity length changes in proportional to the F which is given as: $F = L\ \Delta L_{FP}$ where ΔL_{FP} is amount of length change in FP cavity, k is a parameter that is related to the stiffness of the probe shaft. So, Doppler phase shift of I_{FP} is:

$$\Delta\phi_{FP} = \int_{t_{start}}^{t_{end}} a\tan[I_{FP}(t + \delta t)I_{FP}^{*}(t)]dt \tag{3.1}$$

where t_{start} and t_{end} indicate the start and end time of the indentation process and δt indicates the time interval between signals involved in Doppler analysis.

With $\Delta\phi_{FP}$, ΔL_{FP} can be computed as:

$$\Delta L_{FP} = \frac{\lambda_0 \Delta\phi_{FP}}{4\pi} \tag{3.2}$$

Where λ_0 is the central wavelength of the light source.

The applied force is given as:

$$F = \frac{k\,\lambda_0}{4\pi}\,\Delta\phi_{FP} = \alpha\,\Delta\phi_{FP} \tag{3.3}$$

Light exiting from the probe also illuminates the sample. Backscattered light from the sample ($\mathbf{E}_s$) couples back into the qOCE probe and then interferes with reference light

($\mathbf{E}_r$) to form a depth resolved OCT signal ($I_s(z)$). Next, Doppler analysis is applied to $I_s(z)$ and the Doppler phase is estimated according to Equation (3.4):

$$\Delta\phi_s(z,t) = \text{atan}[I_s(z,t+\delta t)I_s^*(z,t)] \tag{3.4}$$

Therefore, Depth resolved displacement from the sample is calculated as:

$$d(z) = \frac{\lambda_0}{4\pi}\int_{t_{start}}^{t_{end}} \Delta\phi_s(z,t)\,dt \tag{3.5}$$

Meanwhile, the OCT signals obtained for the tracking of probe deformation (I_{FP}) and the tracking of tissue deformation $I_s(z)$ can be multiplexed simultaneously in the same A-scan without any spatial overlap by choosing the appropriate reference arm optical path length.

The qOCE probe is translated to compress the sample and OCT signals are acquired during the compression process. These OCT data are then used for the quantification of reaction force and for tracking the sample displacement. Notably, we performed M-mode scanning in this study. The probe acquires signals from the same spatial location over a period of time.

3.2.1 Sample Preparation

We fabricated polydimethylsiloxane (PDMS) phantoms [74] to validate our method for robust stiffness measurement. These phantoms are prepared using a Sylgard 184 silicone elastomer base and curing agent. Titanium dioxide was added to provide light scattering for the sample. The stiffness of the phantom is adjusted by mixing various ratio of the base and curing agent. The mixture (PDMS base, curing agent and Titanium dioxide) was cured in a temperature-controlled oven at 65°C for 1hr. In this study,two different base-to-agent ratios (10:1 and 20:1) samples are fabricated for the experiments. The samples have

stiffness of approximately 2.6MPa and 1MPa, respectively [96]. Phantoms with different thicknesses were also prepared for this experiment.

3.3 Robust Stiffness Characterization Based on qOCE Measurement

Conventionally, elastic modulus of a material (E) measures the ratio of the stress (σ) and the strain (ε): E = σ/ε. However, when the stress and the strain are considered for 3D space and have spatial variation, direct measurement of E is challenging. In a conventional method, an indenter compresses the sample to obtain the strain. The reaction force (F) and indenter displacement (h) are measured. The elastic modulus is represented a simplified F-h model. Assume that, a flat cylindrical indenter compresses an infinitely thick sample, F-h relationship can be represented by Equation (3.6) [97].

$$F = \frac{2RhE}{1-\upsilon^2} \tag{3.6}$$

Here, R is the radius of the indenter and υ indicates the Poisson's ratio.

However, the assumption of an infinitely thick sample is often not accurate. Therefore, Equation (3.6) has limitation to provide the accurate estimation of tissue stiffness, because the measurement largely depends on the boundary conditions.

A modified model is developed, as shown in Equation (3.7), by introducing a constant coefficient (κ) that considers both the indenter geometry (R) and sample thickness (T) [98].

$$F = \kappa \left(\frac{R}{T}\right) \frac{2RhE}{1-\nu^2} \tag{3.7}$$

Here, $\kappa = \kappa$ (R/T)

However, during *in situ* characterization of tissue, spatial variation of mechanical properties is often unidentified. Therefore, an analytical solution is obtained according to

Equation (3.8) for the axial displacement d(z) within an isotropic, linearly elastic sample indented by qOCE probe [77]. This equation is capable of utilizing the qOCE measurement data for robust stiffness assessment.

$$d(z)|_{x=0,y=0} = \frac{h}{\pi\,(1-\nu)}\, Im[2(1-\nu)\log(2z+2iR) - \frac{z}{z+iR}] \tag{3.8}$$

Here, h is displacement of the indenter, z represents the axial (depth) coordinate in the 3D space, Im takes the imaginary part of a complex number.

Assume that the sample is incompressible (ν = 0.5). Consider, a parameter $m_{qOCE}(z)$ which is inversely proportional to the elastic modulus of the material. $m_{qOCE}(z)$ can be defined as the ratio of d(z) (Equation (3.8)) and F (Equation (3.6)) as shown in Equation (3.9).

$$m_{qOCE}(z) = \frac{d(z)}{F} = \frac{1}{E}\, M_R(z) \tag{3.9}$$

M_R on the right-hand side of Equation (3.9) has an analytical solution shown in Equation (3.10).

$$M_R(z) = \frac{3}{4\pi R}\, Im\,[2(1-\nu)\log(2z+2iR) - \frac{z}{z+iR}] \tag{3.10}$$

Therefore, E can be estimated by the linear curve fitting model shown in Equation (3.11).

$$\boldsymbol{m}_{qOCE} = \frac{1}{E}\, M_R \tag{3.11}$$

Here, $\mathbf{m}_{qOCE}$ is a vector and vector $\mathbf{M}_R = M_R(z)$ derives from the analytical solution of Equation (3.10). Figure 3.1 shows the extraction of sample elastic modulus by qOCE:

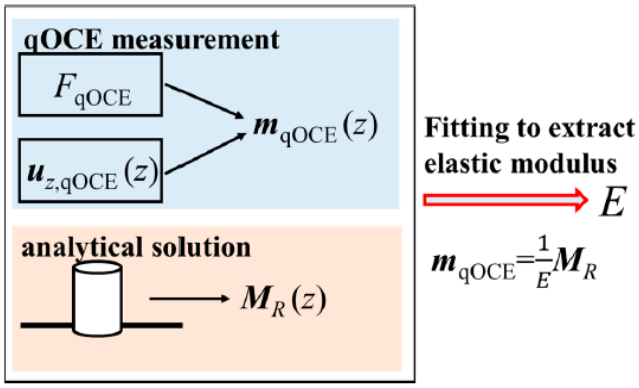

Figure 3.1 Extraction of elastic modulus using qOCE data.
Source: [152]

Figure 3.1 allows more robust assessment of sample stiffness for the following reasons. Firstly, the method quantifies both geometric deformation and reaction force which is an important factor to measure E. In comparison, conventional OCE only measures sample deformation and has limited capability to compute the material properties. Secondly, in conventional method, measured F and *h* are significantly affected by the boundary condition of the measurement. However, our method has considered the local displacement ($d(z)$) of the sample instead of the global deformation for the measurement.

3.4 Experimental Results

3.4.1 Measurement Capabilities of qOCE

First, the force sensing function of the qOCE system is validated. Force is applied through the qOCE probe to the sensing tip of a commercial force gauge. Doppler phase shift ($\Delta\Phi_{FP}$) is extracted from the OCT signal I_{FP}. Force reading from the force gauge is also measured. Afterwards, the coefficient α is calculated. α converts a Doppler phase shift to a force value:

F=$\alpha\Delta\Phi_{FP}$. With the coefficient α, force through the qOCE probe in a loading (increasing force) and an unloading (decreasing force) process can be extracted. The resultant force readings from OCT data are plotted in Figure 3.2. Figure 3.2 suggests that the instrument has the ability to quantify the force accurately both loading and unloading conditions.

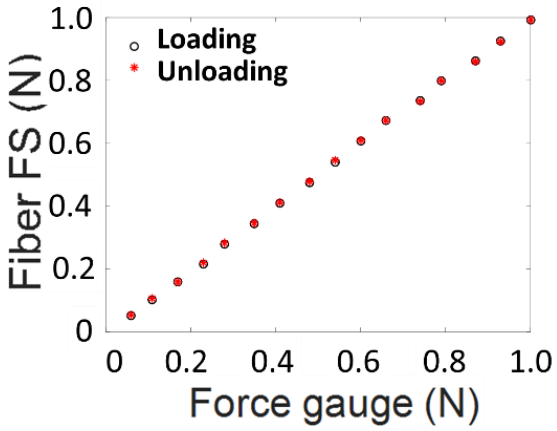

Figure 3.2 Comparison of force measurement of the qOCE instrument with the readings from a commercial force gauge.
Source: [152]

Next, we fabricated a thin (T = 1mm) elastic phantom to track depth resolved displacement ($d(z)$ by qOCE. The phantom is placed on a flat, rigid surface. A qOCE probe is attached to a high precision linear motor to perform the axial translation. The qOCE probe compressed the phantom and the OCT magnitude signal from the phantom is shown in Figure 3.3 (black curve with vertical axis on the right). The probe-sample interface is identified easily by the signal peak marked as green arrow in Figure 3.3. Figure 3.3 also shows the depth resolved displacement (blue and red curves with vertical axis on the left) of the sample obtained through Doppler analysis. We translated the qOCE probe by 0.1mm (h = 0.1mm) for the blue curve and by 0.2mm (h = 0.2mm) for the red curve. The displacement is approximately 0 at the probe-sample interface. Although the qOCE probe

was translated in axial direction by the linear motor, the probe-sample interface matched to a fixed optical path length. So, the displacement of OCT signal started from 0 at the surface of the sample.

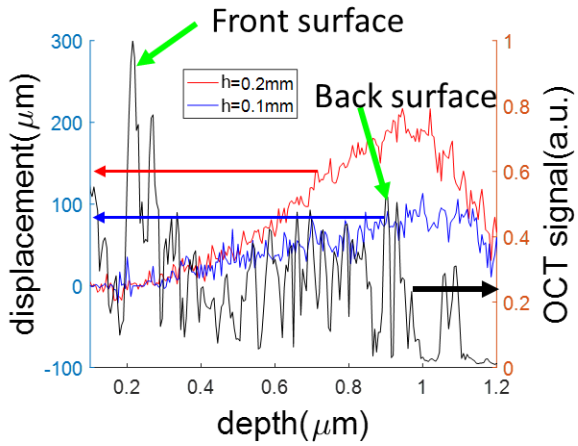

Figure 3.3 Magnitude of OCT signal (black curve to the right axis), and depth resolved displacements extracted through Doppler analysis (red and blue curves) to the left axis.
Source: [152]

Figure 3.3 also shows that the displacement ($d(z)$) increases gradually as z increases. Notably, OCT magnitude and sample displacement were non-zero beyond the sample thickness of 1mm. This is because, photons experienced multiple scattering events and these noisy signals due to multiple scattering was not used in stiffness assessment.

3.4.2 Quantification of Elastic Modulus using qOCE Data

We performed qOCE measurement on a cylindrical PDMS phantom with a 10:1 base-to-agent ratio (E = 2.6MPa, 6mm in thickness and 25mm in diameter). The probe is translated at a speed of 0.1mm/s and OCT signal is grabbed at a 50kHz A-scan rate. Different reaction forces were obtained as shown in Figure 3.4(a) from the fiber-optic force sensor by translating the probe with different displacements. Figure 3.4 (b) shows the displacement

fields ($d(z)$) established within the sample. Afterwards, $m_{qOCE}(z)$ was obtained for different indenter displacements by normalizing $d(z)$ with the corresponding reaction force F. The result is shown in Figure 3.4(c). $m_{qOCE}(z)$ remains same for the same sample as shown in Figure 3.4(c) when the indenter is translated with different displacements as described by Equations (3.9) - (3.11). Furthermore, the black solid curve of Figure 3.4(c) represents the analytical solution curve of $m_{qOCE}(z)$. The analytical solution (black curve) provides satisfactory approximation of the experimental data in a limited depth range (z<0.6mm). As the depth increases, $m_{qOCE}(z)$ calculated from qOCE data diverges more from the analytical solution more. This is because, OCT signal attenuates with depth and Doppler based displacement tracking becomes less accurate. Moreover, at larger depth, the actual displacement depends more on the measurement geometry. As a result, the analytical solution is applicable within a limited depth range and it is important to select a suitable depth range of qOCE data for the evaluation of sample stiffness.

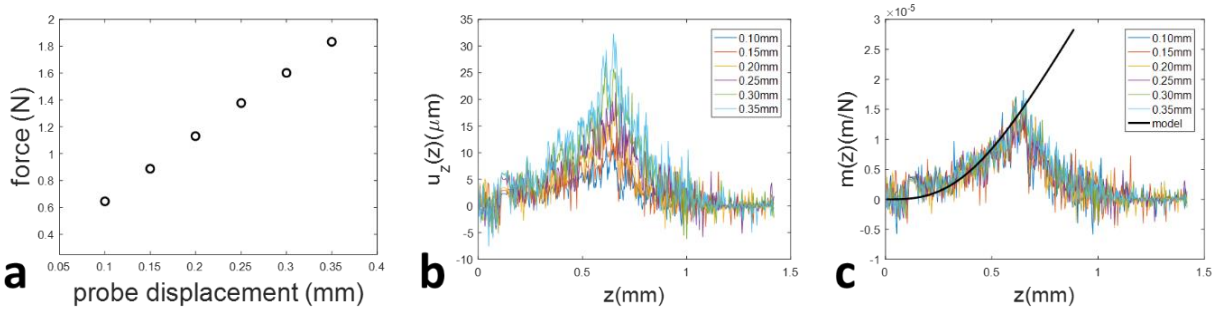

Figure 3.4 (a) Reaction force at different probe displacement; (b) depth resolved sample displacement at different probe displacement; (c) $m_{qOCE}(z)$ from experimental data and analytical expression.
Source: [152]

Additionally, we performed linear fitting of Equation (3.11) using the experimental acquired $m_{qOCE}(z)$ as shown in Figure 3.4(c) and analytical $M_R(z)$ obtained by Equation (3.10). Figure 3.5 (a) shows the resultant elastic moduli, where the error bars indicate 95%

confidential interval of the fitting. The known stiffness of PDMS (10:1) is also plotted in Figure 3.5(a) as the red line. The result is consistent with the curve fitted result of qOCE data. For comparison, the elastic modulus is calculated by the stress ($\sigma_a=F/A$ where F is the force reading from force sensor and A is the cross-sectional area of the qOCE probe) and the strain ($\varepsilon_a=h/T$ where h is the known probe displacement): $\sigma_a=E\varepsilon_a$. An over-estimated elastic modulus of 10.4MPa is observed in Figure 3.5(b) after the linear curve fitting of σ_a and ε_a. In addition, with the F-h data (Figure 3.5(c)), an underestimated elastic modulus of 2MPa is also extracted using Equation (3.6). In other words, when uniform strain is assumed within the entire thickness of the sample, overestimation of stiffness is calculated for the analysis based on apparent stress and apparent strain. In fact, the deformation of the sample under compression is limited to the volume in close proximity to the probe. The analysis based on F-h relationship estimates the stiffness, because the values of F and h are affected by the inflexible surface at a finite depth onto which we placed the phantom.

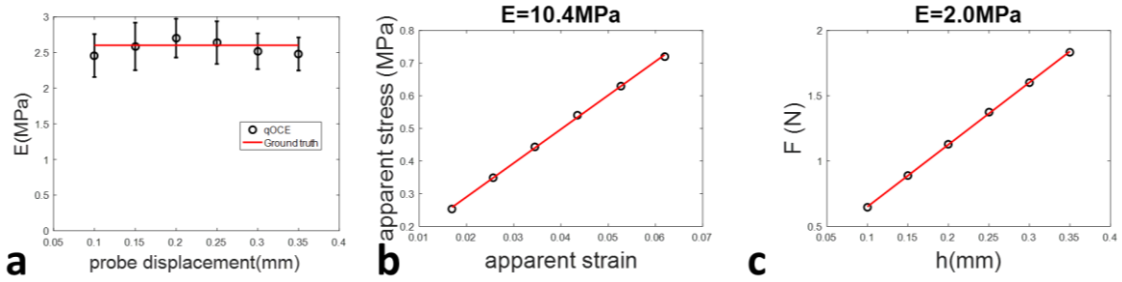

Figure 3.5 (a) Elastic moduli obtained using $m_{qOCE}(z)$ in consistent with the known material stiffness; (b) the relationship between apparent stress and apparent strain results in an overestimation of stiffness; (c) the relationship between reaction force and indenter displacement results in an underestimation of stiffness.
Source: [152]

3.4.3. qOCE Assessment of Stiffness on PDMS Samples with Different Thicknesses

qOCE assessment of stiffness is also performed on stiff and soft PDMS samples with different tissue thicknesses. The stiff sample was prepared with a 10:1 base-to-agent ratio, corresponds to a stiffness of approximately 2.6MPa. The soft sample was fabricated with a 20:1 base-to-agent ratio, corresponds to a stiffness of approximately 1.0MPa. The thicknesses of stiff and soft phantoms were 6mm (thick), 4mm (medium) and 2mm (thin). We translated the probe in the axial direction to compress the sample and to acquire qOCE data. Reaction force and depth resolved sample displacement were obtained at the end of the compression process. We then normalized the displacement ($d(z)$) with the reaction force (F), as shown in Equation (3.9). The resultant $m_{qOCE}(z)$ curves for stiff and soft samples are shown in Figure 3.6(a) and (b) (dashed lines), respectively. Linear curve fitting is applied according to Equation (3.11) to extract the elastic modulus. Remarkably, experimental data within a depth range of 0-330μm was used in the fitting. With the elastic modulus (E) extracted, the fitting results of ($M_R(z)/E$) are shown as solid lines in Figure 3.6(a) and (b). The consistency between the experimental results and the fitted analytical function validated the effectiveness of the simplified material model for qOCE measurement within a limited depth range. The elastic moduli from the stiff sample with large, medium and small thickness are plotted in Figure 3.6(c) (green bars). We compared these values with the value from literature (red bar). The elastic moduli of soft sample with large, medium and small thickness are shown in Figure 3.6(d) (green bars). We also compared those bars with the value obtained from the literature shown as red bar in Figure 3.6(c) and Figure 3.6(d). The plots suggest that our method can assess the tissue stiffness accurately regardless of variations of sample thickness.

As shown in Figure 3.6(a) and Figure 3.6(b), the displacement field extracted from qOCE measurement are not linearly dependent on depth. In other words, the extracted strain field is not spatially uniform. This is partially due to OCT signal attenuation with depth. As the depth increases, noisy signals dominate and OCT signal gets overwhelmed by noise. Therefore, the Doppler phase shift extracted from OCT signal cannot track the motion effectively.

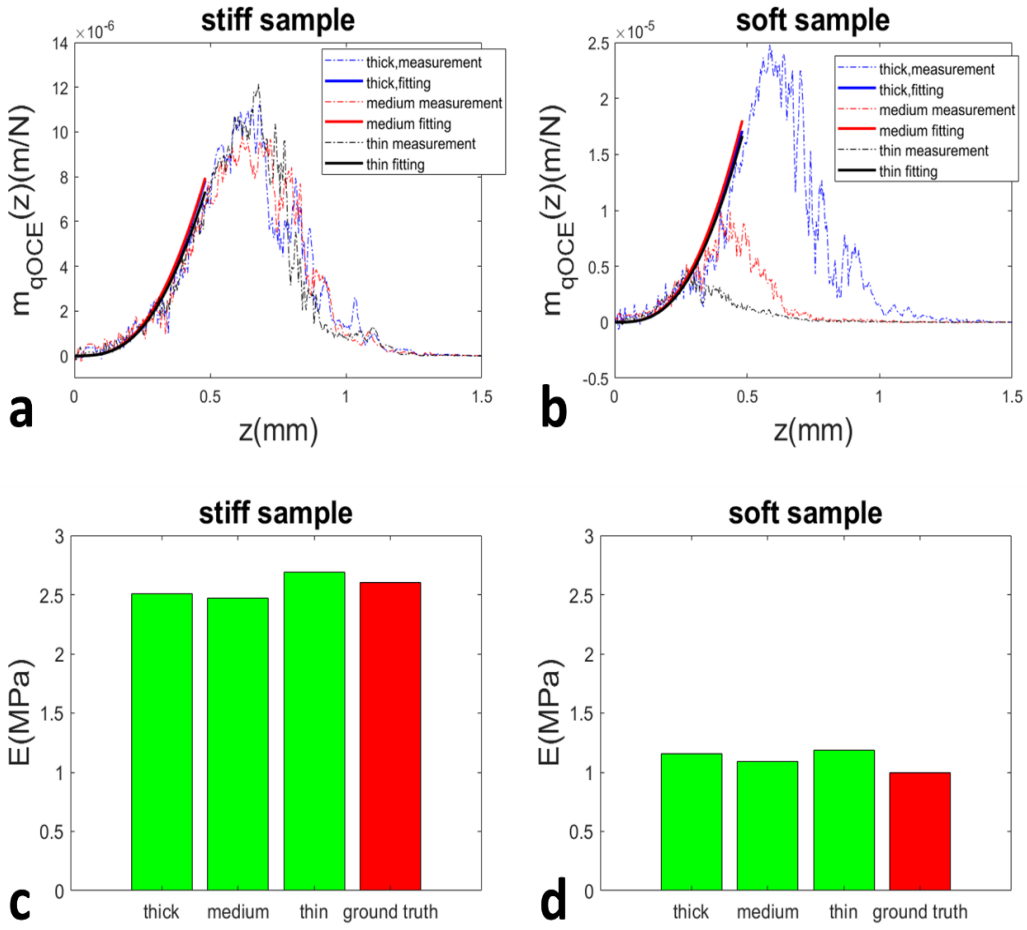

Figure 3.6 (a) Experimental results ($m_{qOCE}(z)$) from qOCE characterizations for stiff samples (E=2.6MPa) with different thicknesses, and curve fitting results; (b) experimental results ($m_{qOCE}(z)$) from qOCE characterizations for soft samples (E=1.0MPa) with different thicknesses, and curve fitting results; (c) elastic moduli from the stiff sample with large, medium and small thickness (green bars) compared to literature value (red bar); (d) elastic moduli from the soft sample with large, medium and small thickness (green bars) compared to literature value (red bar).

Source: [152]

A non-uniform strain field is developed within the sample. This is because, the sample is compressed by an indenter with a finite dimension. The strain field affected by the geometry of the sample is shown in Figure 3.6(b). Moreover, the spatial variation of displacement/strain also depends on the mechanical properties (Figure 3.6(a) versus Figure 3.7(6)). The displacement field of the deformed sample has complicacy for a wide range of factors. Yet, qOCE signal acquired from the volume by qOCE probe remains constant. This suggests that qOCE can perform robust *in situ* mechanical characterization of tissues with unknown boundary conditions.

3.5 Conclusion

In this chapter, we presented a method that analyzed the data obtained from the qOCE system, to achieve robust stiffness assessment. We normalized the displacement field (d(z)) with the reaction force (F) and fit the result with an analytical model to extract the elastic modulus. Our result has shown a significant improvement in measuring the tissue stiffness for different measurement geometry. Therefore, we anticipate that our qOCE method can be applied for margin assessment in breast cancer surgery.

CHAPTER 4

TEMPORALLY AND SPATIALLY ADAPTIVE DOPPLER ANALYSIS FOR ROBUST HANDHELD OPTICAL COHERENCE ELASTOGRAPHY

4.1 Introduction

Chapter 4 presents the development of a handheld OCE instrument that will allow the clinician to conveniently interrogate the localized mechanical properties of *in vivo* tissue, leading to better informed clinical decision making. During handheld OCE characterization, the handheld probe compresses the sample and the displacement of the sample is quantified by analyzing the OCT signals acquired. However, the motion within the sample inevitably varies in time due to varying hand motion. Moreover, the motion speed depends on spatial location due to the sample deformation. Hence, there is a need for a robust motion tracking method for manual OCE measurement. In this chapter, we would describe a temporally and spatially adaptive Doppler analysis method. The method described here strategically chooses the time interval (δt) between signals involved in Doppler analysis to track the motion speed $v(z,t)$ that varies temporally and spatially in a deformed sample volume under manual compression. The results are obtained from phantom experiments and *in vivo* tissue characterization, to demonstrate the effectiveness of the adaptive Doppler analysis for motion tracking in a dynamic manual loading process.

4.2 Motivation for Adaptive Doppler Analysis for Handheld OCE Probe

OCT allows structural and functional imaging of biological tissue with high resolution and high speed [16]. The imaging capability of OCT can be integrated into handheld instruments using fiber optic components [99 - 101]. A compact, lightweight handheld

OCT probe allows a clinician to interrogate tissue characteristics at different anatomical locations [102, 103]. Therefore, handheld OCT imaging instrument is attractive for many clinical applications, including guiding vitreous-retinal surgery, delineating tumor margin for surgical excision, and guiding tissue biopsy for the diagnosis of breast or prostate cancer. A handheld OCT instrument can use the magnitude of OCT signal to reveal morphological features of the tissue. With further signal processing, other characteristics of the tissue related to its physiological and pathological status can be extracted. One feature of clinical interest is the mechanical properties of tissue. For diseases such as breast cancer and prostate cancer, cancerous tissue has a larger stiffness compared to normal tissue [8]. Therefore, manual palpation as well as elastography technologies, have been used in assessing the stiffness of these diseases in clinic [44, 86, 87].

Despite great challenge in quantifying mechanical properties through OCE measurement, depth resolved displacement obtained by analyzing OCT signal can be used as an effective surrogate for sample stiffness. With the assumption of uniform distribution of stress (σ that remains constant for different spatial locations), the strain is directly related to the stiffness of the sample ($\varepsilon=\sigma/E$ where E indicates the Young's modulus and quantifies the stiffness of the sample). Therefore, under the same stress σ, the strain ($\varepsilon=\frac{d\delta L(z)}{dz}$ evaluated by the spatial derivative of displacement $\delta L(z)$ [95]) is larger for a soft material with a smaller E and is smaller for a hard material with a larger E, as indicated in Figure 4.1. Tissue under different pathophysiological conditions have different stiffness, hence OCE measurement of displacement and strain allows *in situ* tissue characterization. For example, cancerous tissue has a larger stiffness compared to normal tissue. A positive margin at the site of tumor excision with residual cancerous tissue can thus be identified

by evaluating the displacement generated through manual OCE measurement. The displacement increases with depth, and the position where the slope of displacement changes abruptly implies the boundary between the cancerous tissue and the normal tissue. Therefore, OCE characterization can reveal highly localized mechanical contrast and hence lead to better interpretation about clinical decision making, without fully quantifying the mechanical properties of the tissue.

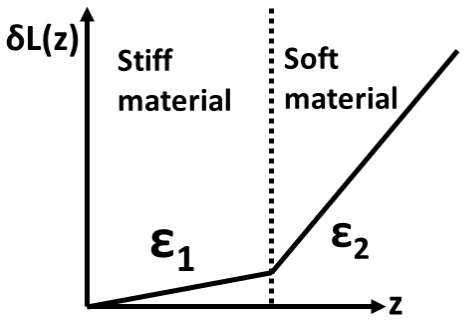

Figure 4.1 Illustration of depth resolved displacement for a sample with different stiffness at different depth. Here, $\varepsilon_1 < \varepsilon_2$.
Source: [92]

Particularly, a compact OCE instrument can be used as a conventional handheld instrument. The tissue is manually compressed by the OCE device and the motion of the tissue is tracked by analyzing OCT signal. A handheld OCE instrument hence performs high sensitivity virtual palpation of the tissue with great convenience and flexibility. Moreover, fiber optic OCE instruments can be integrated into a needle device, delivering the capability of mechanical characterization to tissue that is deeply embedded. However, the major challenge for manual OCE characterization of tissue is the unpredictable and unstable hand maneuver that is used to generate mechanical excitation (compression) in tissue. The deformation of the sample under the known pattern of mechanical excitation is tracked by analyzing OCT signal. In conventional compression OCE measurement, the

sample has a well-defined geometry and undergoes quasi-static compression. Alternatively, the mechanical excitation can be impulse or sinusoidal function [74, 93]. However, with a handheld OCE instrument, it is challenging to impose mechanical excitations that are quasi-static, impulsive or sinusoidal. The manual loading process often generates a motion speed that varies with time. In addition, the sample deforms under compression, implying spatial variation of motion characteristics. Hence, there is a requirement for a motion tracking method that enables robust motion tracking for manual OCE measurement.

Motion tracking in OCE can be achieved through Doppler analysis or speckle decorrelation analysis. Speckle analysis has a smaller dynamic range and is more appropriate to track motion with larger magnitude [62, 106]. In this study, Doppler analysis is used to quantify the axial motion speed and displacement. A simple and effective method for temporally and spatially adaptive Doppler analysis is investigated here. The adaptive Doppler analysis method strategically chooses the time interval (δt) between signals involved in Doppler analysis, to track the motion speed $v(z,t)$ that varies temporally in a manual compression process and spatially in a deformed sample volume. The method is validated in OCE system with a handheld single fiber probe and real-time signal processing software based on GPU. To achieve robust motion tracking, we calculate high density (HD) Doppler phase shift that is most unlikely to have phase wrapping artifact and average the HD Doppler signal to estimate the speed of axial motion from which we derive a time interval to achieve a large yet an artifact free Doppler phase shift. The premise of this method is that (1) directional motion affects larger scale characteristics of the Doppler signal and can be estimated through averaging; (2) noise characteristics in estimated

Doppler phase shift are independent of the time interval δt while the signal due to directional motion does. Enabled by high signal acquisition and processing speed, we perform an online estimation of the motion speed, select an optimal δt adaptively, and perform robust motion tracking for OCE measurement.

4.3 Principle for Adaptive Doppler Analysis

In OCE characterization, the loaded sample deforms during compression process. The sample displacement depends on spatial location ($\delta L(z)$). With local displacement $\delta L(z)$ extracted by OCT signal, localized axial strain, the spatial derivative of the displacement (Equation (4.1)), is calculated as the sample stiffness. For sampled OCT image, local strain can be calculated either through finite difference approach or least square estimation.

$$\varepsilon(z) = \frac{d}{dz}\left[\delta L(z)\right] \tag{4.1}$$

Notably, the motion within a deformed sample under axial compression is generally 3D with axial and lateral components. However, Doppler phase analysis is only sensitive to axial motion. Besides, our measurement geometry has cylindrical symmetry and the light beam propagates along the axis of cylindrical symmetry. Hence, the lateral displacement of an isotropic sample by the incident light beam is minimum.

Doppler phase shifts between OCT A-scans are calculated to acquire 1D depth resolved OCE signal. Consider, OCT signal with complex value at the k^{th} pixel of an A-scan (m^{th} A-scan) and that at the k^{th} pixel of another A-scan ($(m + \Delta_{k,m})^{th}$ A-scan). A non-zero Doppler phase shift ($\delta\phi_{k,m}=\delta\phi(k\delta z, mT_0)$) is anticipated due to the axial displacement at depth $z=k\delta z$ within the time interval $\Delta_{k,m}T_0$. Here δz designates the depth sampling interval by pixels in an A-scan and T_0 indicates the acquisition time interval between the

adjacent A-scans. $\delta\phi_{k,m}$ is linearly correlated to the axial motion speed $v_{k,m}$ (assuming a constant axial motion within the observation time: $v_{k,m}=v(k\delta z,mT_0)$ at depth $k\delta z$ within time interval from mT_0 to $(m+\Delta_{k,m})T_0$, as shown in Equation (4.2) where λ_0 is the central wavelength of the light source [107].

$$\delta\phi_{k,m} = 4\pi\frac{v_{k,m}\delta t}{\lambda_0} = 4\pi\frac{v_{k,m}\Delta_{k,m}T_0}{\lambda_0} \tag{4.2}$$

The Doppler phase shift $\delta\phi_{k,m}$ is calculated according to Equation (5.3) [55], where $I_{k,m}=I(k\delta z,mT_0)$ indicates the complex OCT signal at the k^{th} pixel of an A-scan obtained at time mT_0; $I_{k,m+\Delta(k,m)}=I(k\delta z,(m+\Delta_{k,m})T_0)$ indicates the complex OCT signal at the k^{th} pixel of an A-scan obtained at time $(m+\Delta_{k,m})T_0$; atan(·) indicates to take the arctangent; Im(·), Re(·) and (·)* indicate to take the imaginary part, the real part and the complex conjugate of a complex value, respectively.

$$\delta\hat{\phi}_{k,m} = atan\left[\frac{\mathrm{Im}\left(I_{k,m}^{*}I_{k,m+\Delta_{k,m}}\right)}{\mathrm{Re}\left(I_{k,m}^{*}I_{k,m+\Delta_{k,m}}\right)}\right] \tag{4.3}$$

The relationship between the estimated Doppler phase shift $\delta\hat{\phi}_{k,m}$ and the actual phase shift $\delta\phi_{k,m}$ due to motion $v_{k,m}$ is shown in Eq (4.4), where $n_{k,m}$ is the random phase noise deriving from various noises in OCT measurement (shot noise, thermal noise, excess noise, speckle noise, etc). On the other hand, $N_{k,m}$ is an integer and is non-zero when $|\delta\phi_{k,m}|>\pi/2$: $N_{k,m} = \left\lfloor\frac{\delta\phi_{k,m}+sign(\delta\phi_{k,m})\frac{\pi}{2}}{\pi}\right\rfloor$. In other words, for $|\delta\phi_{k,m}|>\pi/2$, phase wrapping arises, because the arctangent (atan) function calculated for the phase shift in Equation (4.3) cannot differentiate an arbitrary phase shift $\delta\phi_{k,m}$ and $\delta\phi_{k,m}+N_{k,m}\pi$ [47, 114]. Clearly, $N_{k,m}$ depends on time ($t = mT_0$) and space ($z = k\delta z$).

$$\delta\hat{\phi}_{k,m} = \delta\phi_{k,m} - N_{k,m}\pi + n_{k,m} \tag{4.4}$$

Afterwards, axial motion speed is: $\hat{v}_{k,m} = \frac{\lambda_0}{4\pi T_0 \Delta_{k,m}} \delta\hat{\phi}_{k,m}$ for the k^{th} pixel in the m^{th} A-scan and the estimated depth resolved displacement ($\delta\hat{L}_k$=$\delta\hat{L}(k\delta z)$) over the entire compression process is: $\delta\hat{L}_k = \sum_{m=1}^{M}(\delta\hat{v}_{k,m}T_0) = \frac{\lambda_0}{4\pi\Delta_{k,m}}\sum_{m=1}^{M}\delta\hat{\phi}_{k,m}$ where M indicates the total number of A-scans obtained during the sample compression process. $\delta\hat{L}_k$ can thus be expressed as Equation (4.5).

$$\delta\hat{L}_k = \delta L_k - \frac{\lambda_0}{4\Delta_{k,m}}\sum_{m=1}^{M} N_{k,m} + \frac{\lambda_0}{4\pi\Delta_{k,m}}\sum_{m=1}^{M} n_{k,m} \tag{4.5}$$

On the right hand side of Equation (4.5), the first term represents the actual displacement; the second term represents the phase wrapping artifact and the third term denotes the contribution from random phase noise. To improve the sensitivity, SNR and dynamic range for OCE characterization, a smaller variance (Var($\delta\hat{L}_k$-δL_k)) is desired for the estimated displacement. Assume, $n_{k,m}$ (m=1, 2, 3, …, M) is Gaussian and independent in different A-scans with variance shown in Equation (4.6). Therefore, considering $N_{k,m}\equiv 0$, the variance in displacement tracking is given by Equation (4.7).

$$Var\left(n_{k,m}\right) = \beta\frac{1}{SNR} \tag{4.6}$$

$$Var\left(\delta L_k\right) = \frac{\lambda_0 M}{4\pi\Delta_{k,m}} Var\left(n_{k,m}\right) \tag{4.7}$$

In Equation (4.7), λ_0 depends on the OCT system of the imaging study; M depends on the time period of the sample loading process; $Var(n_{k,m})$ is determined by the OCT system as well as the optical characteristics of the sample. Hence $\Delta_{k,m}$ is the only parameter that can be varied to improve the displacement tracking. Noise in displacement tracking

for a given compression process can be suppressed by selecting a larger value of $\Delta_{k,m}$.

Moreover, $N_{k,m} \equiv 0$ is required for unbiased displacement tracking. Therefore, the time interval between A-scans for Doppler phase calculation ($\delta t = \Delta_{k,m} T_0$) has to be sufficiently small, so that $|\delta\phi_{k,m}| = |4\pi v_{k,m} \Delta_{k,m} T_0 / \lambda_0| \leq \pi/2$., The condition for avoiding the phase wrapping artifact in Doppler analysis is:

$$\Delta_{k,m} \leq \frac{\lambda_0}{8 v_{k,m} T_0} \tag{4.8}$$

Equation (4.8) infers that the optimal choice of $\Delta_{k,m}$ depends on the motion speed ($v_{k,m}$). For a handheld OCE instrument, the motion speed within the sample depends on the depth because the sample deforms in the axial direction. The motion speed also varies with time due to the non-constant compression speed. Therefore, $v_{k,m} = v(k\delta z, mT_0)$ and an adaptive optimal time interval ($\delta t = \delta t(z,t)$) is necessary for Doppler analysis to the spatial location and time. For sampled OCT A-scans, $\delta t = \Delta_{k,m} T_0 = \Delta(k\delta z, mT_0) T_0$ where $\Delta_{k,m}$ is an integer. In other words, different values are chosen for $\Delta_{k,m}$ at different depth ($z = k\delta z$) and at different time ($t = mT_0$) (Figure 4.2(a) and (b)).

In contrast, conventional Doppler analysis tracks displacement by comparing OCT signals collected at constant time interval (Figure 4.2 (c)) irrespective of time and spatial location. Therefore, Doppler analysis results suffer from phase wrapping artifact and suboptimal SNR, mostly for a manual OCE characterization process.

In order to adaptively determine the value of $\Delta_{k,m}$ to spatial location ($z = k\delta z$) and time ($t = mT_0$), the motion speed $v_{k,m}$ is estimated by calculating the high density (HD) Doppler phase shift. Discrete OCT signals are acquired frame by frame and each frame consists of multiple (M_0) A-scans with a time interval of T_0. For the i^{th} frame of OCT data, the k^{th} pixel in the j^{th} A-scan is $I_{k,m}$, where $m = j + (i-1)M_0$. The HD Doppler phase shift $\delta\hat{\varphi}_{k,m}$

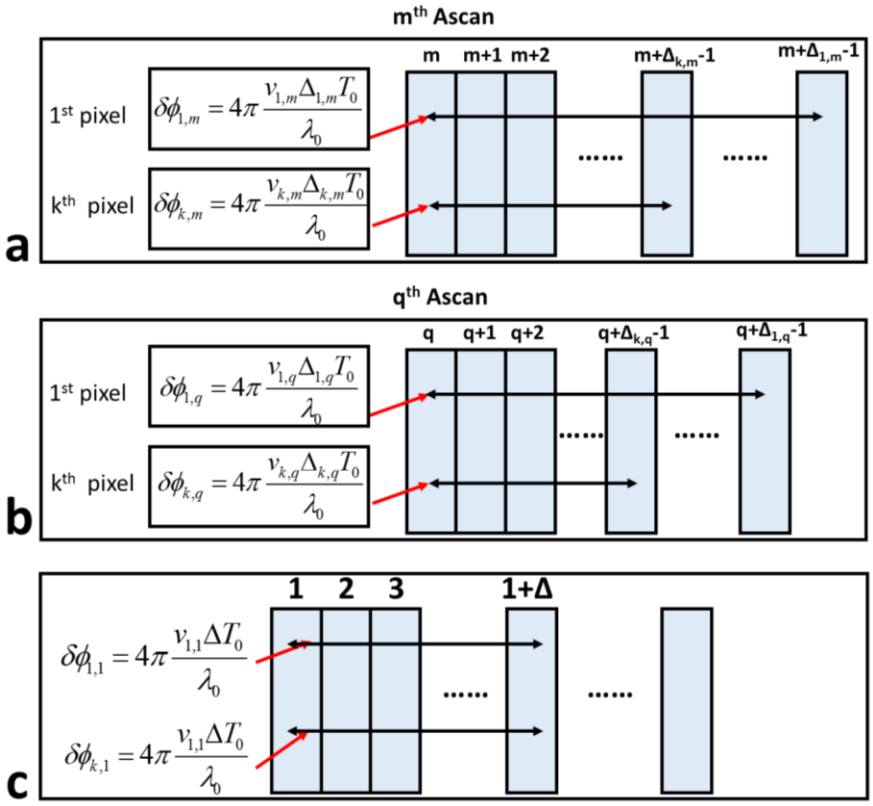

Figure 4.2 (a) and (b) Adaptive selection of time intervals for Doppler analysis. Here, time intervals between 1st and kth pixels (length of black arrows) for (a) and (b) are different; (c) Time interval for conventional Doppler analysis. Both the black arrows have same time interval for different depth.
Source: [92]

is measured between $I_{k,m}$ and $I_{k,m+1}$ according to Equation (4.3) with $\Delta_{k,m}\equiv 1$. Afterwards, calculate mean HD Doppler phase shift for the i^{th} frame of OCT data is estimated by ($\delta\bar{\varphi}_{k,i}=\frac{1}{M_0}\sum_{j=1}^{M_0}\left[\delta\hat{\varphi}_{k,j+(i-1)M_0}\right]$) and axial motion speed at the k^{th} pixel at depth $k\delta$z is: $\frac{\delta\bar{\varphi}_{k,i}}{4\pi T_0}\lambda_0$. Estimation of motion speed has a temporal resolution determined by the time needed to capture a frame of OCT data (M_0T_0), and the motion speed for the m^{th} A-scan is thus approximately $\hat{v}_{k,m}=\frac{\delta\bar{\varphi}_{k,i}}{4\pi T_0}\lambda_0$ where $i=\left\lfloor\frac{m}{M_0}\right\rfloor+1$ and $\lfloor\ \rfloor$ indicates to take the integer part of a rational number. With the estimated motion speed, the Doppler phase shift gathered within a time interval δt is thus $4\pi\frac{\hat{v}_{k,m}}{\lambda_0}\delta t$. It requires $|4\pi\frac{\hat{v}_{k,i}}{\lambda_0}\delta t|\leq\frac{\pi}{2}$ to prevent

phase wrapping from happening. For discrete OCT signal, $\delta t = \delta t_{k,m} = \Delta_{k,m} T_0$ where $\Delta_{k,m}$ is an integer determined by Equation (4.9) with $W > 1$. $\Delta_{k,m}$ is assigned with a value of 1, for the result obtained by Equation (4.9) to be smaller than 1. Moreover, it requires $\Delta_{k,m}$ to be smaller than $M_0/2$ to calculate Doppler phase shift between A-scans within one frame of OCT data. If the value calculated using Equation (4.9) is larger than $M_0/2$, we consider $\Delta_{k,m}=M_0/2$.

$$\Delta_{k,m} = \left\lfloor \frac{\pi M_0}{\left| 2W \sum_{j=1}^{M_0} \left(\delta\hat{\varphi}_{k,j+(i-1)M_0} \right) \right|} \right\rfloor \tag{4.9}$$

Notably, $W>1$ and the method is robust against phase wrapping when phase noise exists. As validated in previous studies including our recent work [111–113], the level of phase noise in the OCT imaging system is inversely proportional to the signal to noise ratio (SNR) of amplitude OCT signal. In this study, other than specifically mentioned, $W = 2$ for the calculation of adaptive time interval for Doppler analysis.

After the selection of adaptive time interval for Doppler analysis ($\delta t_{k,m}=\Delta_{k,m}T_0$), Doppler phase shift ($\delta\hat{\phi}_{k,m}$) between A-scan pairs $I_{k,m}$ and $I_{k,m+\Delta(k,m)}$ is calculated according to Eq (4.3). $\delta\hat{\phi}_{k,m}$ is then transformed to the incremental displacement ($\delta l_{k,m}=(\lambda_0\delta\hat{\phi}_{k,m})/(4\pi\Delta_{k,m})$). Hence, the total displacement over the entire compression process with M A-scans is calculated for the specific depth (k^{th} pixel) during the entire compression process: $\delta L_k=\sum_{m=1}^{M}(\delta l_{k,m})$. Depth resolved strain of the loaded sample is calculated to evaluate the stiffness.

In summary, the adaptive Doppler analysis is illustrated in Figure 4.3 in real-time GPU. The software grabs spectral interferograms frame by frame, performs fast Fourier transform on the spectral interferograms, calculates the HD Doppler phase shift to estimate

the speed of axial motion, adaptively determines the optimal time interval for each frame of OCT data to perform Doppler analysis, and tracks the depth resolved displacement for sample mechanical characterization.

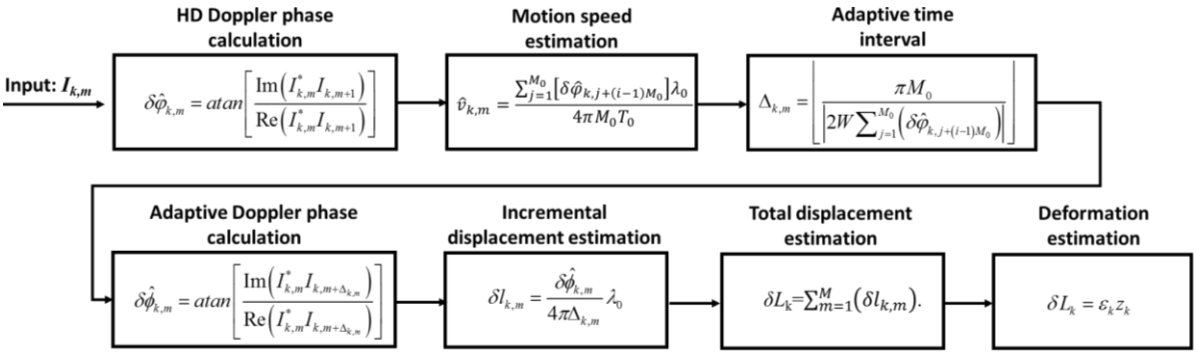

Figure 4.3 Block diagram for adaptive Doppler analysis.
Source: [92]

4.4 Experimental Setup

The spectral domain OCT system described in Chapter 2 is used. To validate the method of adaptive Doppler analysis under well controlled loading conditions, we conducted OCE experiment on the setup shown in Figure 4.4(a) where the sample is sandwiched between two rigid places. One of the plates has a glass window that allowed broadband light to incident into the sample for OCT imaging, and the other plate is attached to a high precision vertical translational stage actuated by a linear motor. Here, common path OCT imaging configuration is used where the reference light is derived from a constant reflector at the probe arm. The reference arm shared the same optical path as the sample light and random phase variation due to environmental perturbation is minimal. The phase noise largely derived from discrepancy of optical signal is determined by Equation (4.6). In Figure 4.4(a), the bottom surface of the glass window provides a reference light that interferes with sample light to generate interferometric OCT signal. The reference light and sample

light are combined and directed by a circulator for detection. The rigid bottom surface of the window ensured a constant optical path length (z = 0) and did not move during compression. Hence, the displacement ($\delta L(z)$ extracted by OCT signal gradually increased with depth starting from the value of 0, as shown in the inset of Figure 4.4 (a).

A Thorlabs scanning lens (LSM02, Thorlabs, with 11μm beam diameter on the focal plane and 70μm depth of field) is used as the imaging object. The scanning lens uses a broadband light source for illumination and has minimal chromatic aberration.

The elastic phantom used in this study is prepared by curing silicone rubber, RTV-22 purchased from Raw Material Suppliers. Titanium dioxide particles is added into the silicone gel before curing to provide light scattering. The sample is considered to have homogeneous mechanical (stiffness) and optical (light scattering and absorption) properties. The elastic phantom used in this study is shown in Figure 4.4(a) (photo and OCT image).

Robust mechanical characterization through a handheld probe are shown in Figure 4.4(b). The probe has simply a single mode fiber with a flat fiber tip and a 3D printed handle. The fiber probe is connected to the port-2 of the circulator for sample illumination and OCT signal acquisition. The Fresnel reflection at the fiber tip served as the reference light for the common path OCT imaging. So, the fiber tip worked as the origin of the spatial coordinate for OCT imaging ($z = 0$) and did not deform under compression in Figure 4.4(a). The displacement gathered by OCT signal increased gradually with the depth starting from the value of 0, as shown in the inset of Figure 4.4(b).

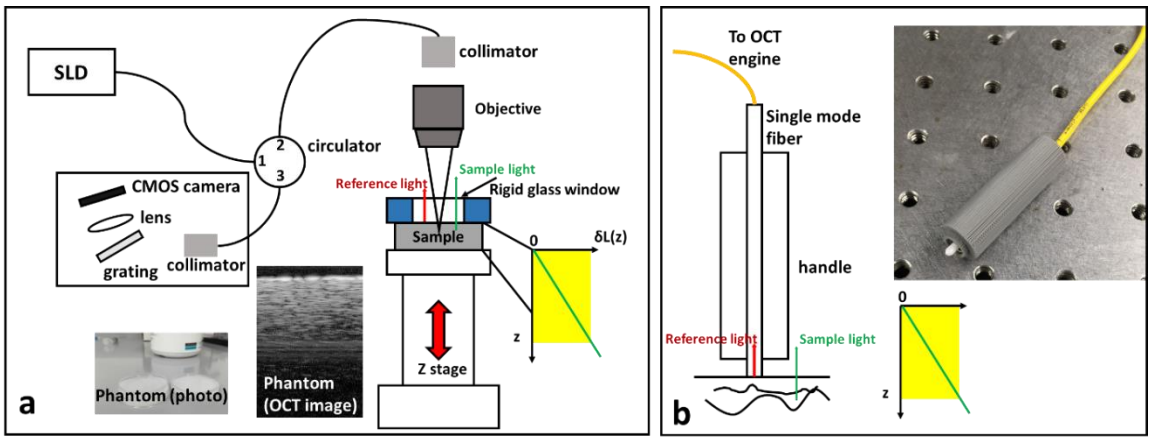

Figure 4.4 (a) Benchtop setup for experimental validation of the method for adaptive Doppler analysis; (b) fiber optic probe for handheld OCE characterization.
Source: [92]

4.5 Experimental Results

The speed of the algorithm is implemented in CUDA. The software processed approximately 288k A-scans per second. The signal processing speed is much faster than the maximum data acquisition rate of the camera (92k A-scans per second). Moreover, the procesing time to perform adaptive Doppler analysis on a frame of OCT data is approximately 0.1ms.

4.5.1 Need for Adaptive Time Interval for Optical Doppler Tracking

To demonstrate the need for an adaptive time interval (δt) in OCE measurement through a manual compression process, we acquired experimental data from the benchtop setup as shown in Figure 4.4 (a). We translated the z-stage at two different speeds (v_{motor} = 0.2mm/s and v_{motor} = 0.1mm/s) to compress the elastic sample sandwiched between the two rigid plates (shown in Figure 4.4 (a)). At each motor translation speed, a frame of OCT data (with 1024 A-scans, i.e., M_0 =1024) is grabbed with a time interval of 16μs between adjacent A-scans (T_0 =16μs). First, we demonstrated how the Doppler signal and noise

determined by the time interval between OCT signals involved in phase shift calculation. For each frame of OCT data, we selected the pixel at the depth z =1mm ($z = k\delta z$ =1mm) from an A-scan (j^{th} A-scan) and calculated the mean phase shift between OCT signal at this pixel ($I_{k,j}$) and OCT signal in subsequent A-scans acquired with different time delays ($I_{k,j+\Delta}$, Δ=1, 2, 3, …):

$$\delta\bar{\phi}(\delta t) = \frac{1}{M_0-\Delta}\sum_{j=1}^{M_0-\Delta}\delta\hat{\phi}_j(\delta t) \tag{4.10}$$

where $\delta\hat{\phi}_j(\delta t) = \arg\left(I_{k,j}^* I_{k,j+\Delta}^*\right)$.

Doppler phase shifts ($\delta\bar{\phi}(\delta t)$) at the specific depth between A-scans with different time intervals ($\delta t = \Delta \times T_0$) are shown in Figure 4.5(a) as blue (v_{motor} = 0.2mm/s) and red (v_{motor} = 0.1mm/s) curves. In Figure 4.5(a), $\delta\bar{\phi}(\delta t)$ initially increases linearly with δt, which is consistent with Equation (4.2). However, with a larger motor translation speed (blue curve in Figure 4.5(a) with v_{motor} = 0.2mm/s), phase wrapping artifact arises when $\delta\bar{\phi}(\delta t)$ approaches and exceeds π/2. In contrast, data for smaller motor translation speed (red curve in Figure 4.5(a) with v_{motor} = 0.1mm/s) are free of phase wrapping artifact for the same δt. Figure 4.5(a) suggests that the selection of adaptive time interval for Doppler analysis is required for the compressor during OCE characterization. In addition, the calculated phase using Equation (4.3) also varies due to random noise. Using $\delta\hat{\phi}_j(\delta t)$, the random noise of the estimated Doppler phase can be estimated as:

$$\sigma_\phi(\delta t) = \sqrt{\frac{1}{M_0-\Delta-1}\sum_{j=1}^{M_0-\Delta}\left(\delta\hat{\phi}_{j,\Delta} - \delta\bar{\phi}_\Delta\right)^2} \tag{4.11}$$

Figure 4.5(b) shows the phase attained with different time intervals ($\delta t = \Delta \times T_0$). $\sigma_\phi(\delta t)$ as blue (v_{motor} = 0.2mm/s) and red (v_{motor} = 0.1mm/s) curves. A peak is found in the

blue signal in Figure 4.5(b). This is because, Doppler signal varies considerably when phase wrapping occurs (blue signal in Figure 4.5(a)). The noise in Doppler phase estimation remains approximately constant for different values of δt. This is because random phase variation in OCT signal originates from noise in OCT measurement and random environmental perturbations which is temporally independent and identically distributed random variables, according to Equation (4.6). Therefore, the results of Doppler analysis have a similar level of noise, despite different time intervals δt. According to Equation (4.7), a larger value of $\Delta_{k,m}$ is required to achieve a minimal error in the displacement tracking, because the phase noise does not increase with time (Figure 4.5(b)) while the phase shift due to directional motion increases with time (Figure 4.5(a)).

In addition, the displacement within the sample under OCE characterization also varies as spatial location due to the sample deformation under compression. The deformation measured as axial strain (Equation (4.1)) can characterize the mechanical properties of the sample. Therefore, Doppler analysis also needs to be adaptive to the spatial location. To demonstrate this, one frame of OCT data with $v_{\text{motor}} = 0.2$mm/s is used and Doppler phase shift are calculated between pixels at depth z =1mm with different time intervals, as well as, Doppler phase shift at a smaller depth (z = 0.5mm). Figure 4.5(c) shows the mean value of Doppler phase shifts for different δt. Doppler phase shift in Figure 4.5(c) initially increases linearly with δt. For Doppler phase shift calculated for a larger depth (blue curve

in Figure 4.5(c) corresponds to z = 1mm), phase wrapping artifact rises as $\delta\phi$ approaches and exceeds $\pi/2$. In contrast, for a smaller depth (red curve in Figure 4.5(c) with z = 0.5mm) the signals are free from the phase wrapping artifact for the same time range. Therefore,

the selection of adaptive time interval for Doppler analysis is essential to the spatial

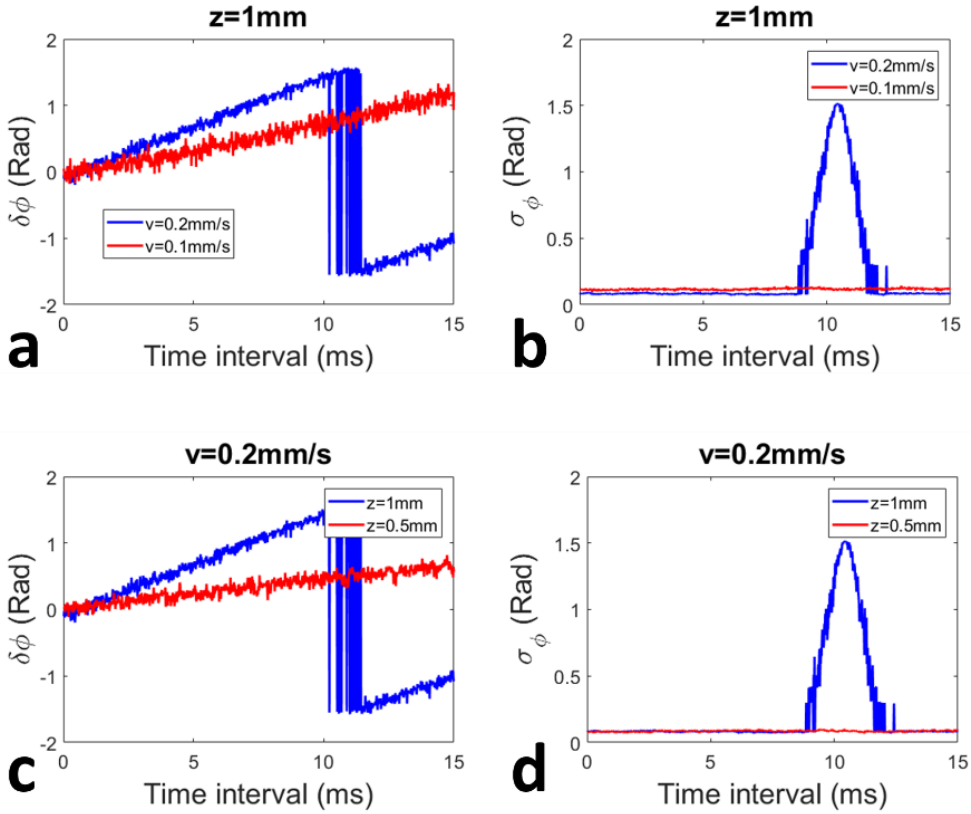

Figure 4.5 Doppler phase shift (a) and phase noise (b) obtained from the sample at the same depth with different motor translation speeds; Doppler phase shift (c) and phase noise (d) obtained from the sample at the different depths with the same motor translation speed. *Source: [92]*

location inside the deformed sample. We also investigated the random noise for Doppler phase shift at different depths for the same set of OCT data with v_{motor} = 0.2mm/s. The results are shown in Figure 4.5(d) as blue (z =1mm) and red (z = 0.5mm) curves. Regardless of a peak detected in the blue curve due to the phase wrapping, Doppler signals display a constant noise level for various δt values.

4.5.2 Impact of Selection of Time Interval on Depth-Resolved Displacement

Next, we demonstrated the impact of time interval selection for Doppler analysis on the tracking of depth resolved displacement. Using the benchtop configuration shown in Figure. 4.4(a), we translated the motor at various speed ranges (v_{motor} = 0.1mm/s, 0.3mm/s, 0.5mm/s, 0.7mm/s and 0.9mm/s) to deform the sample inserted between two rigid plates. We used the OCT engine to capture the spectral interferograms simultaneously from the phantom experienced compression. We calculated Doppler phase shift ($\delta\hat{\phi}_{k,m}$ where k is the index of pixel in an A-scan and m is the A-scan index) between complex OCT signals at pixels in the m^{th} A-scan ($I_{k,m}$) and in the $(m+\Delta)^{th}$ A-scan ($I_{k,m+\Delta}$). We transformed the phase shift to the displacement $\delta l_{k,m} = (\lambda_0\delta\hat{\phi}_{k,m})/(4\pi)$, and estimated the displacement for the compression: $\delta L_k = \delta L(k\delta z)=\sum_{m=1}^{M}(\delta l_{k,m})$.

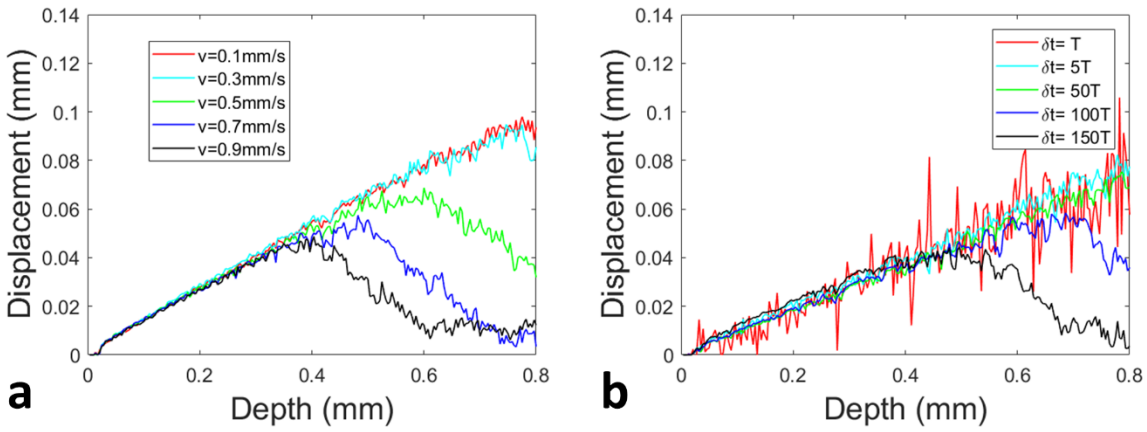

Figure 4.6 Depth resolved displacement (a) obtained with different motor speeds and the same time interval ($\delta t = \Delta \times T_0$, where T_0=16μs and time delay, Δ=50) for Doppler analysis; (b) obtained with the same motor speed (v_{motor} = 0.25mm/s) and different time intervals for Doppler analysis. Here, T = T_0 = 16μs.
Source: [92]

Figure 4.6(a) shows the time interval for Doppler analysis at constant value: $\delta t = \Delta \times T_0$, where T_0=16μs and time delay, Δ = 50. When the motor was moved at larger speeds (v_{motor} = 0.5mm/s, 0.7mm/s and 0.9mm/s) to compress the sample, the displacements

experienced the phase wrapping artifact. Doppler phase shift has magnitude larger than π/2 at time interval δt and could not be precisely estimated using Equation (4.3). Figure 4.6(a) suggests that proper time interval is required for Doppler analysis for motion speed. In a different set of experiments, with benchtop experimental setup shown in Figure 4.4(a), the motor is translated at the same speed (v_{motor} = 0.25mm/s) to compress the sample and displacements are shown in Figure 4.6(b).

Notably, the Doppler phase shift for the displacement tracking was calculated between A-scans with various time intervals: $\delta t = \Delta \times T_0$, where T_0=16μs and Δ=1, 2, 5, 50, 100, 150. In Figure 4.6 (b), for Doppler analysis with a small-time interval ($\delta t = \Delta \times T_0$ with Δ=1, 5, 50), the extracted displacement increases with depth as expected. The random variation of the displacement is larger for a smaller δt and is smaller for a larger δt, which is constant with Equations (4.6) and (4.7), as well as results shown in Figure 4.5. However, additional increment of the time interval ($\delta t = \Delta \times T_0$ with Δ=100, 150) between A-scans for Doppler analysis causes the phase wrapping artifact. Hence, the displacement tends to decrease at a larger depth (blue and black curves in Figure 4.6(b)). From Figure 4.6(b), we can conclude that the axial speed is different at different spatial locations within a deformed sample and different optimal time intervals are necessary for Doppler tracking.

4.5.3 Selection of Adaptive Time Interval

We then explained the real-time estimation of motion speed and the calculation of adaptive time interval for Doppler analysis through HD Doppler phase calculation. With the setup shown in Figure 4.4(a), the sample is compressed by translating the motor at a speed of v_{motor} = 0.1 mm/s. Using one frame of OCT data acquired, HD Doppler phase shift between

adjacent A-scans, mean speed of axial motion at different depths and estimated the optimal time interval ($\delta t(z) = \Delta(z)T_0$) are computed for adaptive Doppler analysis according to Equation (4.9) with W = 4. Integer values of Δ obtained for different depths are shown in Figure 4.7 as the blue curve. On the other hand, for uniform axial deformation and the displacement increases linearly with the depth: $\delta L(z) = \varepsilon z$ with $\varepsilon = \delta L_{\text{motor}}/L_{\text{sample}}$. Here $\delta L_{\text{motor}} = v_{\text{motor}}\delta t$, and the thickness of the sample L_{sample} = 4mm. Therefore, the time required for OCT signal at depth z to achieve a phase shift of $\pi/(2W)$ is:

$$\Delta t = \frac{\lambda_0 L_{sample}}{8W v_{motor} z} \tag{4.12}$$

The depth dependent integer $\Delta(z)$ can be obtained as:

$$\Delta = \left\lfloor \frac{\lambda_0 L_{sample}}{8T_0 W v_{\text{motor}} z} \right\rfloor \tag{4.13}$$

Analytically obtained $\Delta(z)$ is plotted as the red curve in Figure 4.7 and is consistent with the time interval extracted in the real-time software.

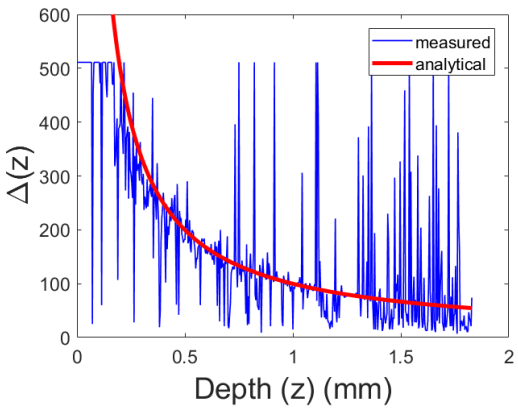

Figure 4.7 Adaptive time interval ($\delta t(z)=\Delta(z)T_0$) selected for a sample under compression. *Source: [92]*

The time interval for Doppler analysis is determined using Equation (4.9) requires a pre-defined parameter W in the software. For Doppler signal free of phase wrapping

artifact, the noise in the estimated Doppler phase is independent of the time interval between signals, as shown in Figure 4.5(b) and (d), as well as Equations (4.6) and (4.7). On the other hand, a smaller value of W in Equation (4.9) implies a larger value of time interval ($\delta t = \Delta \times T_0$) between A-scans for Doppler phase calculation and a larger phase shift due to accumulated displacement. Therefore, a smaller value of W ensures higher SNR in displacement tracking. However, the displacement tracking signal distorts for $W \leq 1$ as the actual phase shift $\left|\frac{\pi}{2W}\right| \geq \frac{\pi}{2}$ cannot be estimated properly using Eq (4.3). To demonstrate the effect of W on motion tracking, we used the experimental setup shown in Figure 4.4(a). We compressed the sample by translating the motor in axial direction with the speed of 0.25mm/s and the displacement of 0.5mm., Time intervals are calculated using Equation (4.9) with different values of W and depth resolved displacements from the compression processes are shown in Figure 4.8. The noise in displacement tracking reduces with the smaller value of W and phase wrapping artifact occurs for W = 1 and 0.5. Therefore, a smaller value of W is ideal to improve the SNR of displacement tracking, but $W > 1$ is preferred to avoid phase wrapping artifact in adaptive Doppler analysis.

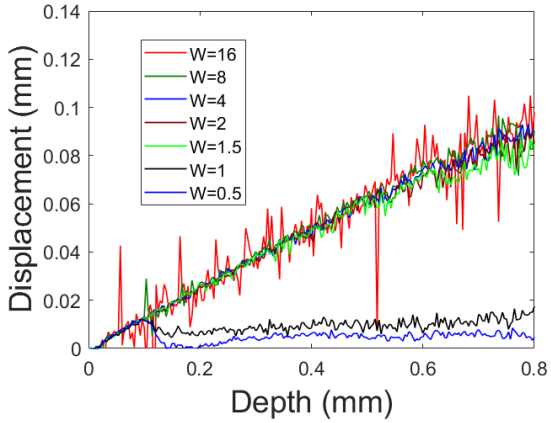

Figure 4.8 Depth resolved displacements obtained through adaptive Doppler analysis when different values of W were used to determine the time interval according to Equation (4.9).
Source: [92]

4.5.4 Depth-Resolved Displacement Tracking for Different Displacements and Speeds

We then demostrated an accurate and robust estimation of displacement tracking through the adaptive Doppler analysis. We compressed the sample by translating the motor at different displacements (δL_{motor} = 0.1mm, 0.2mm, 0.3mm and 0.4mm) with same motor speed (v_{motor} = 0.1mm/s). Figure 4.9(a) shows depth resolved displacements (solid curves) from the real-time software. Time interval was calculated using Equation (4.9) with W = 2. Assuming the uniform axial deformation, the displacement established within the sample increases linearly with the depth: $\delta L(z) = \varepsilon z$, and ε can be obtained: $\varepsilon = \delta L_{motor}/L_{sample}$ (L_{sample} indicates the sample thickness = 4mm) as shown as dashed lines in Figure 4.9(a). Both the experimental and the analytical results are consistent. The result suggests that the adaptive Doppler analysis accurately tracks the magnitude of axial displacement at different depths of the deformed sample.

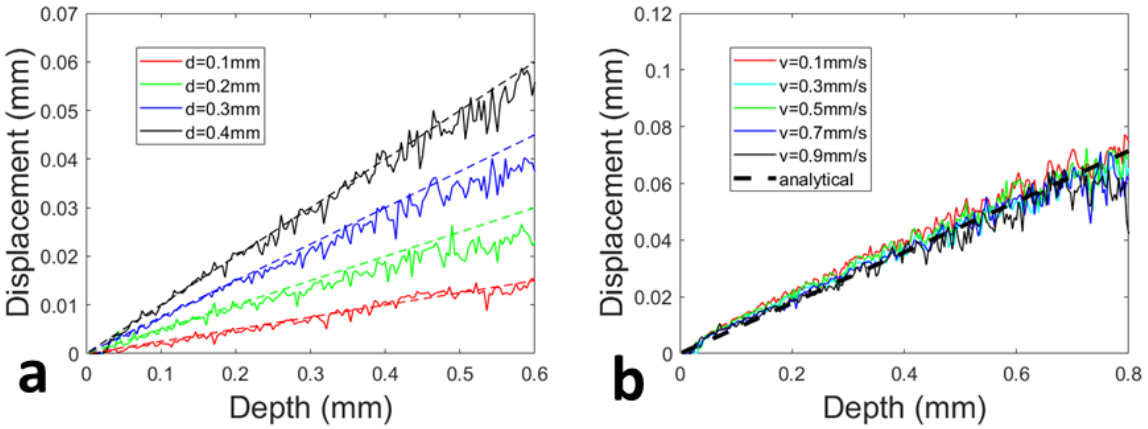

Figure 4.9 Depth resolved displacement extracted through adaptive Doppler analysis, (a) motor translated at the same speed for different displacements; (b) motor translated at different speeds for the same displacement.
Source: [92]

The motor translation speeds (v_{motor} = 0.1mm/s, 0.3mm/s, 0.5mm/s, 0.7mm/s and 0.9mm/s) are also varied with the motor movement of 0.5mm (δL_{motor}= 0.5mm) to

compress the sample. Depth resolved sample displacements through the adaptive Doppler analysis are shown in Figure 4.9(b). Assuming the uniform deformation throughout the sample, displacement is generated ($\delta L(z) = \varepsilon z$ and $\varepsilon = \delta L_{motor}/L_{sample}$) and the result shows linear graph in Figure 4.9(b) as the dashed black line. Despite different motor translation speeds, the signal quality of depth resolved displacements are impressive and are free of phase wrapping artifacts. In contrast, Figure 4.6(a) shows that Doppler analysis based on a fixed time interval are affected by noisy signals in displacement tracking and the phase wrapping artifacts.

4.5.5 OCE Measurement Based on OCE Handheld Probe

Afterwards, we performed OCE measurement with a handheld probe (Figure 4.4(b)). The sample was manually compressed by the probe and OCT signals were acquired. Depth resolved displacements were measured by calculating Doppler phase shift between OCT signal acquired with small ($\delta t = T_0$), large ($\delta t = 100T_0$) and adaptive (Equation (4.9)) time intervals, where T_0 indicates the acquisition time interval in between two consecutive A-scans and T_0 = 16μs. Figure 4.10 shows the displacements at the end of the manual compression. Clearly, for a large time interval ($\delta t = 100T_0$), the displacement does not increase monotonically with depth (blue signal in Figure 4.10), due to the phase wrapping artifact. On the other hand, for small time interval with $\delta t = T_0$ (black signal in Figure 4.10), the displacement is overwhelmed by noises, which is consistent with Equations (4.6) and (4.7). The displacement through adaptive Doppler analysis (red signal in Figure 4.10) is less noisy and is free from phase wrapping artifact. Therefore, adaptive Doppler analysis

is important for a manual probe equipment to perform OCE characterization as hand movement unavoidably varies the compression speed.

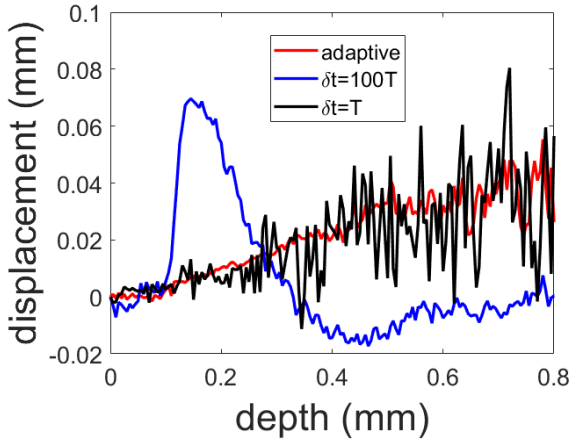

Figure 4.10 Depth resolved displacement extracted from manual compression process with adaptive (red), large (blue) and small (black) time intervals between Ascans invovled in Doppler analysis.
Source: [92]

Additionally, we verified that manual OCE characterization through adaptive Doppler analysis could reveal the spatial variation of mechanical properties. We used two samples. Sample 1 is a homogeneous PDMS phantom and Sample 2 is a homogeneous PDMS with multiple tap-layers attached on top. We compressed both samples manually with the handheld probe and performed the real-time adaptive Doppler on OCT signals to attain the displacements from Sample 1 (blue signal in Figure 4.11(a)) and Sample 2 (blue signal Figure 4.11(b)). We also observed the magnitude OCT signals (red signals) from Sample 1 and Sample 2 as shown in Figure 4.11(a) and (b), respectively. Sample 1 was optically and mechanically homogeneous. Therefore, for Sample 1, A-scan (red signal in Figure 4.11(a)) declines with depth due to the absorption and scattering of light and the depth resolved displacement (blue signal in Figure 4.11(a)) increases mononically with depth. In comparison, the OCT magnitude of Sample 2 shows the tape layers (red signal

upto around 0.36mm depth in Figure 4.11(b)). The tape-layers of Sample 2 did not deform under compression and the displacement of Sample 2 (blue signal in Figure 4.11(b)) remains approximately the same until it reaches the boundary between the tape layers and PDMS phantom. Figure 4.11 suggests that even though the motion of the sample created by manual compression varies with time and spatial location, the adaptive Doppler analysis is capable of differentiating the mechanical properties of different materials..

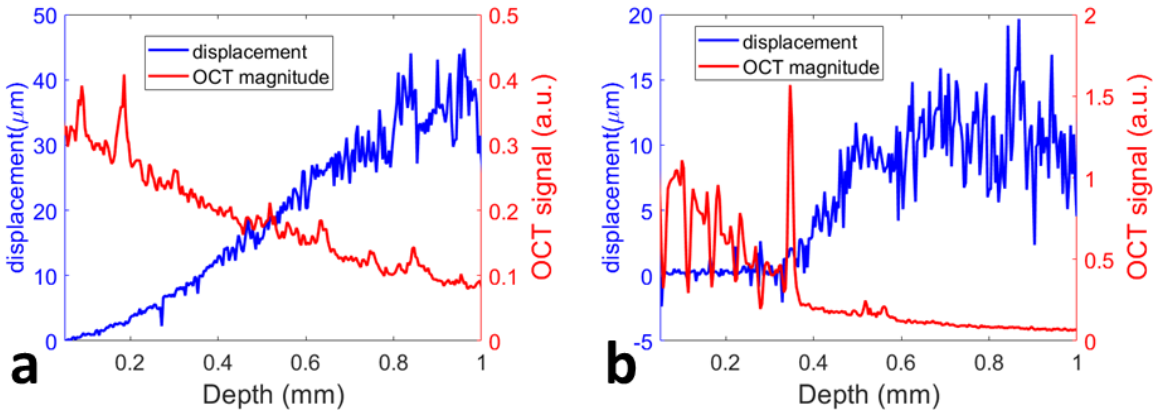

Figure 4.11 (a) Displacements (blue) obtained from adaptive Doppler tracking and magnitude OCT signal (red) of Sample 1; (b) displacements (blue) obtained from adaptive Doppler tracking and magnitude OCT signal (red) of Sample 2.
Source: [92]

4.5.6 *in vivo* Tissue Characterization by Adaptive Doppler

We used the handheld probe to compress the skin tissue of a volunteer to demonstrate *in vivo* OCE tissue characterization by adaptive Doppler. Figure 4.12(a) shows the skin region with a wart at the dorsal of the hand whe it is compressed by the probe. The displacement extracted through adaptive Doppler analysis is shown in Figure 4.12(c) as the blue curve. B-scan image of neighboring region of healthy skin during compression and the displacement are shown as Figure 4.12(b)) and as the red curve in Figure 4.12(c), respectively. Figure 4.12(c) shows different strain characteristics in for healthy and diseased skin. The diseased skin has heterogeneous properties. Therefore, the displacement

shows different slopes (red arrow indicates the starting of displacement for another slope) indicating different axial strain within different depth range. However, the displacement of the healthy skin increases approximataly with the same slope. Assumming the uniform distributed stress, results of Figure 4.12(c) indicate that the elasticity of the diseased skin varies as depth and the healthy skin shows homogeneous elasticity within the depth range.

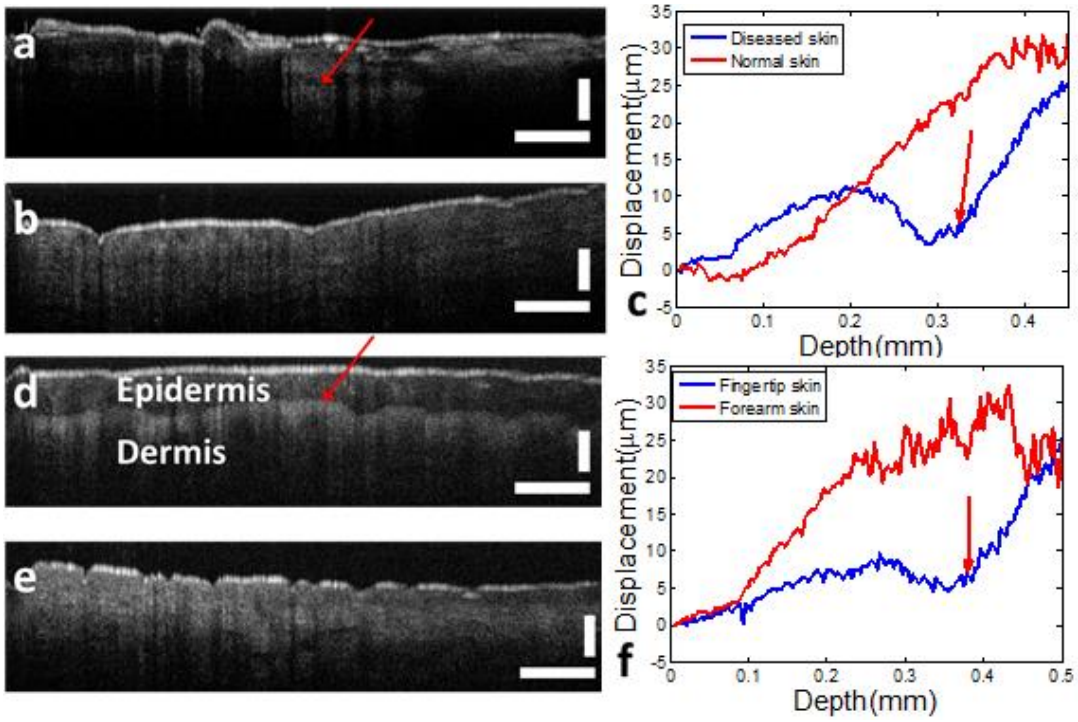

Figure 4.12 (a) *in vivo* OCT image of diseased skin at the dorsal of the hand; (b) *in vivo* OCT image of normal skin at the dorsal of the hand; (c) displacement measured through adaptive Doppler analysis of OCT signal for diseased skin and normal skin; (d) *in vivo* OCT image of fingertip skin; (e) *in vivo* OCT image of forearm skin; (f) displacement measured through adaptive Doppler analysis of OCT signal for fingertip skin and forearm skin. Scale bars represent 500μm.
Source: [92]

The same experiment is also performed on the fingertip (Figure 4.12(d)) and the forearm (Figure 4.12(e)) skin of the same subject. Displacements through manual compression and adaptive Doppler analysis is shown in Figure 4.12(f). The displacement from compressed fingertip skin shows different slopes within different depth regions due to the thickness

variation of epidermis and dermis layers. The dermal-epidermal junction in fingertip skin is visible as marked by red arrow in Figure 4.12(d). A larger slope is detected within the layer of epidermis, and a smaller slope is noticed within the layer of dermis. The result suggests that in epidermis has larger strain compared to the dermis region. Assuming the uniform spatial stress distribution of stress, results in Figure 4.12(f) suggest a smaller stiffness of epidermis compared to dermis, which is consistent with experimental results stated by Kennedy et. al in [109].

4.6 Conclusion and Discussion

In summary, we developed and validated a Doppler analysis method that is adaptive to time and spatial location, for robust manual OCE characterization based on a handheld instrument. Real-time tissue mechanical characterization was demonstrated for the first time to the best of our knowledge, enabled by this adaptive Doppler tracking strategy.

Moreover, our adaptive Doppler tracking method can measure the smallest and largest axial motion with high accuracy. The smallest measurable displacement is determined by the noise floor of phase estimation. According to Equations (4.6) and (4.7), the mean velocity extracted by the adaptive analysis algorithm is: $\bar{v} = \frac{\lambda_0}{4\pi\Delta_{k,m}T_0}\sqrt{\frac{\beta}{SNR}}$. The minimal measurable velocity is found when $\Delta_{k,m}$ has the largest value ($\Delta_{k,m}=M_0/2$). Hence, $\bar{v}_{min} = \frac{\lambda_0}{2\pi M_0 T_0}\sqrt{\frac{\beta}{SNR}}$. On the other hand, $\Delta_{k,m}$ takes a smaller value for a larger motion speed, and the largest measurable displacement is determined by the phase wrapping phenomenon. When the displacement is calculated with $\Delta_{k,m}=1$ without phase wrapping

($|\delta\hat{\phi}_{k,m}|<\pi/2$), $\bar{v}_{max} = \frac{\lambda_0}{8T_0}$. The dynamic range (DR= $\frac{\bar{v}_{max}}{\bar{v}_{min}}$) in tracking motion (axial speed) is thus $DR = \sqrt{\frac{SNR}{\beta}}\frac{\pi(M_0/2)}{2}$. Compared to non-adaptive Doppler tracking (DR= $\sqrt{\frac{SNR}{\beta}}\frac{\pi}{2}$), the adaptive Doppler analysis achieves a $M_0/2$ fold improvement in the dynamic range for motion tracking, where M_0 is the number of A-scans in a frame of OCT data acquired.

CHAPTER 5

NOISE ADAPTIVE WAVELET THRESHOLDING FOR SPECKLE NOISE REMOVAL IN OPTICAL COHERENCE TOMOGRAPHY

5.1 Introduction

OCT is based on coherence detection of interferometric signals and hence inevitably suffers from speckle noise. To remove speckle noise in OCT images, wavelet domain thresholding has demonstrated significant advantages in suppressing noise magnitude while preserving image sharpness. However, speckle noise in OCT images has different characteristics in different spatial scales, which has not been considered in previous applications of wavelet domain thresholding. This chapter describes the implementation and the performance analysis of the noise adaptive wavelet thresholding (NAWT) algorithm.

5.2 Research Motivation for NAWT Algorithm

OCT is a high-speed, high resolution, 3D imaging technique based on low coherence light interferometry [16]. OCT inevitably affects by random noises particularly the multiplicative speckle noise [117 – 119]. Speckle noise in OCT image arbitrarily modifies the OCT amplitude and obscures the subtle image features, resulting in compromised effectiveness in its clinical applications [21, 25]. Various hardware and software-based approaches are developed to remove the speckle noise. Hardware techniques for speckle noise reduction, such as spatial compounding and spectral compounding, may achieve high

SNR for OCT images. However, these techniques have high system cost, provides low spatial resolution and reduces the imaging speed [11, 120, 121]. Post-processing algorithms have also been developed to reduce the speckle noise in OCT images [122, 123]. As speckle noise is inherently multiplicative rather than additive, conventional linear filtering in spatial or frequency domain is suboptimal. This is because, conventional linear filtering produces significant blurring and reduces image contrast after postprocessing [124]. Nonlinear wavelet thresholding methods can be also used, as an alternative, to suppress the speckle noise in various imaging modalities such as ultrasound imaging, synthetic aperture imaging and OCT [17, 125, 126]. Wavelet thresholding algorithms have shown excellent capability in reducing speckle noise and preserving image sharpness in previous studies [127, 128]. The principle of wavelet thresholding is simple. After the wavelet transform, the magnitude of wavelet coefficients is used as an oracle to determine if a coefficient is noise or signal. A wavelet coefficient with larger amplitude carries important information while a wavelet coefficient with smaller amplitude is noisy component.

In conventional wavelet domain OCT thresholding technique, an adaptive threshold is estimated for each wavelet sub-band through an estimated signal variance for the particular sub-band. Assuming the same noise in different sub-bands, the same magnitude of noise variance is calculated for all sub-bands. However, the de-correlation of OCT signals with fully developed speckle could be modeled as a Gaussian function and Gaussian power spectral density can be considered for speckle noise [129]. Therefore, the speckle OCT image has different magnitudes in different wavelet sub-bands. Moreover, the speckle noise characteristics largely depends on the imaging system rather than the sample. Hence,

the characteristics of speckle noise can be extracted from structureless homogeneous scattering sample through OCT imaging.

We developed a novel algorithm for OCT speckle noise removal and then captured and evaluated an OCT image of a homogeneous scattering sample. Afterwards, we computed the noise variance (σ_{w2}) in each wavelet sub-band and used σ_{w2} to estimate the optimal threshold for each sub-band. The main steps of NAWT are: wavelet decomposition, soft thresholding and wavelet reconstruction. All these steps can be parallelized using GPU. Therefore, the NAWT algorithm can be implemented in GPU for real-time speckle noise removal.

5.3 Principle of NAWT Algorithm

In conventional wavelet thresholding method, a wavelet transform is performed on a spatial domain image as shown in Figure 5.1. Subsequently, a threshold (T) is calculated according to Equation (5.1) for each sub-band of detail coefficients (H_1, V_1, D_1, H_2, V_2, D_2, H_3, V_3, D_3, …), where H_k denotes detail coefficients in horizontal direction at kth wavelet decomposition level; V_k indicates detail coefficients in vertical direction at kth wavelet decomposition level, and D_k indicates detail coefficients in diagonal direction at kth wavelet decomposition level.

$$T(\sigma_X) = \frac{\sigma^2}{\sigma_X} \tag{5.1}$$

Here, σ^2 is the noise variance and σ_x is the standard derivation of noise-free signal.

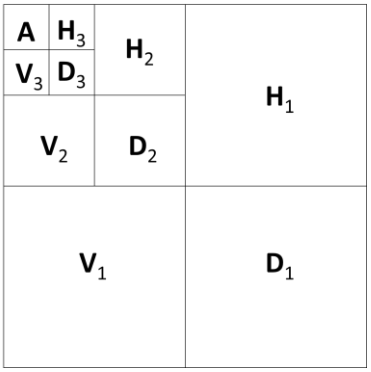

Figure 5.1 2D wavelet decomposition of an image

Afterwards, according to Equation (5.2), a soft thresholding is applied to each wavelet coefficient *S*. Spatial domain image with suppressed speckle noise is then generated through inverse wavelet transform.

$$S_T = \begin{cases} 0; & |S| \leq T \\ sgn(S)\,[|S| - T]; & |S| > T \end{cases} \tag{5.2}$$

Noise variance (σ^2) of Equation (5.1) is computed through the detail sub-band H_1 with the median estimator as shown in Equation (5.3).

$$\sigma = \frac{\text{Median}(|S_{ij}|)}{0.6745}, \quad S_{ij} \in \text{subband } H_1 \tag{5.3}$$

The standard derivation of the noise free signal in (σ_x) each wavelet sub-band is measured according to Equation (5.4),

$$\sigma_X = \sqrt{max(\sigma_S^2 - \sigma^2, 0)} \tag{5.4}$$

Here, σ_s^2 is the variance of the measured wavelet coefficients.

The close form threshold formulated in Equation (5.1) provides the optimal noise reduction in OCT images. All the wavelet coefficients of OCT image follow a generalized Gaussian distribution (GGD). Equations (5.1) – (5.4) summarize the conventional adaptive wavelet thresholding technique of image denoising, mentioned by S. G. Change *et al.* in [127]. However, the assumption of same noise variance (σ^2) across all the sub-bands in

wavelet domain is not effective for OCT signal. This is because the speckle in OCT signal has different characteristics in different sub-bands. Therefore, a noise adaptive wavelet thresholding (NAWT) algorithm has been developed to consider different speckle noise pattern at different spatial scale to accomplish better noise reduction.

The major modification between NAWT algorithm and the conventional wavelet domain thresholding algorithm is that NAWT uses different noise variance to estimate the threshold for individual sub-band. Equation (5.5) is used to compute the threshold, where σ_w^2 indicates the noise variance for the sub-band W (W will be all different sub-bands: H_1, V_1, D_1, H_2, V_2, D_2, H_3, V_3, D_3, …). For each sub-band, σ_w^2 is computed for OCT image of a structureless homogeneous sample. The image is modulated by fully developed speckle. Afterwards, wavelet domain speckle statistics obtained from the structureless sample are applied to other images. It is worth mentioning that speckle in OCT image mainly depends on the characteristics of the imaging system rather than the sample. In other words, the NAWT algorithm applies the noise variance at different sub-band of wavelet coefficients as a prior for subsequent noise reduction.

$$T_N(\sigma_X) = \frac{\sigma_W^2}{\sigma_X} \tag{5.5}$$

As the magnitude variation of a reference image has random noise, this reference image from a uniform scattering sample allows the characterization of speckle noises. Moreover, it is not possible to evaluate speckle noise characteristics from OCT image of a spatially heterogeneous sample because the OCT magnitude image for heterogeneous structured sample varies due to random noise and deterministic structural features of the sample.

The flow-chart for the NAWT algorithm is shown in Figure 5.2.

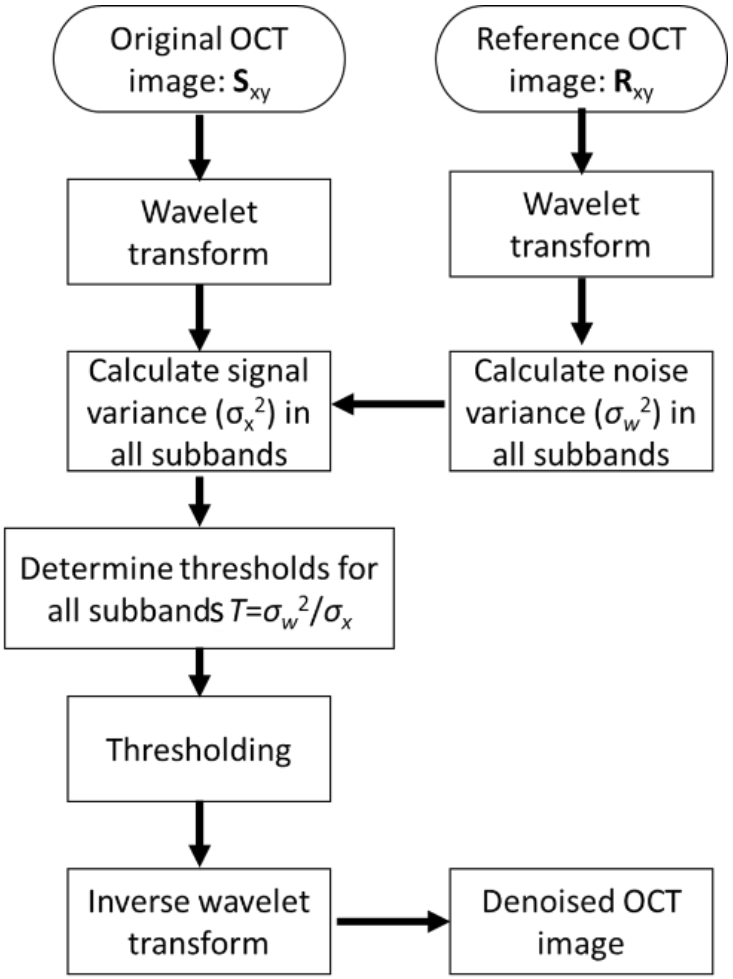

Figure 5.2 Signal processing flow-chart for the optimized adaptive wavelet thresholding algorithm.
Source: [18]

Briefly, σ_{w2} for each sub-band (H_1, V_1, D_1, H_2, V_2, D_2, H_3, V_3, D_3, …) are calculated from the structureless reference image ($\mathbf{R}_{xy}$) that is obtained from the homogeneous scattering sample. Afterwards, the image to be denoised ($\mathbf{S}_{xy}$) is used to estimate the signal variance (Equation (5.4)). The threshold for each sub-band is thus estimated using Equation (5.5). Notably, $\mathbf{R}_{xy}$ and $\mathbf{S}_{xy}$ are normalized by their mean signal intensities respectively. Every wavelet coefficient (S) in a detail sub-band is then performed thresholding using Equation (5.2). Spatial domain image is then reconstructed by the inverse wavelet

transform. The algorithm is implemented in MATLAB 2016 on a personal computer (intel i72.8 GHz CPU, 8GB memory). The processing time of a 512x2014 image is approximately 0.2s.

5.4 Description of an OCT Imaging System

A spectral domain OCT (SD OCT) system has been utilized for the imaging experiments as shown in Figure 5.3. The detail imaging setup is described in chapter 2. Briefly, SD-OCT system has a superluminescent diode (SLD1325 Thorlabs, 1.3μm central wavelength and 100nm bandwidth, power less than 10mW at the sample) as the broadband light source. The output of the SLD illuminates the reference and sample arm of a fiber-optic Michelson interferometer through a fiber-optic coupler. A lens is used in the sample arm to focus the probing beam and to collect the photons backscattered from the sample. Light returned from the sample and the reference mirror experienced the interference and is then detected by a CMOS camera and A frame grabber streams the signal from the camera to the host computer for further processing in real-time GPU.

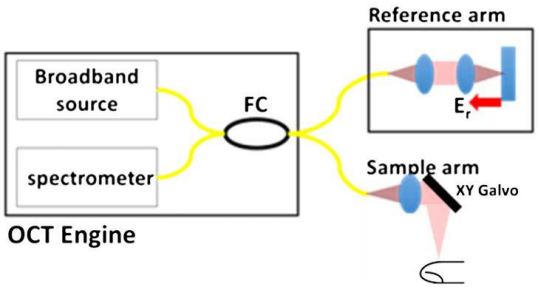

Figure 5.3 Schematic of SD-OCT imaging system. Here, FC = fiber-coupler.
Source: [18]

5.5 Experimental Results

5.5.1 Assessment of Speckle Noise Characteristics of OCT in Wavelet Domain

Firstly, the characteristics of speckle noise of OCT image is evaluated in the wavelet domain. A homogeneous scattering PDMS sample is used. Four structureless images (one of the images is shown in Figure 5.4) are obtained from the same PDMS sample with different elevation planes (B-scan 1, B-scan 2, B-scan 3 and B-scan 4) of 31.4μm interval.

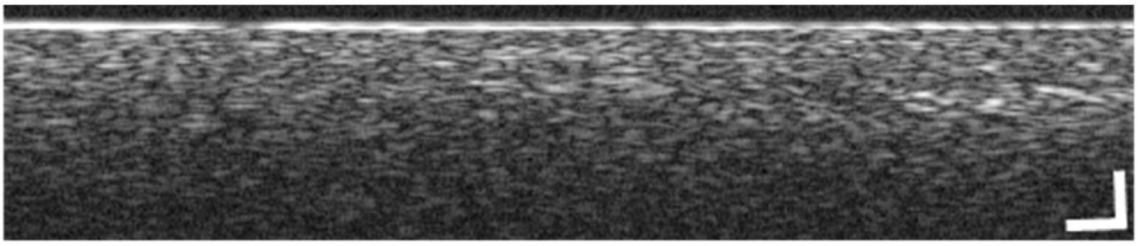

Figure 5.4 OCT B-scan of scattering PDMS phantom. Scale bars indicate 200μm.
Source: [18]

All the B-scan images (linear scale) are normalized by their respective mean values and the probability density signal magnitudes (for depth from 0.8mm to 1.15mm) are computed as shown in Figure 5.5 (solid curves). The probability density function (PDF) of Rayleigh distribution with a mean of 1 according to Equation (5.6) is also plotted as the dashed curve in Figure 5.5:

$$P(s)=\frac{s}{\sigma^2} exp\left(-\frac{s^2}{2\sigma^2}\right) \text{ where } \sigma=\sqrt{\frac{2}{\pi}} \tag{5.6}$$

Notably, all the probability density signal magnitudes images acquired from four B-scan sample images followed the same Rayleigh distribution pattern, even if they had different sub-resolution characteristics. This result suggests that the speckle statistics of OCT image is determined by the imaging system rather than the sample properties.

Therefore, speckle statistics characterized by a reference image can be applied as a prior for subsequent noise reduction.

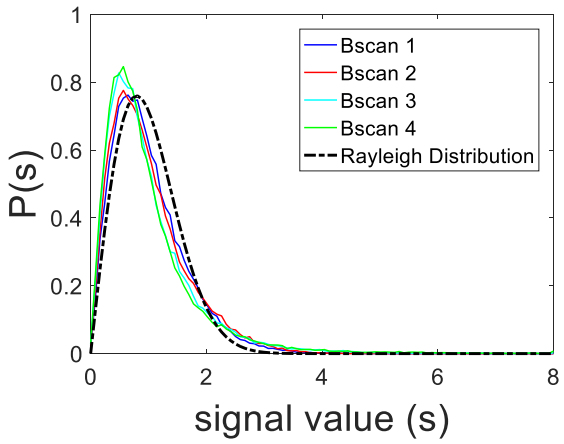

Figure 5.5 Probability distribution of OCT signal magnitude (solid curves), in comparison with the PDF of Rayleigh distribution (dashed).
Source: [18]

Next, one of the B-scan images (linear scale, normalized to its maximum value) from PDMS sample is used to demonstrate that the magnitude of speckle noise varies significantly in different wavelet sub-band. The image is transformed into a four-level wavelet using a sym4 wavelet base. The variation of signal is simply due to noise. Next, the variance of wavelet coefficients in horizontal (H), vertical (V) and diagonal (D) directions are computed in four different decomposition levels and the results are shown in Figure 5.6. The noise magnitudes measured by wavelet coefficient variance are different in each different sub-bands. However, the conventional methodology, assuming same noise variance (σ^2) across different wavelet sub-bands, computed the threshold for wavelet domain de-noising according to Equation (5.1). As Figure 5.6 shows large difference for noise magnitude in different sub-bands and soft-thresholding based on Equation (5.1) is not the optimal solution to reduce the speckle noise in OCT image.

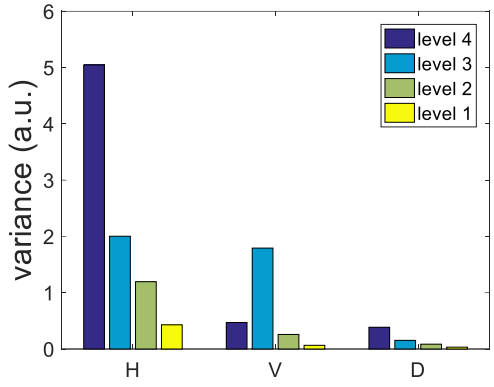

Figure 5.6 Variance of wavelet coefficients for B-scan image obtained from the homogeneous scattering sample, in H, V, and D directions at four decomposition levels. Clearly, the magnitudes of noise quantified by wavelet coefficient variance are different in different sub-bands.
Source: [18]

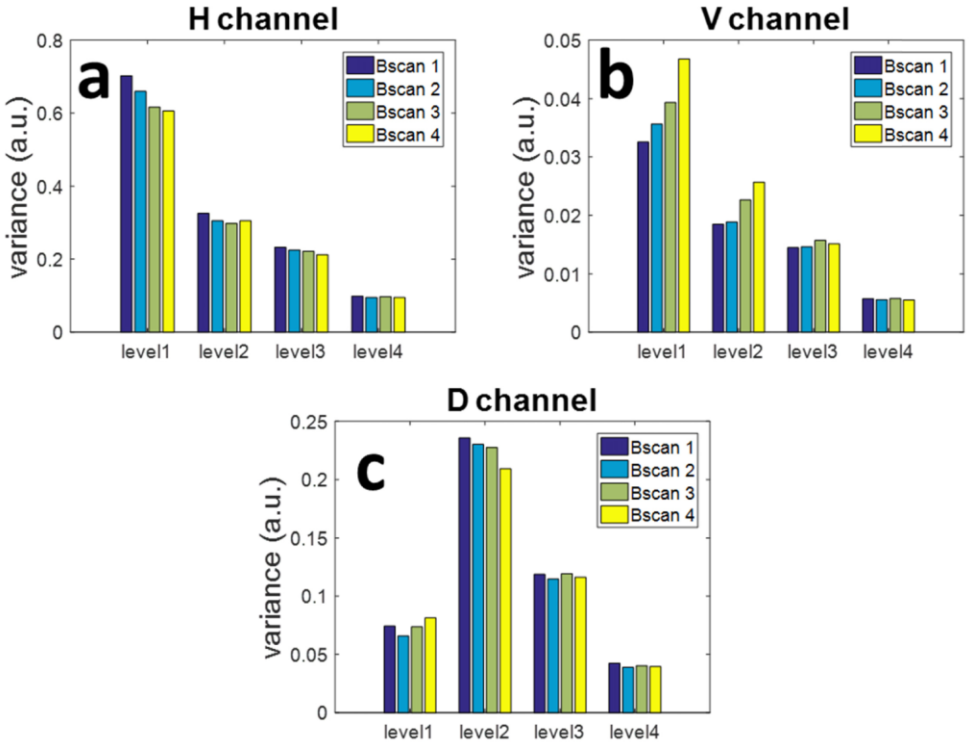

Figure 5.7 Variance of wavelet coefficients for B-scan image obtained from the homogeneous scattering sample in four different elevation planes (B-scan 1, B-scan 2, B-scan 3, and B-scan 4), in H, V, and D directions at four decomposition levels.
Source: [18]

Speckle statistics is further characterized by a reference image The inter-image difference for noise variance are compared for the reference image. Images (linear,

normalized) captured from the homogeneous PDMS sample is used to generate results as shown in Figure 5.7. For the same wavelet sub-band (H, V or D , level 1 - 4), noise variance difference among different B-scan images (B-scan1- B-scan 4) are lower, compared to the difference among different wavelet sub-bands for the same image.

To demonstrate the efficiency of our algorithm, the NAWT algorithm is applied on a sample (Sample 1). Sample 1 is fabricated by attaching three tape-layers top of the homogeneous scattering PDMS phantom. The sample has well developed speckle pattern and all the three tape-layers are easily visible. Therefore, this sample is suitable for the validation of the NAWT algorithm. OCT image without any post-processing is shown in Figure 5.8 (a). The area within the rectangle is enlarged in Figure 5.8 (b) to provide better visualization of image details. The grainy appears in the image due to speckle noise. NAWT algorithm is applied to the PDMS sample and denoised image is obtained as shown in Figure 5.8 (c). Clearly, speckle noise in Figure 5.8(c) and (d) in reduced in compared to Figure 5.8(a) and (b). Moreover, the sample boundaries are clearly visible in Figure 5.8(c) and (d). Furthermore, Figure 5.8(a) is also processed through the conventional wavelet domain thresholding algorithm. The processing results are shown in Figure 5.8(e) and (f). The image texture remains grainy after denoising by conventional wavelet technique in contrast Figure 5.8 (c) and (d) for NAWT processing.

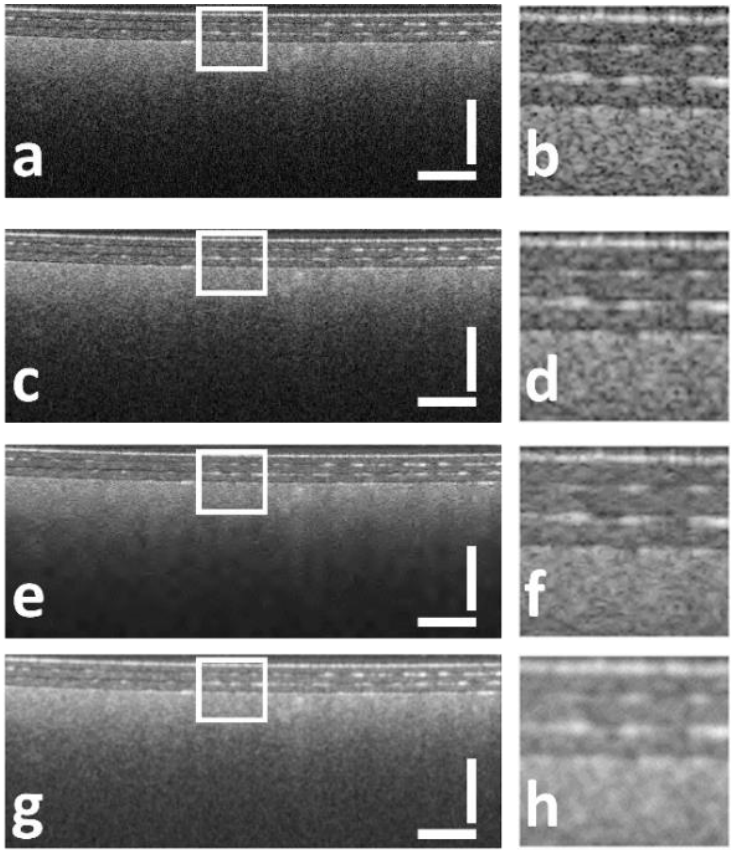

Figure 5.8 (a) Raw OCT image of Sample 1 (without any post processing); (b) enlarger region of interest (ROI) enclosed by the rectangle in Figure 5.8 (a); (c) OCT image of Sample 1 processed by our NAWT algorithm; (d) enlarger ROI enclosed by the rectangle in Figure 5.8(c); (e) OCT image of Sample 1 processed by conventional wavelet domain thresholding; (f) enlarger ROI enclosed by the rectangle in Figure 5.8 (e); (g) OCT image of Sample 1 processed by Gaussian filtering; (h) enlarger ROI enclosed by the rectangle in Figure 5.8 (g). Scale bars in Figure 5.8 (a) indicate 500 μm.
Source: [18]

Next, spatial domain linear filtering is achieved through a Gaussian kernel (25 pixels by 25 pixels with a σ of 1.5 pixels:

$$h(i,j)=\exp\left[-(i^2+j^2)/2\sigma^2\right]) \quad (5.7)$$

Figure 5.8(g) and (h) represent the processed OCT images by Gaussian filter. Gaussian filter effectively removed the speckle noise. However, the filter also reduced the contrast of the image and blurred small features in the image.

5.5.2 A-scan Signals of OCT Images for Different Algorithms

Additionally, we selected the OCT A-scans at the same lateral location for different algorithms to illustrate the effectiveness of NAWT algorithm in speckle noise reduction. The processed A-scans data of different algorithms are plotted in Figure 5.9. OCT data without any processing (red curve) has shown random fluctuation due to the presence of speckle noise. The green curve of conventional wavelet thresholding has reduced the variation of noise. The noise reduces more for NAWT as shown by blue curve in Figure 5.9. The result suggests the higher performance for speckle noise suppression by NAWT in contrast to conventional wavelet domain thresholding.

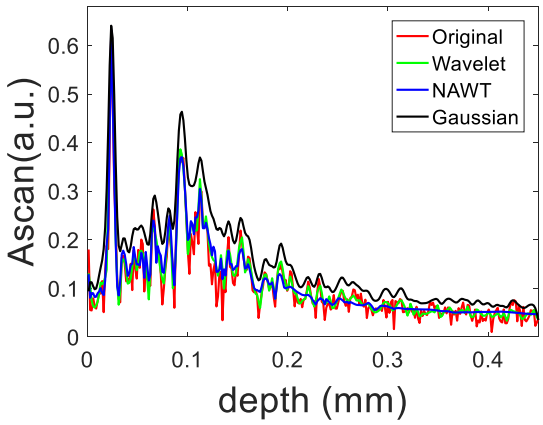

Figure 5.9 A-scans at the same lateral location from OCT images processed with different algorithms.
Source: [18]

However, the A-scan signal processed by the Gaussian filter (black curve) broadened the signal peaks. This result is consistent with the visual appearance in Figure 5.8(e) and (g) where Gaussian filtering blurs small structural features and reduces the image contrast. Notably, Gaussian filter decreases the random signal fluctuation up to a certain level but the Gaussian filter also introduces the noise level artificially after depth >

0.3mm. Therefore, it is worth mentioning that linear Gaussian filter is not optimized for the reduction of multiplicative speckle noise.

5.5.3 Image Enhancement of B-scan OCT Images using NAWT Algorithm

Next, NAWT algorithm is applied to two samples: an IR viewing card (Sample 2) and human fingertip (Sample 3). B-scan OCT images are obtained from for both samples without and with NAWT processing. The images are shown in Figure 5.10 (a) – (d). NAWT algorithm significantly reduced the grainy appearance of the image due to speckle noise for Figure 5.10 (b). Additionally, the upper and lower boundaries of the plastic film are not blurred. In Figure 5.10 (d), the image processed by NAWT clearly shows the epidermis-dermis junction.

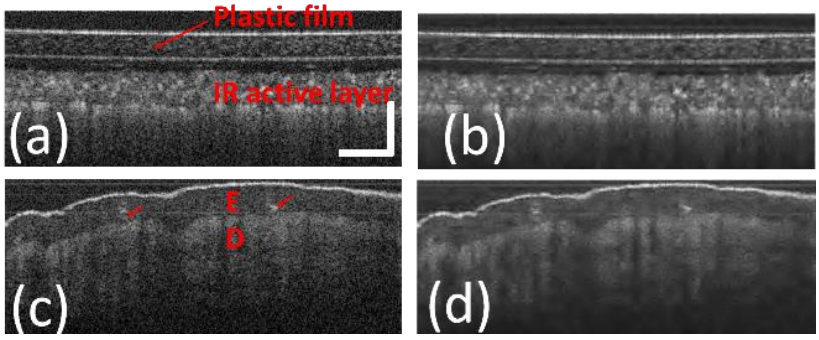

Figure 5.10 (a) Original IR card image (Sample 2), (b) IR card image processed using NAWT; (c) fingertip image (Sample 3), (d) fingertip image processed using NAWT. Scale bars indicates 500 μm. E: epidermis; D dermis; arrows in Figure 5.10 (c) indicate sweat duct.
Source: [18]

5.5.4 Performance Analysis of NAWT Algorithm

SNR of the OCT images are estimated according to Equation (5.8) to quantitatively assess the effectiveness of different speckle removal algorithms. Remarkably, in SNR calculation, background OCT data within the depths from 1mm-1.5mm are considered for the estimation of noise variance. Additionally, β (Equation (5.9)) is calculated to evaluate the

noise removal capability of NAWT to restore the morphological features [130] of the original image.

$$SNR = 10\,log_{10}\left(\frac{[mean(I)]^2}{\sigma_I^2}\right) \tag{5.8}$$

$$\beta = \frac{\Gamma(I_D - \mu_{I_D}, I_0 - \mu_{I_0})}{\sqrt{\Gamma(I_D - \mu_{I_D}, I_D - \mu_{I_D}) \cdot \Gamma(I_0 - \mu_{I_0}, I_0 - \mu_{I_0})}} \tag{5.9}$$

where σ_I^2 indicates noise variance of the OCT image, I_D represents the denoised image; I_0 indicates the original image; μ_D is the mean signal value of the denoised image; μ_0 indicates the mean signal value of the original image; $\Gamma(I_1, I_2) = \sum_{i,j}[I_1(i,j)I_2(i,j)]$ where i and j indicate indices of pixel in 2D images.

In Table 5.1, we summarized performance evaluation of different speckle reduction algorithms (WT: conventional wavelet domain thresholding; NAWT: noise adaptive wavelet thresholding; GF: Gaussian filtering). OCT images are obtained from Sample1 (Figure 5.8), Sample2 (Figure 5.10 (a) and (b)) and Sample3 (Figure 5.10 (c) and (d)). As shown in Table 5.1, NAWT algorithm offers around 3 -8 dB SNR improvement compared to other methods. Moreover, NAWT has comparable effectiveness in preserving image sharpness (β value) compared to conventional wavelet domain thresholding.

Table 5.1 Performance of Different Noise Reduction algorithms.

Parameters	Methods	Sample 1	Sample 2	Sample 3
SNR (dB)	Raw	17.13	11.42	13.56
	WT	23.17	13.24	17.99
	NAWT	**29.04**	**14.56**	**20.59**
	GF	25.04	14.07	18.99
β	WT	0.96	**0.96**	**0.94**
	NAWT	**0.97**	0.94	0.93
	GF	0.92	0.92	0.90

Source: [18]

Moreover, we compared the speckle noise reduction capability of nonlinear NAWT algorithm to linear Gaussian filtering. We varied the standard deviation (σ) of the Gaussian kernel and calculated the SNR of image at different values of σ. The SNR versus σ curves for Sample 1, 2, and 3 are plotted in Figure 5.11. The three solid curves (black, red and blue) are from Gaussian filtering of the samples and the dashed curves are from SNR obtained from images processed by NAWT. As shown in Figure 5.11, the SNR of OCT image increases with Gaussian filter width for small σ. However, no significant SNR improvement is noticed after certain increment of σ of Gaussian filter. Also, the maximum SNR achieved through Gaussian filtering is lower compared to that of NAWT. The graph suggests that the nonlinear NAWT algorithm is more suitable for the suppression of multiplicative speckle noise.

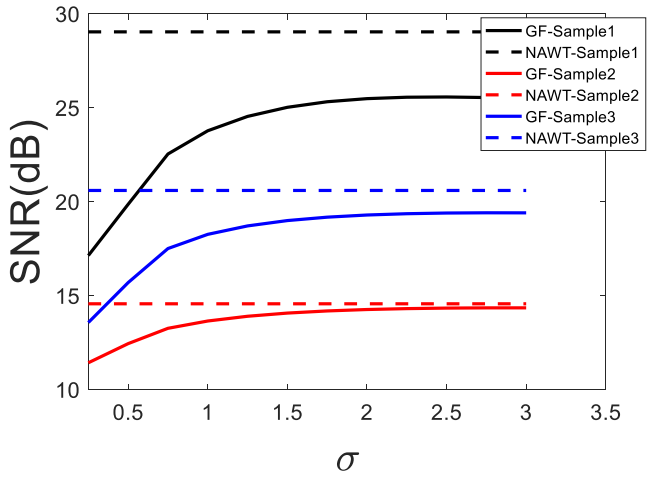

Figure 5.11 SNR performance of Gaussian filtering and NAWT.
Source: [18]

5.6 Conclusion and Discussion

This chapter developed a novel algorithm to remove the speckle noise in OCT images. The noise adaptive wavelet thresholding (NAWT) algorithm utilized the characteristics of

speckle noise in wavelet domain to adaptively remove speckle noise and also conserves the structure features in OCT image. NAWT improves visual appearance of OCT image. Moreover, NAWT shows better performance in noise removal by SNR and in preserving structural features compared to the conventional wavelet domain thresholding and Gaussian filtering.

NAWT can be a generic algorithm for speckle noise removal in various imaging/sensing technologies, such as ultrasound imaging, synthetic aperture imaging, Lidar, etc. NAWT can significantly improve the image quality through reducing the speckle noise as long as fully developed speckle assumption is valid. NAWT algorithm does not require huge computational power and the algorithm takes approximately 0.2s to process a 512x1024 image using CPU in MATLAB environment.

CHAPTER 6

ASSESSMENT AND REMOVAL OF ADDITIVE NOISE IN A COMPLEX OCT SIGNAL BASED ON DOPPLER ANALYSIS

6.1 Introduction

This chapter represents and validates a novel approach to assess and remove the additive noise for optical coherence tomography (OCT) imaging. The method first generates a map of additive noise for the OCT image through Doppler variation analysis. Then, the additive noise is removed from the real and imaginary parts of the complex OCT signal through pixelwise Wiener filtering. Results show that the denoising method improves the sensitivity of OCT imaging and preserves the spatial resolution without any further medication of the imaging apparatus and data acquisition protocol.

6.2 Research Motivation for Doppler Analysis based Additive Noise Reduction in OCT Images

The tissue characterization capability of OCT depends on the sensitivity of OCT. In OCT, sensitivity is defined as the minimal reflectivity attained from the sample arm to generate a noticeable signal from a noisy measurement condition [131, 132]. During the suboptimal measurement condition, high imaging sensitivity is necessary for *in vivo* OCT imaging and the imaging from deep tissues. Noise suppression improves the sensitivity in OCT imaging. There is hardware optimization technique and also various post-processing algorithms such as wavelet domain adaptive filtering, diffusion filtering, and sparsity-based iterative optimization [36, 133 - 135] for removing the noise from OCT signal. In this chapter, a

novel scheme has been developed that performed Doppler variation analysis to assess the additive noise in an OCT signal. Afterwards, it removed the additive noise from the complex OCT signal through an adaptive Wiener filtering algorithm.

The method developed in this chapter differs from the conventional OCT denoising algorithms in the following manners. Firstly, conventional structural OCT imaging system operates on the magnitude of the OCT signal, whereas our method gathers information for both the magnitude and phase from the complex OCT signal. The phase of the OCT signal is normally used for tracking the motion through Doppler analysis and has numerous applications, such as, vasculature visualization, measurement of blood flow, optical coherence elastography and cellular motion detection [56, 74, 136 - 139]. Additionally, OCT phase signal is also applicable for morphological tissue characterization because OCT phase signal is measured by the sample thickness and refractive index [140, 141]. Doppler phase variation can also evaluate the additive noise in the OCT signal for subsequent noise removal. Secondly, most of the conventional denoising algorithms, applied to the OCT magnitude signal, considered noise in OCT image as additive Gaussian [36, 133 –135]. However, OCT imaging suffers from both additive noise and multiplicative noise (speckle noise) [18, 21, 142]. Therefore, for low SNR, modeling with the additive Gaussian noise is not valid for the OCT magnitude. In our denoising method, first, Doppler variation analysis is employed to map an additive noise in the OCT system and then local Wiener filtering [143, 144] is performed for denoising. Similar to the complex denoising algorithm developed for magnetic resonance imaging, the real and imaginary parts of the complex OCT signal are processed as independent signal channels [145, 146]. Sensitivity of OCT imaging can be enhanced by reducing the additive noise from the OCT signal.

6.3 Principle of Doppler Analysis based Additive Noise Reduction Method

Consider a complex OCT signal **F** = F(x, z) (here, x indicates the lateral dimension, z indicates the axial dimension, and the elevation dimension y is not considered) that can be expressed as Equation (6.1). All the bold symbols in Equation (6.1) and subsequent discussions represent a function of space as follows:

$$\begin{aligned} \boldsymbol{F} &= \boldsymbol{N}_m \boldsymbol{R}_0 \boldsymbol{S}_0 e^{j\boldsymbol{\phi}} + \boldsymbol{N}_{\mathrm{Re}} + j\boldsymbol{N}_{\mathrm{Im}} \\ &= \boldsymbol{F}_{\mathrm{Re}} + j\boldsymbol{F}_{\mathrm{Im}} \end{aligned} \tag{6.1}$$

where j is the imaginary unit; R_0 is the reference arm field reflectivity; S_0 and ϕ_0 are the magnitude and phase of sample arm optical field (x, y, z); $N_m=N_{m,0}e^{j\phi m}$ describes the random modulation of signal due to speckle formation; N_{Re} and N_{Im} are the real and imaginary parts of the additive noise ($var(N_{Re})=var(N_{Im})=\sigma_0^2/2$), respectively.

Consider, two laterally A-scan signals displaced by δx can be represented as $\boldsymbol{F}_1=F_1(x, z)$ and $\boldsymbol{F}_2=F_2(x +\delta x, z)$. The Doppler phase shift ($\boldsymbol{\phi}_D$) between these two A-scans is estimated using Equation (6.2) [74, 137]. Symbols with a hat (^), such as $\widehat{\phi_D}$, indicate an estimation of a signal as follows:

$$\widehat{\phi_D} = \operatorname{atan}\left[\frac{\mathrm{Im}(\mathbf{F_2F_1^*})}{\mathrm{Re}(\mathbf{F_2F_1^*})}\right] = \boldsymbol{\phi_D} + \mathbf{n_D} \tag{6.2}$$

Where, * indicates to take the conjugate of a complex value and $\boldsymbol{n}_D$ represents the random noise that arises in Doppler phase estimation.

Assume, δx << the lateral resolution of the imaging system. Therefore, the two A-scans are highly correlated and $N_m(x, z) \approx N_m(x + \delta x, z)$. Hence, estimated phase determined by the additive noise is independent for different A-scans, as demonstrated in a study by Yazdanfar *et al* [111]. Results in [111] suggested that variance of the estimated

Doppler phase (var($\widehat{\phi_D}$)=$\boldsymbol{\sigma}_\phi^2$) depends on the characteristics of the additive Gaussian noise in OCT signal regardless the value of $\boldsymbol{\phi}_D$ (Equation (6.3) where $\mu=S_0N_{m,0}$) as follows:

$$\sigma_\phi(i_x,i_z)=\frac{\sqrt{3}\sigma_0(i_x,i_z)}{S_0(i_x,i_z)N_{m,0}(i_x,i_z)}=\frac{\sqrt{3}\sigma_0}{\mu} \tag{6.3}$$

The results in [111] indicates that the magnitude of the additive noise (σ_0^2) can be calculated through Doppler variation analysis [Equation (6.4)]:

$$\sigma_0(i_x,i_z)=\frac{\sigma_\phi(i_x,i_z)S_0(i_x,i_z)N_{m,0}(i_x,i_z)}{\sqrt{3}}=\frac{\sigma_\phi\mu}{\sqrt{3}} \tag{6.4}$$

Here, i_z and i_x represent the axial and the lateral pixel indices in a discretized image, respectively.

Equations (6.3) and (6.4) indicate that Doppler variation analysis can be performed for the assessment of the additive noise. Moreover, the most prominent multiplicative noise in OCT is speckle noise and these speckle noise imposes random modulation on OCT signal ($\boldsymbol{N}_m$ in Equation (6.1)). Despite the random nature of speckle, OCT signals in adjacent A-scans ($F_1(i_x, i_z)$ and $F_2(i_x+1, i_z)$) are correlated [119]. Doppler phase estimation by Equation (6.2) effectively cancels out the randomness due to speckle, although there still remains uncertainty due to the additive noise. Such uncertainty is then quantified for the additive noise assessment according to Equation (6.4). Moreover, estimated values of σ_ϕ and μ for the additive noise assessment are calculated for each pixel using Equations (6.5) and (6.6) (assuming N_x and N_z are odd integers), respectively.

$$\sigma_\phi\widehat{(i_x,i_z)}=\frac{1}{N_xN_z}\sqrt{\sum_{\alpha_x=i_x-\frac{N_x-1}{2}}^{i_x+\frac{N_x-1}{2}}\sum_{\alpha_z=i_z-\frac{N_z-1}{2}}^{i_z+\frac{N_z-1}{2}}[\phi_D(\alpha_x,\alpha_z)-\bar{\phi}_D]} \tag{6.5}$$

$$\mu\widehat{(i_x,i_z)}=\frac{1}{N_xN_z}\sum_{\alpha_x=i_x-\frac{N_x-1}{2}}^{i_x+\frac{N_x-1}{2}}\sum_{\alpha_z=i_z-\frac{N_z-1}{2}}^{i_z+\frac{N_z-1}{2}}|F(\alpha_x,\alpha_z)| \tag{6.6}$$

Since $\widehat{\sigma_\phi}$ and $\hat{\mu}$ are calculated in Equations (6.5) and (6.6), a map of the additive noise $\widehat{\sigma_0}$ can be estimated using Equation (6.4) as follows:

$$\widehat{\sigma_0}\,(i_x, i_z) = \frac{1}{\sqrt{3}}\,\widehat{\sigma_\phi}\,(i_x, i_z)\hat{\mu}(i_x, i_z) \tag{6.7}$$

Hence, the real and imaginary parts of the complex OCT signal ($\boldsymbol{F}_{\mathrm{Re}}$=Re($\boldsymbol{F}$) and $\boldsymbol{F}_{\mathrm{Im}}$=Im($\boldsymbol{F}$)) can be optimally denoised by Wiener filtering as shown in Equations (6.8) and (6.9) [143, 144].

$$\hat{F}_{\mathrm{Re}}\left(i_x, i_z\right) = \frac{\sigma^2_{\mathrm{Re}}\left(i_x, i_z\right)\left[F_{\mathrm{Re}}\left(i_x, i_z\right) - \mu_{\mathrm{Re}}\left(i_x, i_z\right)\right]}{\sigma^2_{\mathrm{Re}}\left(i_x, i_z\right) + \sigma^2_{\mathrm{Re},n}\left(i_x, i_z\right)} + \mu_{\mathrm{Re}}\left(i_x, i_z\right) \tag{6.8}$$

$$\hat{F}_{\mathrm{Im}}\left(i_x, i_z\right) = \frac{\sigma^2_{\mathrm{Im}}\left(i_x, i_z\right)\left[F_{\mathrm{Im}}\left(i_x, i_z\right) - \mu_{\mathrm{Im}}\left(i_x, i_z\right)\right]}{\sigma^2_{\mathrm{Im}}\left(i_x, i_z\right) + \sigma^2_{\mathrm{Im},n}\left(i_x, i_z\right)} + \mu_{\mathrm{Im}}\left(i_x, i_z\right) \tag{6.9}$$

In Equations (6.8) and (6.9), μ_{Re} and μ_{Im} indicate the local means of the real and imaginary parts of the OCT signal; σ^2_{Re} and σ^2_{Im} indicate the local variance of the real and imaginary parts of the OCT signal; $\sigma^2_{Re,n}$and $\sigma^2_{Im,n}$indicate the local noise variance of the real and imaginary parts of OCT signal, respectively.

Assume that the additive noise in the real and imaginary parts of OCT signal are uncorrelated and have the same variance, we have $\sigma^2_{Re,n}$=$\sigma^2_{Im,n}$=0.5σ^2_0. Also, $\sigma^2_{Re,Im}$= (0.5$\sigma^2_{|F|}$- 0.5$\sigma^2_{0|}$) where $\sigma^2_{|F|}$ is the variance of OCT magnitude (|$\boldsymbol{F}$|). Furthermore, $\sigma^2_{Re,Im}$ is of 0 if the above calculation has a negative value [127] due to the non-negative nature of variance.

Therefore, the denoised magnitude signal of OCT can be reconstructed using Equation (6.10).

$$\hat{F}\left(i_x, i_z\right) = \sqrt{\hat{F}^2_{\mathrm{Re}}\left(i_x, i_z\right) + \hat{F}^2_{\mathrm{Im}}\left(i_x, i_z\right)} \tag{6.10}$$

6.4 OCT System and Signal Processing

A spectrometer-based Fourier domain OCT (FD-OCT) system has been used for the imaging experiments. The detail experimental setup is discussed in chapter 2. The complex denoising method is directly applied to OCT data obtained through a faster routine scanning protocol.

First, a complex B-scan OCT image ($\boldsymbol{F}$) is attained by Fourier transform on a frame of interferometric spectra according to Equation (6.1). A Doppler image $\tilde{\boldsymbol{\phi}}_D$ is created by calculating the Doppler phase shift between the same pixels in adjacent A-scans according to Equation (6.2). Afterwards, for each pixel in the Doppler image $\tilde{\boldsymbol{\phi}}_D$, local variation of Doppler phase ($\boldsymbol{\sigma}_\phi$) and mean magnitude of OCT signal are computed using pixels within N_x by N_z window (Equations (6.5) and (6.6), respectively). Once we have estimated μ and σ_ϕ , the additive noise ($\sigma_0(i_x, i_z)$) is then estimated according to Equation (6.4). Afterwards, spatially adaptive filtering on the real and imaginary parts of OCT signal at individual pixels are performed according to (Equation (6.8) and (6.9)) and eventually noise suppressed magnitude OCT image is obtained by applying (Equation (6.10)). With $N_x = N_z = 3$, it takes approximately 0.3s to generate a denoised OCT image (1024 by 1024) with MATLAB in a personal computer (Intel 2.9GHz processor, 16GB RAM). Figure 6.1 shows the flowchart for the assessment and removal of the additive OCT noise.

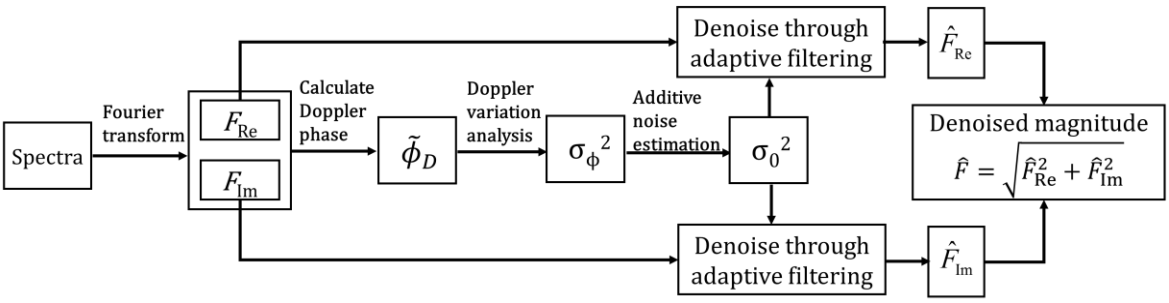

Figure 6.1 Flow-chart for the assessment and removal of additive OCT noise.
Source: [113]

6.5 Imaging Experiments and Results

To validate the method for the assessment and removal of additive noise, the following imaging experiments have been conducted:

Experiment-1: OCT images captured from a homogeneous scattering sample at different motor speeds.

Experiment-2: OCT images acquired from a homogeneous scattering sample at different signal levels.

Experiment-3: OCT images from a resolution target.

Experiment-4: OCT images from IR viewing card and *ex vivo* human skin.

6.5.1 Analysis of Results from the Experiment-1 and 2

For the first two experiments, a homogeneous scattering substance is used as a sample. The sample is translated in the axial direction with different speeds and the OCT signals are captured. Afterwards, OCT images are also acquired from a homogeneous scattering sample at different signal levels. First experiment is used to validate that Doppler phase has been correctly extracted. To generate different magnitudes of Doppler phase shift, a silicon scattering phantom (Figure 6.2 (a) with axial dimension of 1250μm and lateral

dimension of 50μm, displayed in log scale) is placed on a motorized linear translation stage, and the stage is moved in the axial direction at different speeds (v). The light beam is scanned laterally by the galvanometer with a 0.1V(p-p) driving voltage. A 20-fold oversampling is applied during the scanning process to minimize speckle decorrelation between adjacent A-scans. Once complex OCT signal are obtained from the moving phantom, the phase shift between corresponding pixels in adjacent A-scans are used to generate the Doppler image (Figure 6.2 (b)). Next, we averaged the Doppler signal, converted the Doppler phase shift to the displacement ($d=\phi_D\lambda_0/(4\pi)$) and the speed ($\tilde{v}=d/\delta t$). In this experiment, δt indicates the time interval between the acquisition of adjacent A-scans and the value is 0.11ms.

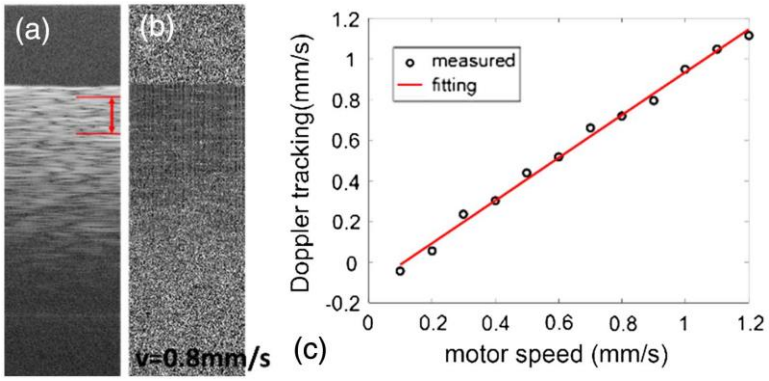

Figure 6.2 (a) Magnitude OCT image obtained from a scattering phantom; (b) Doppler OCT images; (c) the speed extracted from Doppler OCT signal ($\tilde{v}$) versus the speed of the motor (v) .
Source: [113]

Motion tracking results ($\tilde{v}$) obtained from Doppler analysis are plotted against the actual motor speeds (v) in Figure 6.2(c). The consistency between $\tilde{v}$ and v suggests that the Doppler phase is accurately extracted. Results obtained from experiments-1 and 2 are furthermore analyzed to validate the analytical relationship between the variation of estimated Doppler phase (σ_ϕ^2) and additive noise (σ_0^2) as shown in Equation (6.3). First, Equation (6.3) suggests that the variance of estimated Doppler phase (σ_ϕ^2) is independent

of the expected value of Doppler phase (ϕ_D). The σ_ϕ for Doppler OCT images from experiment-1 are computed according to Equation (6.5). All the pixels in this experiment selected within the depth range from 0.45mm to 0.65mm (between two horizontal lines in Figure 6.2(a)) to calculate σ_ϕ. The results are plotted in Figure 6.3(a).

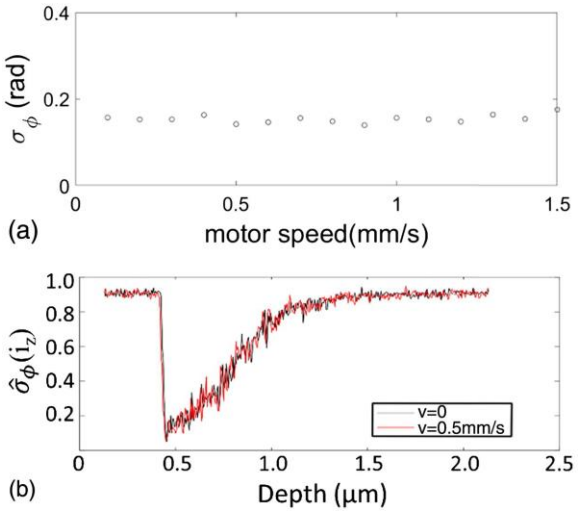

Figure 6.3 (a) σ_ϕ obtained from sample translated at different axial speeds; (b) $\sigma_\phi(i_z)$ obtained from static (black) and moving (red)sample.
Source: [113]

σ_ϕ remains approximately the same for both different magnitudes of the axial motion and different expected value Doppler phase. Additionally, Doppler images are analyzed keeping the sample at static or moving the sample at a 0.5mm/s axial speed. The standard deviation of estimated Doppler phase $\sigma_\phi(i_z)$ at different depths (i_z) are measured using Equation (6.5) with $N_z = 1$ and the calculated σ_ϕ (i_z) is almost same for the static sample (black curve) and the moving sample (red curve) at different imaging depths of the sample. Figure 6.3(a) and (b) suggest that the spatial variation of the estimated Doppler phase quantified by σ_ϕ does not depend on the magnitude of the axial motion. So, Doppler variation analysis can be applied to OCT signals from a sample that does not have any motion in the axial direction.

Furthermore, the variance of estimated Doppler phase (σ_ϕ^2) is proportional to the additive noise σ_0^2 and is inversely proportional to the magnitude of OCT signal according to Equation (6.3). Hence σ_ϕ^2 can be employed to evaluate the magnitude of the additive noise as per Equation (6.4). Image data obtained in Experiment 2 are analyzed to validate Equation (6.3). In experiment 2, we altered the intensity of sample light. An adjustable aperture into the sample arm of the OCT system is inserted, the diameter of the aperture is adjusted and a series of OCT images are acquired from the same static scattering phantom keeping other imaging conditions unchanged. For each OCT image acquired at a specific level of sample power, σ_ϕ are calculated according to Equation (6.5) with pixels in a region of interest (ROI with N_x by N_z pixels) immediately under the surface of the phantom in a 100μm depth range. The mean signal intensity for pixels within the same region is also evaluated using Equation (6.6). σ_ϕ is plotted against $\tilde{\mu}$ in Figure 6.4(a) shown as black circles. Next, the curve fitting is applied by Equation (6.3) with the experimental data (σ_ϕ and $\tilde{\mu}$). The standard variation of the additive noise: σ_0 = 0.1242 and R^2 statistics of the fitting is 0.99.

Moreover, the additive noise can be accurately assessed through the Doppler variation analysis despite the existence of multiplicative noise in OCT measurement, by analyzing the data obtained from Experiment 2. Pixels within the same ROI as the above analysis are chosen for the following calculation. The quantification is achieved by the fluctuation of the magnitude OCT signal using Equation (6.11) and is result is plotted $\sigma_{|F|}$ against mean signal magnitude ($\tilde{\mu}$) in Figure 6.4(b) as blue triangles:

$$\sigma_{|F|} = \frac{1}{N_x N_z}\sqrt{\sum_{i_z}\sum_{i_x}[|F(i_x, i_z)| - \tilde{\mu}]^2} \tag{6.11}$$

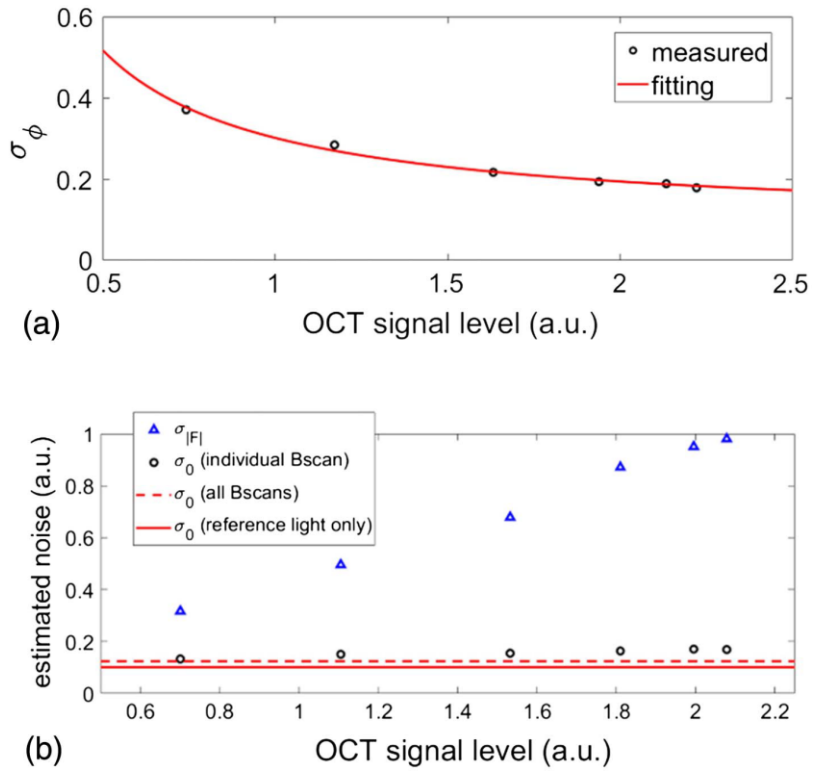

Figure 6.4 (a) Variation of Doppler phase (σ_ϕ) versus the amplitude of OCT signal (black circles: experimental data; red curve: fitting result); (b) variation of magnitude OCT signal (blue triangles), additive noise estimated through Doppler variation analysis (black circles, dashed and solid lines).
Source: [113]

Due to the existence of multiplicative noise in OCT image, such as speckle noise, the fluctuation of magnitude OCT signal increases with the signal as illustrated in Figure 6.4(b). The additive noise (σ_0) is measured with Equation (6.4) (black circles in Figure 6.4(b)), using σ_ϕ obtained from Doppler variation analysis and the estimated mean signal amplitude $\tilde{\mu}$. The noise estimated through Doppler variation analysis does not change significantly with sample light intensity. The result suggests the additive nature of noise parameters in OCT images. The additive noise in Experiment 2 remained approximately the same despite the variation of sample light intensity, because the reference power is substantially larger than the sample power and the overall additive noise largely depends

on the shot noise derived from the reference light. The level of additive noise ($\sigma_0 = 0.1242$) is obtained by fitting Equation (6.3) with σ_ϕ and $\tilde{\mu}$ (the dashed line shown in Figure 6.4(b)). Moreover, we blocked the sample arm and acquired a frame of spectral interferogram and then the noise level is derived from the reference light. The result is shown as solid line in Figure 6.4(b). Uniformity is found in the additive noise assessed through Doppler variation analysis (black circles, dashed line, and solid line), further validate Equations (6.3) and (6.4).

In Figures. 6.5(a)–6.5(c), images are obtained from the same raw spectral data with different processing methods (with axial dimension of 1250μm and lateral dimension of 50μm, displayed in log scale). Figure 6.5(a) shows the OCT magnitude without any enhancement. Figure 6.5(b) shows the OCT image processed with the complex denoising algorithm and Figure 6.5(c) is the OCT magnitude of Gaussian filtered image. Gaussian filter is given as:

$$G(i_x, i_z) = exp[-(\frac{i_x^2+i_z^2}{2w^2})] \tag{6.13}$$

Here, w denotes the standard deviation of the Gaussian function.

For complex denoising, the local variation of Doppler phase (σ_ϕ) and local mean of signal magnitude ($\tilde{\mu}$) are estimated for individual pixels within a 3×3 spatial window ($N_x = N_z = 3$ in Equations (6.5) and (6.6)). With σ_ϕ and $\tilde{\mu}$, it is possible to estimate σ_0, the additive noise for each pixel of the OCT image using Equation (6.4) and applying Equations (6.7) and (6.8) to the real and imaginary parts at each pixel of the OCT image to remove the additive noise. For the kernel used in Gaussian filtering, we selected $w = 2$ to achieve the same SNR enhancement as the complex denoising algorithm.

In contrast to the original OCT image [Figure 6.5(a)], the processed image with the complex denoising algorithm [Figure 6.5(b)] has a significantly reduced level of brightness in the background at larger imaging depth and this indicates the removal of additive noise from the background. Meanwhile, for the complex denoising algorithm, the speckle contrast remains high because the complex denoising algorithm specifically suppresses the additive noise rather than the multiplicative noise. On the other hand, Gaussian filtering has reduced the signal fluctuation level, the image contrast and also the speckle contrast.

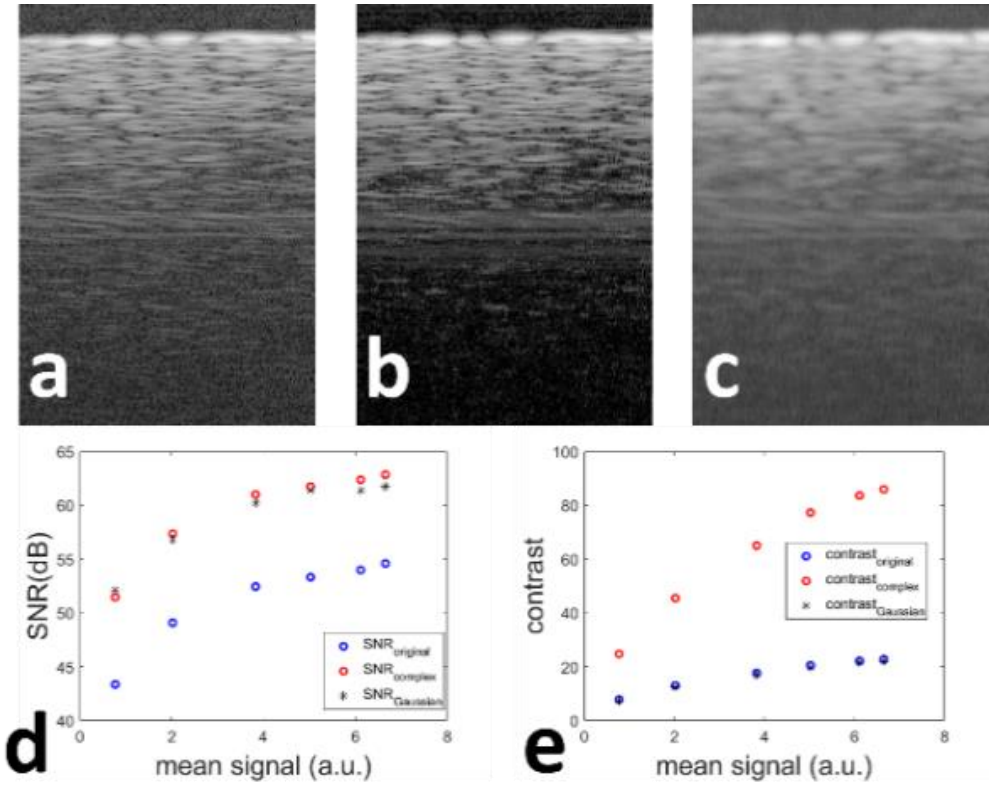

Figure 6.5 Images of a scattering phantom: (a) magnitude OCT image; (b) OCT image processed by the complex denoising algorithm; (c) OCT image filtered by a Gaussian kernel; (d) SNR for OCT images processed with different methods; (e) contrast for OCT images processed with different methods.
Source: [113]

Additionally, SNR is calculated for the images obtained with different sample light intensities according to Equation (6.14):

$$SNR = 10\ \log_{10}(\frac{\max(\boldsymbol{I})^2}{\sigma^2}) \tag{6.14}$$

The noise variance (σ^2) was estimated within a region at a large imaging depth (1mm - 1.25mm) overwhelmed by noise. SNR values of images processed with different algorithms are shown in Figure 6.5(d) (blue circles: $SNR_{original}$ for original magnitude OCT image; red circles: $SNR_{complex}$ for complex denoised OCT image; black stars: $SNR_{Gaussian}$ for Gaussian filtered OCT image). Clearly, $SNR_{complex}$ is larger than $SNR_{original}$ for images obtained with different sample light intensities.

Using data shown in Figure 6.5(d), the two curves are fitted with the following linear relationship:

$$SNR_{complex} = aSNR_{original} + b \tag{6.15}$$

Here, a = 1.0247, b = 7.07dB, $R^2 = 0.9993$.

The fitting results suggest that the complex denoising algorithm has more than 7dB SNR image enhancement. Figure 6.5(d) also suggests Gaussian filtering can achieve similar effectiveness in improving SNR. The SNR improvement proposes the complex denoising algorithm can improve sensitivity of the OCT imaging system. The sensitivity of the OCT system is the smallest signal detectable from noisy measurement [132].

Furthermore, the image contrast can also be evaluated as:

$$Image\ contrast = \frac{mean(I_{signal})}{mean(I_{background})} \tag{6.16}$$

The mean signal magnitude is estimated within the range of 0.1mm to 0.35mm, and

the mean background magnitude is considered within the range of 1mm to 1.25mm. The results of contrast analysis are shown in Figure 6.5(e) (blue circles: $Contrast_{original}$ for original magnitude OCT image; red circles: $Contrast_{complex}$ for complex denoised OCT image; black stars: $Contrast_{Gaussian}$ for Gaussian filtered OCT image). Complex denoising has significant image contrast improvement as the background noise is effectively suppressed. In contrast, Gaussian filtering has shown a slight improvement in image contrast.

6.5.2 Analysis of Results from the Experiment-3

Experiment-3 is performed to demonstrate that the complex denoising algorithm preserves the spatial resolution of OCT imaging. A resolution target (R1L3S6P, Thorlabs) in the region with 100lines/mm barcode is used as a sample and OCT images are grabbed for further image processing. The original OCT image, the image processed by the complex denoising algorithm and the image filtered by a Gaussian kernel are compared in Figure 6.6(a) (log scale images are displayed with the same dynamic range). The complex denoising algorithm improves SNR and image contrast. The results are consistent with the results shown in Figure 6.5. The lateral resolution of the OCT imaging system is determined by the spot size of the scanning lens (LSM02, Thorlabs) and is approximately 10μm. The complex denoised image shows well-preserved lateral resolution because the barcode pattern with a 10μm period is clearly noticeable. OCT signals at the depth corresponding to the surface of the resolution target are also plotted in Figure 6.6(b) (shown in a linear scale). The signal processed by the complex denoising algorithm (red, dashed) overlaps quite well with the original OCT magnitude signal (black, solid).

However, the signal generated after the Gaussian filter (blue curve) in Figure 6.6(b),

shows a smaller difference between the peaks and valleys. This suggests the reduction of imaging contrast after processing the OCT image by Gaussian filter. In addition, the A-scan is selected from the same lateral position [central A-scan in Figure 6.6(a)] in OCT images and is then processed with different methods. Afterwards, these OCT A-scans are

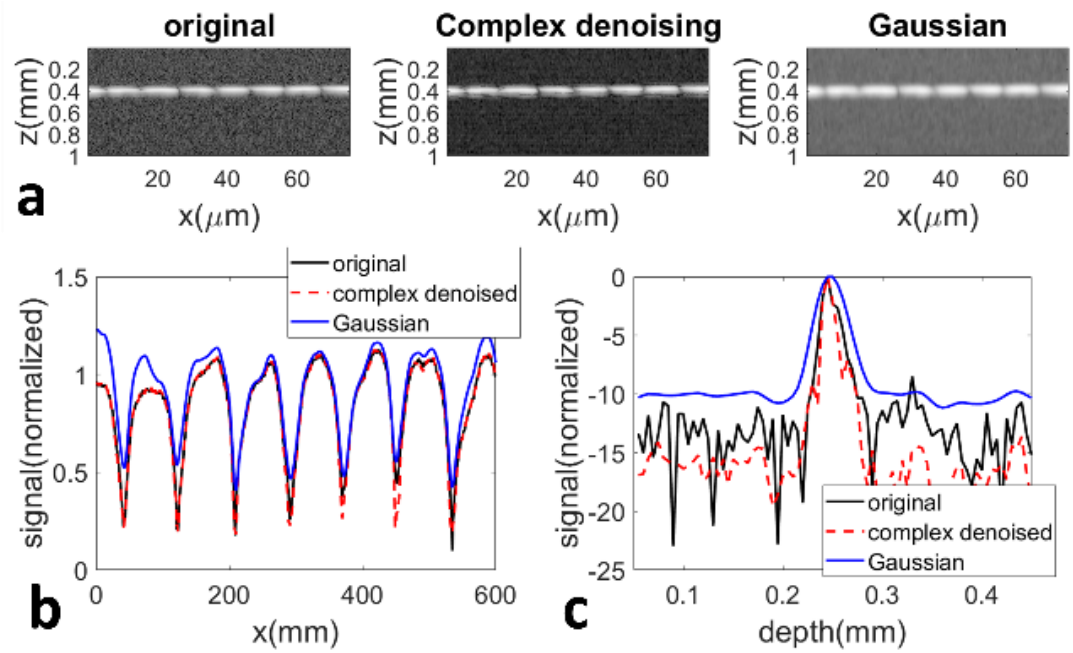

Figure 6.6 OCT images of the resolution target: (a) (left) the original magnitude of the OCT image, (middle) the image processed by the complex denoising algorithm, and (right) the image filtered by a Gaussian kernel; (b) normalized OCT signals (linear scale) at the depth corresponding to the surface of the resolution target; (c) normalized A-scans (log scale in dB) at the central lateral position (black solid curve: the original magnitude of the OCT signal; red dashed curve: the OCT signal processed by the complex denoising algorithm; blue solid curve: the OCT signal filtered by a Gaussian kernel).
Source: [113]

normalized and plotted in log scale as shown in Figure 6.6(c). Comparing the original OCT magnitude (black, solid), the signal processed by the complex denoising algorithm (red, dashed) has a reduced noise level with a sharp signal peak, while the signal processed by the Gaussian filter shows a broadening signal peak because of low spatial resolution. Figure 6.6 shows that the complex denoising method effectively removes additive noise while

preserving the spatial resolution. Because, the signal at pixels corresponding to an edge is likely to possess a larger local signal variation compared to the noise variation ($\sigma_{Re}^2 \gg \sigma_{Re,n}^2$ and $\sigma_{Im}^2 \gg \sigma_{Im,n}^2$). Therefore, according to Equations (6.7) and (6.8) for Wiener filtering, the high frequency signal component [$(F_{Re} - \mu_{Re})$ and $(F_{Im} - \mu_{Im})$] for edge pixels is well-maintained, as $\frac{\sigma_{Re}^2}{\sigma_{Re}^2 + \sigma_{Re,n}^2} \approx 1$ and $\frac{\sigma_{Im}^2}{\sigma_{Im}^2 + \sigma_{Im,n}^2} \approx 1$.

6.5.3 Analysis of Results from the Experiment-4

In experiment-4, OCT images from the fingertip of a healthy volunteer and from an infrared viewing card are captured. The experiment is performed to demonstrate that better visualization of structural features of the sample could be achieved through assessment and adaptive removal of additive noise. The original OCT image and the image processed by the complex denoising algorithm are shown in Figures 6.7(a) and 6.7(b) (displayed in logarithmic scale with the same dynamic range). In contrast to Figure 6.7(a), Figure 6.7(b) shows more visible blood vessels, as pointed by the red arrows, due to presence of low additive noise in low signal regions. The original OCT image and the complex denoised OCT image of the infrared viewing card are shown in Figures 6.7(c) and 6.7(d), where the protective plastic film and the fluorophore layers are visible.

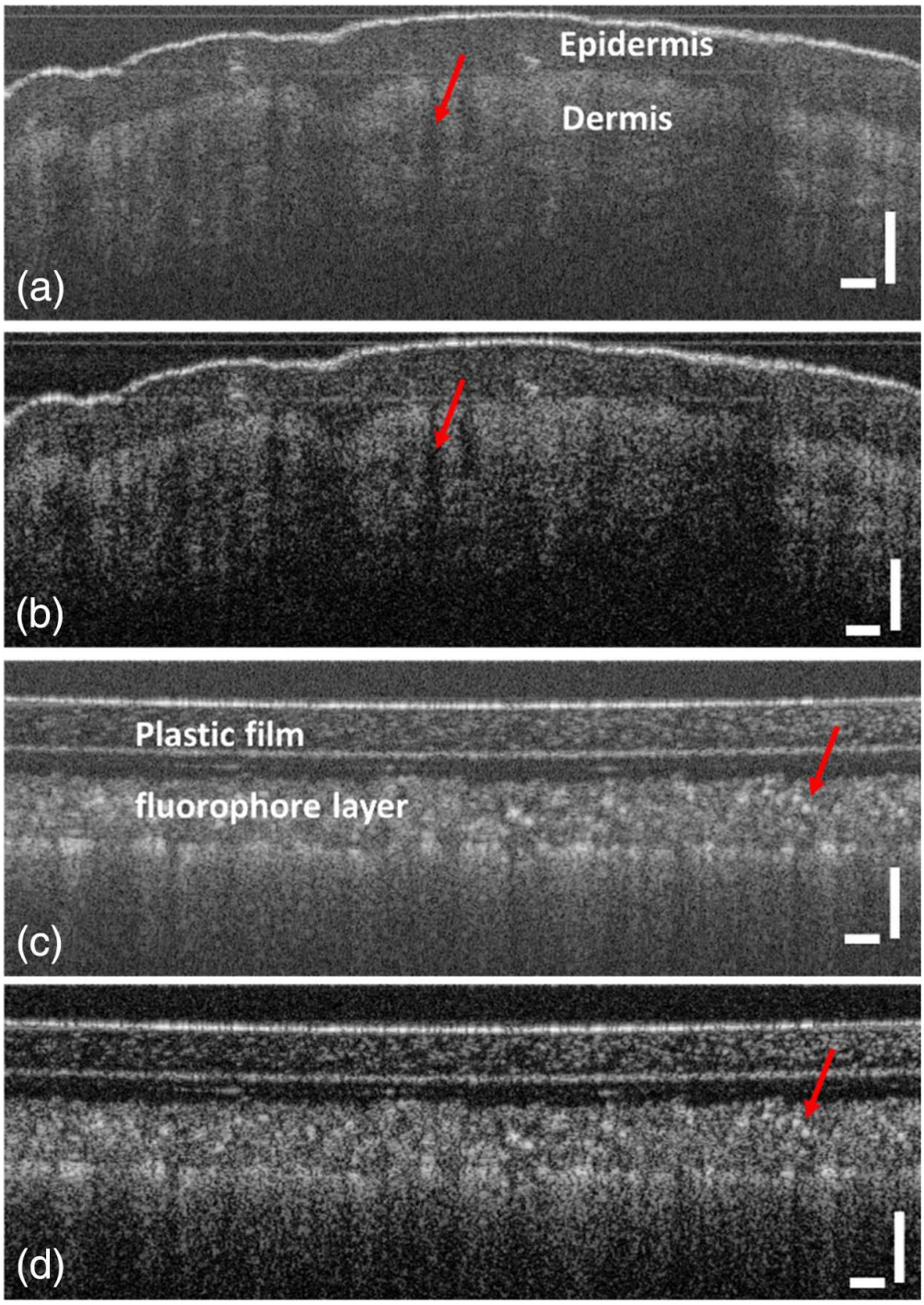

Figure 6.7 Image of a human fingertip: (a) the original magnitude of the OCT image and (b) the complex denoised OCT image, where the arrows indicate the shadow generated by blood absorption; images of the IR viewing card: (c) the original magnitude of the OCT image, and (d) the complex denoised OCT image. Scale bars represent 500μm.
Source: [113]

6.6 Summary and Conclusion

In summary, a novel technique has been developed to generate a map of additive noise for OCT images through Doppler variation analysis and is presented an innovative algorithm to adaptively eliminate additive noise from the real and imaginary parts of the complex OCT signal. The results suggest that the additive noise could be effectively evaluated through Doppler variation analysis (Figure 6.4). The complex denoising algorithm improves the SNR (Figures. 6.5 – 6.7) without compromising the spatial resolution of the OCT images. An advantage of this complex denoising method is its capability to improve the sensitivity of the OCT imaging. With reduced additive noise [N_{Re} and N_{Im} in Equation (6.1)], a weak signal [small sample reflectivity S_0 in Equation (6.1)] is easily detectable from the noisy measurement. In other words, the sensitivity of OCT image can be further improved by suppressing the additive noise.

Chapter 7

SUMMARY AND FUTURE WORK

7.1 Summary

In this dissertation, the dual modality of OCT system has been developed that can be applied for the characterization of biological tissues (such as breast tissue and brain tissue) on both morphology and stiffness to provide more accurate differentiation between cancerous and normal breast tissues. The dissertation has two parts. In Chapter 2 – 4, development and validation of qOCE technology and a handheld OCE instrument are covered. In Chapter 5 - 6, denoising algorithms have been designed and implemented to suppress the additive Gaussian and multiplicative speckle noises from the sample images acquired by SD-OCT imaging system to achieve better image quality and visualization of the tissue samples. Additionally, a couple of samples (tissue-mimicking scattering samples, IR viewing card, *ex vivo* and *in vivo* biological samples) have been used for the experiment purposes to show the effectiveness of these techniques.

Chapter 2 describes the fabrication, implementation and validation of qOCE technology based on FD-OCT system. The miniature qOCE probe integrated with a Fabry-Perot force sensor tracks both interaction force and local tissue displacement under compression and measures the tissue elasticity. The qOCE system establishes the relationship between mechanical stimulus and tissue response to characterize the stiffness of biological tissue. The qOCE technique permits direct measurement of elastic properties and therefore has great potential in many applications, such as cancer diagnosis, brain injury study, tissue engineering and biomechanical modeling. Signal processing techniques

are implemented in real-time GPU. In this study, we strategically chose the time interval between A-scans in Doppler phase calculation, to track phase shift during the process of quasi-static compression. The sensitivity of our device in force measurement could be higher than 0.25mN and the maximum applicable force through the qOCE probe was approximately 1N. The chapter also presented the application of qOCE probe on mechanical substance (phantom) as well as various biomedical applications such as in vivo (brain tissue), ex vivo (skin tissue) sample.

More importantly, the qOCE technique evaluates the stiffness of the tissue quantitatively, by simultaneously measuring the force/stress and depth resolved tissue displacement. In comparison, ultrasound elastography and conventional compression OCE are qualitative rather than quantitative because the mechanical stimulus applied to tissue is unknown during elastography imaging. The quantitative feature of our qOCE device allows results obtained from different measurement sessions to be compared and correlated for accurate tissue classification.

Chapter 3 demonstrates the capability of quantitative optical coherence elastography (qOCE) for robust assessment of material stiffness under different boundary conditions using the reaction force and displacement field established in the sample. We presented a method to achieve robust stiffness assessment using qOCE data (displacement field and reaction force) and validated the method using experimental data and fitted the result with an analytical model to extract the elastic modulus. The capability to measure stiffness under different boundary conditions is crucial for intraoperative assessment of tumor margin in situ where the boundary condition is usually not known.

Chapter 4 presents the development of a handheld OCE instrument to conveniently

interrogate the localized mechanical properties of *in vivo* tissue. Handheld OCT imaging device is an attractive detecting and surgical tool for many clinical applications, including guiding vitreous-retinal surgery, delineating tumor margin for surgical excision, and guiding tissue biopsy for the diagnosis of breast or prostate cancer. During handheld OCE characterization, the handheld probe compresses the sample and quantifies the displacement of the sample by OCT signal analyzer. However, the major challenge for manual OCE characterization of tissue is the unpredictable and unstable time varying hand maneuver generated during compression. In addition, the sample deforms under compression, implying spatial variation of motion characteristics. We have described a temporally and spatially adaptive Doppler analysis method for a robust motion tracking method for manual OCE measurement. The method selects the time interval (δt) between signals through Doppler analysis to track the motion speed $v(z,t)$ that varies temporally in a manual compression process and spatially in a deformed sample volume. The method is validated in OCE system with a handheld single fiber probe and real-time signal processing software based on GPU. The method performed an online estimation of the motion speed, selected an optimal δt adaptively and then accomplished robust motion tracking for OCE measurement. The results are obtained from phantom experiments and *in vivo* tissue characterization (local mechanical contrast of the tissue as shown in Figure 4.11(b), Figure 4.12(c) and (f)), to demonstrate the effectiveness of the adaptive Doppler analysis for motion tracking in a dynamic manual loading process. Our adaptive Doppler analysis achieves a $M_0/2$ fold improvement in the dynamic range for motion tracking compared to the conventional Doppler tracking method, where M_0 represents the number of A-scans in a frame of OCT data acquisition system.

Chapter 5 has discussed the implementation and the performance analysis of the noise adaptive wavelet thresholding (NAWT) algorithm to mitigate the speckle noise in OCT images. Speckle noise randomly alters the magnitude of OCT signal and therefore, hinders to identify the subtle features from the sample images which in turn, reduces the effectiveness of OCT system for the clinical applications. Conventional wavelet thresholding algorithms are capable of reducing the speckle noise while conserving the image sharpness [127, 128]. In wavelet thresholding, the magnitude of wavelet coefficients determines if a coefficient is noise or signal. A wavelet coefficient with larger amplitude carries signal information whereas a wavelet coefficient with smaller amplitude is noise. However, speckle noise in OCT images has different characteristics in different spatial scales, which is not considered in conventional wavelet domain thresholding. In our NAWT algorithm, the noise variance (σ_{w2}) in individual wavelet sub-band is determined and then the optimal threshold for individual sub-band.is calculated using σ_{w2}. The algorithm is simple, fast, effective and is closely related to the physical origin of speckle noise in OCT image. We have also presented a number of examples (homogeneous scattering sample, IR viewing card, *ex vivo* human fingertip) to mitigate speckle noise by NAWT algorithm in OCT imaging. NAWT algorithm results clearly have demonstrated better performance to adaptively remove speckle noise while preserving the structure features in OCT image compared to conventional wavelet domain thresholding and linear filtering. Moreover, NAWT improves the visual appearance of OCT image and shows better SNR. NAWT algorithm takes approximately 0.2s to process a 512x1024 image using CPU in MATLAB environment. The main steps of NAWT are- wavelet decomposition, soft thresholding and wavelet reconstruction. All these steps can be parallelized using

GPU. Therefore, NAWT algorithm can be implemented in GPU for real-time speckle noise removal.

In **Chapter 6**, we have developed a denoising technique to mitigate the additive noise from the complex OCT signal. Conventional denoising algorithms reflect only the magnitude of OCT and also takes into account the additive Gaussian noise. However, Phase of OCT plays a vital role in several motion tracking applications through Doppler analysis, such as, vascular visualization, blood flow measurement, OCE, cellular motion detection, etc. Moreover, OCT signal affects from both additive Gaussian and multiplicative speckle noises. In our denoising algorithm, we have first mapped and analyzed the characteristics of additive noise through Doppler variation. Next, with the help of local adaptive Weiner filter [144], we have processed and suppressed the additive noise from the real and imaginary parts of the complex OCT as independent signal channels. The denoising algorithm takes approximately 0.3s to generate a 1024x1024 denoised image using CPU in MATLAB environment. Our denoising algorithm shows the SNR and sensitivity improvement for the structural images (i.e., human finger-tip, IR viewing card), maintains the spatial resolution of OCT without any additional upgradation of SD-OCT imaging setup and data acquisition protocol.

7.2 Future Work

In conclusion, it is expected that the dual-modality OCT system will allow more effective tissue characterization and will become a powerful nominally invasive tool to assist the diagnosis and treatment of breast cancer. In the future, the generic dual-modality OCT technology can be adapted for various clinical aspects. For instance, a dual-modality OCT

sensor can be integrated with a biopsy instrument for the guidance of tissue acquisition. Intraoperative OCT characterization of tissue at the point of biopsy will lead the advancement in the diagnosis of breast cancer with improved accuracy. For surgical excision of breast tumor, dual-modality OCT can help generate a negative margin through intraoperative malignancy assessment.

REFERENCES

[1] C. A. Taylor, J. M. Bell, M. J. Breiding, and L. Xu, "Traumatic brain injury–related emergency department visits, hospitalizations, and deaths — United States, 2007 and 2013," *MMWR Surveillance Summary 2017*; vol. 66, no. SS-9, pp. 1–16. [Online] Available: https://www.cdc.gov/mmwr/volumes/66/ss/ss6609a1.htm#suggestedcitation [Accessed: March. 27, 2019].

[2] American Cancer Society, "Breast cancer facts and figures 2015-2016", Atlanta: American Cancer Society, Inc. 2015. [Online] Available:https://www.cancer.org/content/dam/cancer-org/research/cancer-facts-and-statistics/breast-cancer-facts-and-figures/breast-cancer-facts-and-figures-2015-2016.pdf [Accessed: March. 27, 2019].

[3] P. N. Wells and H. D. Liang, "Medical ultrasound: imaging of soft tissue strain and elasticity," *Journal of the Royal Society, Interface*, vol. 8, no. 64, pp. 1521-49, 2011.

[4] S. Wojcinski, A. Farrokh, S. Weber, A. Thomas, T. Fischer, T. Slowinski, W. Schmidt, and F. Degenhardt, "Multicenter study of ultrasound real-time tissue elastography in 779 cases for the assessment of breast lesions: Improved diagnostic performance by combining the BI-RADSR - US classification system with sonoelastography," *Ultraschall in der Medizin*, vol. 31, no. 5, pp. 484–491, 2010.

[5] O. S. Jaffer, P. F. C. Lung, D. Bosanac, A. Shah, and P. S. Sidhu, "Is ultrasound elastography of the liver ready to replace biopsy? A critical review of the current techniques," *Ultrasound*, vol. 20, pp. 24–32, 2012.

[6] B. F. Kennedy, K. M. Kennedy, and D. D. Sampson, "Optical coherence elastography," *Optics & Photonics News*, vol. 26, no. 4, pp. 32-39, 2015.

[7] J. F. Greenleaf, M. Fatemi, and M. Insana. "Selected methods for imaging elastic properties of biological tissues," *Annual Review of Biomedical Engineering* 5, 57-781, 2003.

[8] T. A. Krouskop, T. M. Wheeler, F. Kallel, B. S. Garra, and T. Hall, "Elastic moduli of breast and prostate tissues under compression," *Ultrasonic Imaging*, vol. 20, no. 4, pp. 260–274, 1998.

[9] A. Samani, J. Zubovits, and D. Plewes, "Elastic moduli of normal and pathological human breast tissues: An inversion-technique-based investigation of 169 samples," *Physics in Medicine and Biology*, vol. 52, no. 6, pp. 1565 1576, 2007.

[10] K. Hoyt, B. Castaneda, M. Zhang, P. Nigwekar, P. A. di Sant'agnese, J. V. Joseph, J. Strang, D. J. Rubens, and K. J. Parker, "Tissue elasticity properties as biomarkers for prostate cancer," *Cancer Biomarkers*, vol. 4, no. 4-5, pp. 213–225, 2008.

[11] K. Arda, N. Ciledag, E. Aktas, B. K. Aribas, and K. Köse, "Quantitative assessment of normal soft-tissue elasticity using shear-wave ultrasound elastography," *American Journal of Roentgenology*, vol. 197, no. 3, pp. 532–536, 2011.

[12] X. Liang, V. Crecea, and S. A. Boppart, "Dynamic optical coherence elastography: A Review," *Journal of Innovative Optical Health Sciences*, vol. 3, no. 4, pp. 221–233, 2010.

[13] K. M. Kennedy, L. Chin, R. A. McLaughlin, B. Latham, C. M. Saunders, D. D. Sampson, and B. F. Kennedy, "Quantitative micro-elastography: imaging of tissue elasticity using compression optical coherence elastography," *Scientific Reports*, vol. 5, no. 1, 2015.

[14] R. Karimi, T. Zhu, B. E. Bouma, and M. R. K. Mofrad, "Estimation of nonlinear mechanical properties of vascular tissues via elastography," *Cardiovascular Engineering*, vol. 8, no. 4, pp. 191–202, 2008.

[15] W. F. Cheong, S. A. Prahl, and A. J. Welch, "A review of the optical properties of biological tissues," *IEEE Journal of Quantum Electronics*, vol. 26, no. 12, pp. 2166-2185, 1990.

[16] D. Huang, E. A. Swanson, C. P. Lin, J. S. Schuman, W. G. Stinson, W. Chang, M. R. Hee, T. Flotte, K. Gregory, and C. A. Puliafito, "Optical coherence tomography," *Science*, vol. 254, no. 5035, pp. 1178–1181, 1991.

[17] W. Drexler, M. Liu, A. Kumar, T. Kamali, A. Unterhuber, and R. A. Leitgeb, "Optical coherence tomography today: speed, contrast, and multimodality," *Journal of Biomed. Optics*, vol. 19, no. 7, 2014.

[18] F. Zaki, Y. Wang, H. Su, X. Yuan, and X. Liu, "Noise adaptive wavelet thresholding for speckle noise removal in optical coherence tomography," *Biomedical Optics Express*, vol. 8, no. 5, pp. 2720-2731, 2017.

[19] X. Liu, F. Zaki, Y. Wang, Q. Huang, X. Mei, and J. Wang, "Secure fingerprint identification based on structural and microangiographic optical coherence tomography," *Applied Optics*, vol. 56, no.8, pp. 2255-2259, 2017.

[20] M. Zhang, L. Ma, and P. Yu, "Dual-band Fourier domain optical coherence tomography with depth-related compensations," *Biomedical Optics Express*, vol. 5, no. 1, pp. 167-182, 2014.

[21] J. M. Schmitt, S. H. Xiang, and K. M. Yung, "Speckle in optical coherence tomography," *Journal of Biomedical Optics*, vol. 4, pp. 95–105, 1999.

[22] A. Curatolo, B. F. Kennedy, D. D. Sampson, and T. R. Hillman, "Speckle in optical coherence tomography," in *Advanced Photonics: Tissue Optical Sectioning*, R. K. Wang, and V. V. Tuchin, Boca Raton, FL: Eds. CRC Press, 2014, pp- 211-277.

[23] M. Born and E. Wolf, *Principles of Optics: Electromagnetic Theory of Propagation, Interference and Diffraction of Light*, Rochester, NY: Cambridge University Press, 1999.

[24] M. Villiger and T. Lasser, "Image formation and tomogram reconstruction in optical coherence microscopy," *Journal of the Optical Society of America A*, vol. 27, pp. 2216–2228, 2010.

[25] M. Bashkansky and J. Reintjes, "Statistics and reduction of speckle in optical coherence tomography," *Optics Letters*, vol. 25, pp. 545–547, 2000.

[26] M. Pircher, E. Gotzinger, R. Leitgeb, A. F. Fercher, and C. K. Hitzenberger, "Speckle reduction in optical coherence tomography by frequency compounding," *Journal of Biomedical Optics*, vol. 8, pp. 565–569, 2003.

[27] A. E. Desjardins, B. J. Vakoc, W. Y. Oh, S. M. R. Motaghiannezam, G. J. Tearney, and B. E. Bouma, "Angle-resolved Optical Coherence Tomography with sequential angular selectivity for speckle reduction," *Optics Express*, vol. 15, pp. 6200–6209, 2007.

[28] J. M. Schmitt, "Array detection for speckle reduction in optical coherence microscopy," *Physics in Medicine and Biology*, vol. 42, pp. 1427–1439, 1997.

[29] A. E. Desjardins, B. J. Vakoc, G. J. Tearney, and B. E. Bouma, "Speckle reduction in OCT using massively-parallel detection and frequency-domain ranging," *Optics Express*, vol. 14, pp. 4736–4745, 2006.

[30] B. Karamata, M. Laubscher, M. Leutenegger, S. Bourquin, T. Lasser, and P. Lambelet, "Multiple scattering in optical coherence tomography. I. Investigation and modeling," *Journal of the Optical Society of America A*, vol. 22, pp. 1369–1379, 2005.

[31] D. P. Popescu, M. D. Hewko, and M. G. Sowa, "Speckle noise attenuation in optical coherence tomography by compounding images acquired at different positions of the sample," *Optics Communications*, vol. 269, pp. 247–251, 2007.

[32] T. M. Jorgensen, L. Thrane, M. Mogensen, F. Pedersen, and P. E. Andersen, "Speckle reduction in optical coherence tomography images of human skin by a spatial diversity method," Proceedings of SPIE 6627, 6627–6620P, 2007.

[33] B. F. Kennedy, T. R. Hillman, A. Curatolo, and D. D. Sampson, "Speckle reduction in optical coherence tomography by strain compounding," *Optics Letters*, vol. 35, pp. 2445–2447, 2010.

[34] B. F. Kennedy, A. Curatolo, T. R. Hillman, C. M. Saunders, and D. D. Sampson, "Speckle reduction in optical coherence tomography images using tissue viscoelasticity," *Journal of Biomedical Optics*, vol. 16, 2011.

[35] S.H. Xiang, L. Zhou, J.M. Schmitt, Proceedings of SPIE, 3196, vol. 79, 1997.

[36] D. C. Adler, T. H. Ko, and J. G. Fujimoto, "Speckle reduction in optical coherence tomography images by use of a spatially adaptive wavelet filter," *Optics Letters*, vol. 29, pp. 2878–2880, 2004.

[37] D. C. Fernandez, "Delineating fluid-filled region boundaries in optical coherence tomography images of the retina," *IEEE Transactions on Medical Imaging*, vol. 24, pp. 929–945, 2005.

[38] J. Schmitt, "OCT elastography: imaging microscopic deformation and strain of tissue," *Optics Express*, vol. 3, no. 6, pp. 199–211, 1998.

[39] B. F. Kennedy, P. Wijesinghe, and D. D. Sampson, "The emergence of optical elastography in biomedicine," *Nature Photonics*, vol. 11, pp. 215–221, 2017.

[40] S. C. Cowin and S. B. Doty, *Tissue Mechanics*, New York City, NY: Springer, 2007.

[41] S. J. Kirkpatrick and D. D. Duncan, "Optical assessment of tissue mechanics," in *Handbook of Optical Biomedical Diagnostics*, V. V. Tuchin, Ed. Bellingham, WA, USA: SPIE, 2002, pp. 1037–1084.

[42] J. Ophir, S. K. Alam, B. Garra, F. Kallel, E. Konofagou, T. Krouskop, and T. Varghese, "Elastography: Ultrasonic estimation and imaging of the elastic properties of tissues," *Proceedings of the Institution of Mechanical Engineers*, vol. 213, no. 3, pp. 203–233, 1999.

[43] K. J. Parker, M. M. Doyley, and D. J. Rubens, "Imaging the elastic properties of tissue: The 20 year perspective," *Physics in Medicine and Biology*, vol. 56, no. 1, pp. R1–R29, 2011.

[44] B. F. Kennedy, K. M. Kennedy, and D. D. Sampson, "A review of optical coherence elastography: fundamentals, techniques and prospects," *IEEE Journal of Selected Topics on Quantum Electronics*, vol. 20, no. 2, pp. 272–288, 2014.

[45] K. J. Parker, L. S. Taylor, S. Gracewski, and D. J. Rubens, "A unified view of imaging the elastic properties of tissue," *The Journal of the Acoustical Society of America*, vol. 117, no. 5, pp. 2705–2712, 2005.

[46] X. Zhang and J. F. Greenleaf, "Estimation of tissue's elasticity with surface wave speed," *The Journal of the Acoustical Society of America.*, vol. 122, pp. 2522–2525, 2007.

[47] B. F. Kennedy, S. H. Koh, R. A. McLaughlin, K. M. Kennedy, P. R. T. Munro, and D. D. Sampson, "Strain estimation in phase-sensitive optical coherence elastography," *Biomedical Optics Express*, vol. 3, no. 8, pp. 1865–1879, 2012.

[48] B. F. Kennedy, T. R. Hillman, R. A. McLaughlin, B. C. Quirk, and D. D. Sampson, "*In vivo* dynamic optical coherence elastography using a ring actuator," *Optics Express*, vol. 17, no. 24, pp. 21762–21772, 2009.

[49] K. D. Mohan and A. L. Oldenburg, "Elastography of soft materials and tissues by holographic imaging of surface acoustic waves," *Optics Express*, vol. 20, no. 17, pp. 18887–18897, 2012.

[50] V. Crecea, A. L. Oldenburg, X. Liang, T. S. Ralston, and S. A. Boppart, "Magnetomotive nanoparticle transducers for optical rheology of viscoelastic materials," *Optics Express*, vol. 17, no. 25, pp. 23114–23122, 2009.

[51] A. Chau, R. Chan, M. Shishkov, B. MacNeill, N. Iftimia, G. Tearney, R. Kamm, B. Bouma, and M. Kaazempur-Mofrad, "Mechanical analysis of atherosclerotic plaques based on optical coherence tomography," *Annals of Biomedical Engineering*, vol. 32, no. 11, pp. 1494–1503, 2004.

[52] R. Chan, A. Chau, W. Karl, S. Nadkarni, A. Khalil, N. Iftimia, M. Shishkov, G. Tearney, M. Kaazempur-Mofrad, and B. Bouma, "OCT based arterial elastography: Robust estimation exploiting tissue biomechanics," *Optics Express*, vol. 12, no. 19, pp. 4558–4572, 2004.

[53] F. M. Hendriks, D. Brokken, C. W. Oomens, D. L. Bader, and F. P. Baaijens, "The relative contributions of different skin layers to the mechanical behavior of human skin *in vivo* using suction experiments," *Medical Engineering and Physics*, vol. 28, no. 3, pp. 259–266, 2006.

[54] H. J. Ko, W. Tan, R. Stack, and S. A. Boppart, "Optical coherence elastography of engineered and developing tissue," *Tissue Engineering*, vol. 12, no. 1, pp. 63–73, 2006.

[55] S. J. Kirkpatrick, R. K. Wang, and D. D. Duncan, "OCT-based elastography for large and small deformations," *Optics Express*, vol. 14, no. 24, pp. 11585–11597, 2006.

[56] R. K. Wang, Z. Ma, and S. J. Kirkpatrick, "Tissue Doppler optical coherence elastography for real time strain rate and strain mapping of soft tissue," *Applied Physics Letters*, vol. 89, no. 14, pp. 144103-1–144103-3, 2006.

[57] R. K. Wang, S. Kirkpatrick, and M. Hinds, "Phase-sensitive optical coherence elastography for mapping tissue microstrains in real time," *Applied Physics Letters*, vol. 90, pp. 164105-1–164105-3, 2007.

[58] B. F. Kennedy, X. Liang, S. G. Adie, D. K. Gerstmann, B. C. Quirk, S. A. Boppart, and D. D. Sampson, "*In vivo* three-dimensional optical coherence elastography," *Optics Express*, vol. 19, no. 7, pp. 6623–6634, 2011.

[59] X. Liang, A. L. Oldenburg, V. Crecea, E. J. Chaney, and S. A. Boppart, "Optical micro-scale mapping of dynamic biomechanical tissue properties," *Optics Express*, vol. 16, no. 15, pp. 11052–11065, 2008.

[60] B. F. Kennedy, M. Wojtkowski, M. Szkulmowski, K. M. Kennedy, K. Karnowski, and D. D. Sampson, "Improved measurement of vibration amplitude in dynamic optical coherence elastography," *Biomedical Optics Express*, vol. 3, no. 12, pp. 3138–3152, 2012.

[61] C. Li, G. Guan, Z. Huang, M. Johnstone, and R. K. Wang, "Noncontact all-optical measurement of corneal elasticity," *Optics Letters*, vol. 37, no. 10, pp. 1625–1627, 2012.

[62] S. Wang, K. Larin, J. Li, S. Vantipalli, R. K. Manapuram, S. Aglyamov, S. Emelianov, and M. D. Twa, "A focused air-pulse system for optical-coherence-tomography-based measurements of tissue elasticity," *Laser Physics Letters*, vol. 10, no. 7, pp. 075605-1–075605-6, 2013.

[63] C. Li, G. Guan, X. Cheng, Z. Huang, and R. K. Wang, "Quantitative elastography provided by surface acoustic waves measured by phase sensitive optical coherence tomography," *Optics Letters*, vol. 37, no. 4, pp. 722–724, 2012.

[64] R. K. Manapuram, S. R. Aglyamov, F. M. Monediado, M. Mashiatulla, J. Li, S. Y. Emelianov, and K. V. Larin, "*In vivo* estimation of elastic wave parameters using phase-stabilized swept source optical coherence elastography," *Journal of Biomedical Optics*, vol. 17, no. 10, pp. 100501-1–100501-3, 2012.

[65] X. Liang and S. A. Boppart, "Biomechanical properties of *in vivo* human skin from dynamic optical coherence elastography," *IEEE Transactions on Biomedical Engineering*, vol. 57, no. 4, pp. 953–959, Apr. 2010.

[66] S. Li, K. D. Mohan, W. W. Sanders, and A. L. Oldenburg, "Toward soft tissue elastography using digital holography to monitor surface acoustic waves," *Journal of Biomedical Optics*, vol. 16, no. 11, pp. 116005-1–116005-7, 2011.

[67] A. L. Oldenburg, G. Wu, D. Spivak, F. Tsui, A. S. Wolberg, and T. H. Fischer, "Imaging and elastometry of blood clots using magnetomotive optical coherence tomography and labeled platelets," *IEEE Journal of Quantum Electronics*, vol. 18, no. 3, pp. 1100–1109, 2012.

[68] A. L. Oldenburg and S. A. Boppart, "Resonant acoustic spectroscopy of soft tissues using embedded magnetomotive nanotransducers and optical coherence tomography," *Physics in Medicine and Biology*, vol. 55, no. 4, pp. 1189–1201, 2010.

[69] A. Grimwood, L. Garcia, J. Bamber, J. Holmes, P. Woolliams, P. Tomlins, and Q. A. Pankhurst, "Elastographic contrast generation in optical coherence tomography from a localized shear stress," *Physics in Medicine and Biology*, vol. 55, pp. 5515–5528, 2010.

[70] G. Wu, C. Krebs, F.-C. Lin, A. S. Wolberg, and A. L. Oldenburg, "High sensitivity micro-elastometry: Applications in blood coagulopathy," *Annals of Biomedical Engineering*, vol. 41, no. 10, pp. 2120–2129, 2013.

[71] V. Crecea, A. Ahmad, and S. A. Boppart, "Magnetomotive optical coherence elastography for microrheology of biological tissues," *Journal of Biomedical Optics*, vol. 18, no. 12, pp. 121504-1–121504-5, 2013.

[72] D. D. Kalanovic, M. P. Ottensmeyer, J. Gross, G. Buess, and S. L. Dawson, "Independent testing of soft tissue viscoelasticity using indentation and rotary shear deformations," *Studies in Health Technology and Informatics*, vol. 94, pp. 137–143, 2003.

[73] Y. Huang, X. Liu, and J. U. Kang, "Real-time 3D and 4D Fourier domain Doppler optical coherence tomography based on dual graphics processing units," *Biomedical Optics Express*, vol. 3, no. 9, pp. 2162–2174, 2012.

[74] Y. Qiu, Y. Wang, Y. Xu, N. Chandra, J. Haorah, B. Hubbi, B. J. Pfister, and X. Liu, "Quantitative optical coherence elastography based on fiber-optic probe for in situ measurement of tissue mechanical properties," *Biomedical Optics Express*, vol. 7, no. 2, pp. 688–700, 2016.

[75] A. Karimi and M. Navidbakhsh, "An experimental study on the mechanical properties of rat brain tissue using different stress-strain definitions," *Journal of Materials Science: Materials in Medicine*, vol. 25, no. 7, pp. 1623–1630, 2014.

[76] R. W. Ogden, *Non-Linear Elastic Deformations*, Mineola, NY: Dover Publications, Inc., 1997.

[77] A. F. Bower, *Applied Mechanics of Solids*, Boca Raton, FL: CRC Press, 2009.

[78] A. Delalleau, G. Josse, J.-M. Lagarde, H. Zahouani, and J. M. Bergheau, "A nonlinear elastic behavior to identify the mechanical parameters of human skin in vivo," *Skin Research and Technology*, vol. 14, no. 2, pp. 152–164, 2008.

[79] A. A. Oberai, N. H. Gokhale, S. Goenezen, P. E. Barbone, T. J. Hall, A. M. Sommer, and J. Jiang, "Linear and nonlinear elasticity imaging of soft tissue in vivo: demonstration of feasibility," *Physics in Medicine and Biology*, vol. 54, no. 5, pp. 1191– 1207, 2009.

[80] D. R. Veronda and R. A. Westmann, "Mechanical characterization of skin—finite deformations," *Journal of Biomechanics*, vol. 3, no. 1, pp. 111-122, 1970.

[81] S. Ganpule, A. Alai, E. Plougonven, and N. Chandra, "Mechanics of blast loading on the head models in the study of traumatic brain injury using experimental and computational approaches," *Biomechanics and Modeling in Mechanobiology*, vol. 12, no. 3, pp. 511–531, 2013.

[82] V. Mishra, M. Skotak, H. Schuetz, A. Heller, J. Haorah, and N. Chandra, "Primary blast causes mild, moderate, severe and lethal TBI with increasing blast overpressures: Experimental rat injury model," *Scientific Reports*, vol. 6, 2016.

[83] C. T. McKee, J. A. Last, P. Russell, and C. J. Murphy, "Indentation versus tensile measurements of Young's modulus for soft biological tissues," *Tissue Engineering Part B Reviews*, vol. 17, no. 3, pp. 155–164, 2011.

[84] J. D. Finan, B. S. Elkin, E. M. Pearson, I. L. Kalbian, and B. Morrison 3rd, "Viscoelastic properties of the rat brain in the sagittal plane: effects of anatomical structure and age," *Annals of Biomedical Engineering*, vol. 40, no. 1, pp. 70–78, 2012.

[85] A. C. Voogd, M. Nielsen, J. L. Pieterse, M. Blichert-Toft, H. Bartelink, M. Overgaard, G. van Tienhoven, K. W. Andersen, R. J. Sylvester, and J. A. van Dongen, "Differences in risk factors for local and distant recurrence after breast-conserving therapy or mastectomy for stage I and II breast cancer: Pooled results of two large European randomized trials," *Journal of Clinical Oncology*, vol. 19, no. 6, 1688–1697, 2001.

[86] J. Ophir, I. Céspedes, H. Ponnekanti, Y. Yazdi, and X. Li, "Elastography: a quantitative method for imaging the elasticity of biological tissues," *Ultrasonic Imaging*, vol. 13, no. 2, pp. 111–134, 1991.

[87] R. Muthupillai, D. J. Lomas, P. J. Rossman, J. F. Greenleaf, A. Manduca, and R. L. Ehman, "Magnetic resonance elastography by direct visualization of propagating acoustic strain waves," *Science*, vol. 269, no.5232, pp. 1854–1857, 1995.

[88] S. A. Boppart, W. Luo, D. L. Marks, and K. W. Singletary, "Optical coherence tomography: Feasibility for basic research and image-guided surgery of breast cancer," *Breast Cancer Research and Treatment*, vol. 84, no. 2, pp. 85–97, 2004.

[89] F. T. Nguyen, A. M. Zysk, E. J. Chaney, J. G. Kotynek, U. J. Oliphant, F. J. Bellafiore, K. M. Rowland, P. A. Johnson, and S. A. Boppart, "Intraoperative evaluation of breast tumor margins with optical coherence tomography," *Cancer Research*, vol. 69, no. 22, pp. 8790–8796, 2009.

[90] K. M. Kennedy, R. A. McLaughlin, B. F. Kennedy, A. Tien, B. Latham, C. M. Saunders, and D. D. Sampson, "Needle optical coherence elastography for the measurement of microscale mechanical contrast deep within human breast tissues," *Journal of Biomedical Optics*, vol. 18, no. 12, 2013.

[91] K. M. Kennedy, B. F. Kennedy, R. A. McLaughlin, and D. D. Sampson, "Needle optical coherence elastography for tissue boundary detection," *Optics Letters*, vol. 37, no. 12, pp. 2310–2312, 2012.

[92] X. Liu, F. Zaki, H. Wu, C. Wang, and Y. Wang, "Temporally and spatially adaptive Doppler analysis for robust handheld optical coherence elastography," *Biomedical Optics Express*, vol. 9, no.7, pp. 3335–3353, 2018.

[93] Y. Qiu, F. Zaki, N. Chandra, S. A. Chester, and X. Liu, "Nonlinear characterization of elasticity using quantitative optical coherence elastography," *Biomedical Optics Express*, vol. 7, no. 11, pp. 4702–4710, 2016.

[94] M. H. Sadd, *Elasticity: Theory, Applications, and Numerics*, NY, Academic Press, 2009.

[95] Y. C. Fung, *Biomechanics: Mechanical Properties of Living Tissues*, Berlin, Germany: Springer Science and Business Media, 2013.

[96] Z. Wang, A. A. Volinsky, and N. D. Gallant, "Crosslinking effect on polydimethylsiloxane elastic modulus measured by custom-built compression instrument," *Journal of Applied Polymer Science*, vol. 131, no. 22, 2014.

[97] B. S. Elkin, A. I. Ilankovan, and B. Morrison III, "A detailed viscoelastic characterization of the P17 and adult rat brain,". *Journal of Neurotrauma*, vol. 28, no. 11, pp. 2235–2244, 2011.

[98] W. Hayes, L. Keer, G. Herrmann, and L. Mockros, "A mathematical analysis for indentation tests of articular cartilage," *Journal of Biomechanics*, vol. 5, no.5, 541–551, 1972.

[99] X. Li, C. Chudoba, T. Ko, C. Pitris, and J. G. Fujimoto, "Imaging needle for optical coherence tomography," *Optics Letters*, vol. 25, no. 20, pp. 1520–1522, 2000.

[100] D. Lorenser, X. Yang, R. W. Kirk, B. C. Quirk, R. A. McLaughlin, and D. D. Sampson, "Ultrathin side-viewing needle probe for optical coherence tomography," *Optics Letters*, vol. 36, no. 19, pp. 3894–3896, 2011.

[101] Y. Qiu, Y. Wang, K. D. Belfield, and X. Liu, "Ultrathin lensed fiber-optic probe for optical coherence tomography," *Biomedical Optics Express*, vol. 7, no. 6, pp. 2154–2162, 2016.

[102] J. U. Kang, J.-H. Han, X. Liu, K. Zhang, C. G. Song, and P. Gehlbach, "Endoscopic functional Fourier domain common-path optical coherence tomography for microsurgery," *IEEE Journal of Selected Topics on Quantum Electronics*, vol. 16, no. 4, pp. 781–792, 2010.

[103] A. M. Zysk, K. Chen, E. Gabrielson, L. Tafra, E. A. May Gonzalez, J. K. Canner, E. B. Schneider, A. J. Cittadine, P. Scott Carney, S. A. Boppart, K. Tsuchiya, K. Sawyer, and L. K. Jacobs, "Intraoperative assessment of final margins with a handheld optical imaging probe during breast-conserving surgery may reduce the reoperation rate: Results of a multicenter study," *Annals of Surgical Oncology*, vol. 22, no**.** 10, pp. 3356–3362, 2015.

[104] K. V. Larin and D. D. Sampson, "Optical coherence elastography - OCT at work in tissue biomechanics [Invited]," *Biomedical Optics Express***,** vol. 8, no. 2, 1172–1202, 2017.

[105] D. Chavan, J. Mo, M. de Groot, A. Meijering, J. F. de Boer, and D. Iannuzzi, "Collecting optical coherence elastography depth profiles with a micromachined cantilever probe," *Optics Letters*, vol. 38, no. 9, pp.1476–1478, 2013.

[106] S. Es'haghian, K. M. Kennedy, P. Gong, Q. Li, L. Chin, P. Wijesinghe, D. D. Sampson, R. A. McLaughlin, and B. F. Kennedy, "In vivo volumetric quantitative micro-elastography of human skin," *Biomedical Optics Express*, vol. 8, no. 5, pp. 2458–2471, 2017.

[107] X. Liang, S. G. Adie, R. John, and S. A. Boppart, "Dynamic spectral-domain optical coherence elastography for tissue characterization," *Optics Express*, vol. 18, no. 13, pp. 14183–14190, 2010.

[108] H. C. Hendargo, M. Zhao, N. Shepherd, and J. A. Izatt, "Synthetic wavelength-based phase unwrapping in spectral domain optical coherence tomography," *Optics Express*, vol. 17, no. 7, pp. 5039–5051, 2009.

[109] Y. Wang, D. Huang, Y. Su, and X. S. Yao, "Two-dimensional phase unwrapping in Doppler Fourier domain optical coherence tomography," *Optics Express*, vol. 24, no. 23, pp. 26129–26145, 2016.

[110] S. G. Adie, X. Liang, B. F. Kennedy, R. John, D. D. Sampson, and S. A. Boppart, "Spectroscopic optical coherence elastography," *Optics Express*, vol. 18, no. 25, pp. 25519–25534, 2010.

[111] B. Park, M. C. Pierce, B. Cense, S.-H. Yun, M. Mujat, G. Tearney, B. Bouma, and J. de Boer, "Real-time fiber based multi-functional spectral-domain optical coherence tomography at 1.3 μm," *Optics Express*, vol. 13, no. 11, pp. 3931–3944, 2005.

[112] S. Yazdanfar, C. Yang, M. V. Sarunic, and J. A. Izatt, "Frequency estimation precision in Doppler optical coherence tomography using the Cramer-Rao lower bound," *Optics Express*, vol. 13, no. 2, pp. 410–416, 2005.

[113] X. Liu, F. Zaki, and D. Renaud, "Assessment and removal of additive noise in complex OCT signal based on Doppler variation analysis," *Applied Optics*, vol. 57, no. 13, pp. 2873–2880, 2018.

[114] Y. Zhao, Z. Chen, C. Saxer, S. Xiang, J. F. de Boer, and J. S. Nelson, "Phase-resolved optical coherence tomography and optical Doppler tomography for imaging blood flow in human skin with fast scanning speed and high velocity sensitivity," *Optics Letter*, vol. 25, no. 2, pp. 114–116, 2000.

[115] A. F. Fercher, W. Drexler, C. K. Hitzenberger, and T. Lasser, "Optical coherence tomography-principles and applications," *Reports on Progress in Physics*, vol. 66, no. 2, pp. 239–303, 2003.

[116] A. M. Zysk, F. T. Nguyen, A. L. Oldenburg, D. L. Marks, and S. A. Boppart, "Optical coherence tomography: a review of clinical development from bench to bedside," *Journal of Biomedical Optics*, vol. 12, no. 5, article no. 051403, 2007.

[117] J. W. Goodman, *Statistical Optics,* NY, USA: John Wiley and Sons, 2015.

[118] J. W. Goodman, "Some fundamental properties of speckle," *Journal of the Optical Society of America*, vol. 66, no. 11, pp. 1145–1150, 1976.

[119] X. Liu, J. C. Ramella-Roman, Y. Huang, Y. Guo, and J. U. Kang, "Robust spectral-domain optical coherence tomography speckle model and its cross-correlation coefficient analysis," *Journal of the Optical Society of America A*, vol. 30, no.1, pp.51–59, 2013.

[120] N. Iftimia, B. E. Bouma, and G. J. Tearney, "Speckle reduction in optical coherence tomography by "path length encoded" angular compounding," *Journal of Biomedical Optics*, vol. 8, no. 2, pp. 260–263, 2003.

[121] M. Pircher, E. Götzinger, R. Leitgeb, A. F. Fercher, and C. K. Hitzenberger, "Speckle reduction in optical coherence tomography by frequency compounding," *Journal of Biomedical Optics*, vol. 8, no. 3, pp. 565–569, 2003.

[122] A. Ozcan, A. Bilenca, A. E. Desjardins, B. E. Bouma, and G. J. Tearney, "Speckle reduction in optical coherence tomography images using digital filtering," *Journal of the Optical Society of America A*, vol. 24, no. 7, pp. 1901–1910, 2007.

[123] J. Rogowska and M. E. Brezinski, "Evaluation of the adaptive speckle suppression filter for coronary optical coherence tomography imaging," *IEEE Transactions on Medical Imaging*, vol. 19, no. 12, pp. 1261–1266, 2000.

[124] R. C. Gonzalez and R. E. Woods, "Image processing," in *Digital Image Processing*, Upper Saddle River, NJ: Pearson, 2007.

[125] S. Sudha, G. Suresh, and R. Sukanesh, "Speckle noise reduction in ultrasound images by wavelet thresholding based on weighted variance," *International Journal of Computer Theory and Engineering*, vol. 1, no. 1, pp. 7–12, 2009.

[126] H. Guo, J. E. Odegard, M. Lang, R. A. Gopinath, I. W. Selesnick, and C. S. Burrus, "Wavelet based speckle reduction with application to SAR based ATD/R," in Image Processing, 1994. Proceedings. ICIP-94., IEEE International Conference, 1994, 75–79.

[127] S. G. Chang, B. Yu, and M. Vetterli, "Adaptive wavelet thresholding for image denoising and compression," *IEEE Transactions on Image Processing*, vol.9, no. 9, pp. 1532–1546, 2000.

[128] S. G. Chang, B. Yu, and M. Vetterli, "Spatially adaptive wavelet thresholding with context modeling for image denoising," *IEEE Transactions on Image Processing*, vol. 9, no. 9, pp. 1522–1531, 2000.

[129] X. Liu, Y. Huang, and J. U. Kang, "Distortion-free freehand-scanning OCT implemented with real-time scanning speed variance correction," *Optics Express*, vol. 20, no. 15, pp. 16567–16583, 2012.

[130] F. Sattar, L. Floreby, G. Salomonsson, and B. Lovstrom, "Image enhancement based on a nonlinear multiscale method," *IEEE Transactions of Image Processing*, vol. 6, no. 6, pp. 888–895, 1997.

[131] R. Leitgeb, C. K. Hitzenberger, and A. F. Fercher, "Performance of Fourier domain vs. time domain optical coherence tomography," *Optics Express*, vol. 11, no. 8, pp. 889–894, 2003.

[132] M. A. Choma, M. V. Sarunic, C. Yang, and J. A. Izatt, "Sensitivity advantage of swept source and Fourier domain optical coherence tomography," *Optics Express*, vol. 11, no. 18, pp. 2183–2189, 2003.

[133] H. M. Salinas and D. C. Fernández, "Comparison of PDE-based nonlinear diffusion approaches for image enhancement and denoising in optical coherence tomography," *IEEE Transactions on Medical Imaging*, vol. 26, no. 6, pp. 761–771, 2007.

[134] L. Fang, S. Li, Q. Nie, J. A. Izatt, C. A. Toth, and S. Farsiu, "Sparsity based denoising of spectral domain optical coherence tomography images," *Biomedical Optics Express*, vol. 3, no. 5, pp. 927–942, 2012.

[135] S. Chitchian, M. A. Fiddy, and N. M. Fried, "Denoising during optical coherence tomography of the prostate nerves via wavelet shrinkage using dual-tree complex wavelet transform," *Journal of Biomedical Optics*, vol. 14, no. 1, article no. 014031, 2009.

[136] S. Yazdanfar, A. M. Rollins, and J. A. Izatt, "Imaging and velocimetry of the human retinal circulation with color Doppler optical coherence tomography," *Optics Letters*, vol. 25, no. 19, pp. 1448–1450, 2000.

[137] Z. Chen, T. E. Milner, S. Srinivas, X. Wang, A. Malekafzali, M. J. C. Van Gemert, and J. Stuart Nelson, "Noninvasive imaging of in vivo blood flow velocity using optical Doppler tomography," *Optics Letters*, vol. 22, no. 14, pp. 1119–1121, 1997.

[138] L. An, J. Qin, and R. K. Wang, "Ultrahigh sensitive optical microangiography for in vivo imaging of microcirculations within human skin tissue beds," *Optics Express*, vol. 18, no. 8, pp. 8220–8228, 2010.

[139] V. J. Srinivasan, S. Sakadžić, I. Gorczynska, S. Ruvinskaya, W. Wu, J. G. Fujimoto, and D. A. Boas, "Quantitative cerebral blood flow with optical coherence tomography," *Optics Express*, vol. 18, no. 3, pp. 2477–2494, 2010.

[140] M. Sticker, C. K. Hitzenberger, R. Leitgeb, and A. F. Fercher, "Quantitative differential phase measurement and imaging in transparent and turbid media by optical coherence tomography," *Optics Letters*, vol. 26, no. 8, pp. 518–520, 2001.

[141] C. Joo, T. Akkin, B. Cense, B. H. Park, and J. F. de Boer, "Spectral-domain optical coherence phase microscopy for quantitative phase-contrast imaging," *Optics Letters*, vol. 30, no. 16, pp. 2131–2133, 2005.

[142] X. Li, J. Han, X. Liu, and J. U. Kang, "Signal-to-noise ratio analysis of all-fiber common-path optical coherence tomography," *Applied Optics*, vol. 47, no. 27, pp. 4833–4840, 2008.

[143] J.-S. Lee, "Digital image enhancement and noise filtering by use of local statistics," *IEEE Transactions on Pattern Analysis and Machine Intelligence*, vol. 2, no. 2, pp. 165–168, 1980.

[144] F. Jin, P. Fieguth, L. Winger, and E. Jernigan, "Adaptive Wiener filtering of noisy images and image sequences," in Proceedings of the International Conference on Image Processing, 2003, vol. 342, pp. III-349–III-352.

[145] J. C. Wood and K. M. Johnson, "Wavelet packet denoising of magnetic resonance images: importance of Rician noise at low SNR," *Magnetic Resonance in Medicine*, vol. 41, no. 3, pp. 631–635, 1999.

[146] M. Alexander, R. Baumgartner, A. Summers, C. Windischberger, M. Klarhoefer, E. Moser, and R. Somorjai, "A wavelet-based method for improving signal-to-noise ratio and contrast in MR images," *Magnetic Resonance in Medicine*, vol. 18, no. 2, pp. 169–180, 2000.

[147] J. Mead, "Mechanical properties of lungs," *Physiological Reviews*, vol. 41, no. 2, pp. 281-330, 1961.

[148] D. T. Reilly, and A. H. Burstein, "The mechanical properties of cortical bone," *The Journal of Bone and Joint Surgery America*, vol. 56, no. 5, pp. 1001-1022, 1974.

[149] P. B. Dobrin, “Mechanical properties of arterises,” *Physiological Reviews*, vol. 58, no. 2, pp. 397-460, 1978.

[150] S. Chatelin, A. Constantinesco, and R. Willinger, “Fifty years of brain tissue mechanical testing: from in vitro to in vivo investigations,” *Biorheology*, vol. 47, no. 5-6, pp. 255-76, 2010.

[151] A. Wax, and V. Backman, “Classical light scattering models,” in *Biomedical applications of light scattering*, NY, USA: McGraw- Hill, 2010, pp. 3 – 29.

[152] X. Liu, F. Zaki, and Y. Wang, “Quantitative optical coherence elastography for robust stiffness assessment,” *Applied Science*, vol. 8, no. 8, pp. 1255, 2018.

[153] E. A. Swanson, J. A. Izatt, M. R. Hee, D. Huang, C. P. Lin, J. S. Schuman, C. A. Puliafito, and J. G. Fujimoto, "In vivo retinal imaging by optical coherence tomography," *Optics Letters*, vol. 18, pp. 1864-1866, 1993.

[154] N. Nassif, B. Cense, B. H. Park, S. H. Yun, T. C. Chen, B. E. Bouma, G. J. Tearney, and J. F. de Boer, “In vivo human retinal imaging by ultrahigh-speed spectral domain optical coherence tomography,” *Optics Letters*, vol. 29, pp. 480-482, 2004.

[155] M. Wojtkowski, R. Leitgeb, A. Kowalczyk, T. Bajraszewski, and A. F. Fercher, “In vivo human retinal imaging by fourier domain optical coherence tomography,” *Journal of Biomedical Optics*, vol. 7, pp. 457–463, 2002.

[156] J. W. Goodman, *Speckle Phenomena in Optics*, Englewood, CO: Roberts and Company,2007.

[157] Y. T. Pan, R. Birngruber, J. Rosperich, and R. Engelhardt, “Low-coherence optical tomography in turbid tissue: theoretical analysis,” *Applied Optics*, vol. 34, pp. 6564–6574, 1995.